

**Fabrication of thin films and nano columnar structures of Fe-Ni
amorphous alloys and modification of its surface properties by
thermal annealing and swift heavy ion irradiation for tailoring the
magnetic properties**

Thesis submitted to the
COCHIN UNIVERSITY OF SCIENCE AND TECHNOLOGY

in partial fulfilment of the requirements

For the award of the degree of
DOCTOR OF PHILOSOPHY

SENOY THOMAS

**Department of Physics
Cochin University of Science and Technology
Kochi-682 022, Kerala, India**

December 2009

Fabrication of thin films and nano columnar structures of Fe-Ni amorphous alloys and modification of its surface properties by thermal annealing and swift heavy ion irradiation for tailoring the magnetic properties

Ph. D. Thesis

Author

Senoy Thomas
Peedikayil House
Madathumoozhy
Ranni-Perunad P.O
Pathanamthitta, 689711
Kerala, India
Email: senoythomas@gmail.com

Supervising Guide

Prof. M R Anantharaman
Department of Physics
Cochin University of Science and Technology
Kochi-682 022, India
Email: mra@cusat.ac.in

December 2009

Cover Page Illustration

Front page: 3-D AFM image of Fe-Ni Columnar films

Nullius in verba

(The Royal Society, London, 1663)



Certificate

*Certified that the thesis entitled “**Fabrication of thin films and nano columnar structures of Fe-Ni amorphous alloys and modification of its surface properties by thermal annealing and swift heavy ion irradiation for tailoring the magnetic properties**”, submitted by Mr. Senoy Thomas is an authentic record of research work carried out by him under my supervision at the Department of Physics in partial fulfilment of the requirements for the award of degree of Doctor of Philosophy of the Cochin University of Science and Technology and the work embodied in this thesis has not been included in any other thesis submitted previously for the award of any other degree.*

Kochi-682 022
07-12-2009

Dr. M. R. Anantharaman
Professor
Department of Physics
Cochin University of Science and
Technology
Kochi-682 022
Kerala, India

Declaration

*I hereby declare that the thesis entitled "**Fabrication of thin films and nano columnar structures of Fe-Ni amorphous alloys and modification of its surface properties by thermal annealing and swift heavy ion irradiation for tailoring the magnetic properties**" submitted for the award of degree of Doctor of Philosophy of the Cochin University of Science and Technology is based on the original work done by me under the guidance of Prof. M. R. Anantharaman, Professor, Department of Physics, Cochin University of Science and Technology, Kochi-682 022 and this work has not been included in any other thesis submitted previously for the award of any other degree.*

Kochi-682 022
07-12-2009

Senoy Thomas

Acknowledgment

My PhD years at the Department of Physics, Cochin University of science and Technology, Cochin and this thesis has had mentorship from numerous outstanding individuals both from within the university and outside of it. It is to these individuals, that my heartfelt gratitude and thanks go out to, for without their help, this thesis would not have seen possible.

First and foremost I would like to express my deep and sincere gratitude to Professor Dr. M. R Anantharaman, Head of the Department of Physics, Cochin University of Science and Technology, Cochin who has been my supervisor since the beginning of my research career in CUSAT, Cochin .The association with him, which started in the February 2004 as a M.Phil student, and later in August 2005 as a Ph.D student, has transformed me in scientific as well as personal terms.He provided me with many helpful suggestions, important advice and constant encouragement during the course of this work. His understanding, encouraging and personal guidance have provided a good basis for the present thesis. In addition, he was always accessible and willing to help his students with their research. As a result, research life became smooth and rewarding for me.

I am deeply grateful to Dr. Raju V Ramanujan, Associate Professor, School of Materials Science and Engineering, Nanyang Technological University, Singapore for his detailed and constructive comments, and for his important support throughout this work.

I owe my most sincere gratitude to Prof. A K George, Dr. Salim Al-Harhi and Dr. Imad Al-Omari, who gave me the opportunity to work with them in the Department of Physics at Sultan Qaboos University Muscat and gave me untiring help during my difficult moments.

I was delighted to interact with Dr. D. K. Avasthi of IUAC, New Delhi during ion beam irradiation experiments. His insight to Ion-Matter interactions is second to none. Besides, he sets an example of a world-class researcher for his rigor and passion on research

Special Gratitude goes to Dr. D Sakthikumar, Associate Professor, Bio Nano Electronics Research Centre, Toyo University Japan for electron microscopy measurements and useful discussions.

I am grateful to Dr. P A Joy of NCL Pune, Prof Nickolai Sobolev of University of Aveiro, Portugal and Dr.P Radhakrishnan of CUSAT for their help during the various stages of my work.

I am grateful to all teachers, former head of the departments and non teaching staff of the Physics department, CUSAT for their help during various stages of my work.

I would like to thank my friends and colleagues that I have met in this my home far away from home called CUSAT. All my lab buddies at the Magnetics laboratory made it a convivial place to work. In particular, I would like to thank Vijutha, Veena, vasudevan sir, Narayanan, Reena, Ramkumar, Geetha, Sagar, Jamal Sir, Hysen and Tom Chettan for their friendship and help in the past five years. All other folks, including Malini Chechi, Asha Chechi, Swapna, Mathew Sir, Sanoj, Vinaya, Soumya, Anjali, Rajeev, Shyam, Ratheesh, Prema Teacher, Ajimsha, Anoop, Saji, Jose, Solar, Sreekumar, JK, Kishore, Radhakrishnan, Wilson, Teny Chechi, Beena, Arun, Binu, Rajeev

Tommy, Sajeevettan, Saravanan Chettan and my room mate Arun-Chemistry had inspired me in research and life through our interactions during my days in CUSAT. Thanks.

I thank with love and gratitude all my friends in Physics, Chemistry, Hindi, Statistics, Biotechnology, Instrumentation, Photonics and Polymer science Department.

I remember the days in IUAC and I thank my friends Abhilash, Jay, Srinivas, Patel, Misra, Dinesh, Prasad and Kishore for their love and support.

I am also greatly indebted to many teachers in the past: Prof. V K Premnath (St. Thomas College Ranni) and Prof. K A Jacob (St. Thomas College Kozhencherry) for getting me interested in experimental physics and coming to CUSAT.

During the course of this work, at CUSAT (2005 – 2009), I was supported in part by Inter University Accelerator Centre-New Delhi under UFUP 35036. Junior Research Fellowship from UGC and senior research fellowship from CSIR during the period 2008-2009 is gratefully acknowledged. I was also privileged with AG Merit scholarship from Marthoma Syrian church of Malabar during the year 2007.

My deepest gratitude goes to my family for their unflagging love and support throughout my life; this dissertation is simply impossible without them. I am indebted to my father, for his care and love. As a typical father in an Indian family, he worked industriously to support the family and spare no effort to provide the best possible environment for me to grow up and attend school. He never complained in spite of all the hardships in his life. I cannot ask for more from my mother, as she is simply perfect. I have no suitable word that can fully describe her everlasting love to me. I remember her constant support when I encountered difficulties and I remember, most of all, her delicious dishes. My special gratitude is due to my sister and her family for their loving support

Last but not least, thanks be to God for my life through all tests in the past five years. You have made my life more bountiful. May your name be exalted, honoured, and glorified.

Cochin, India, December 2009

Senoy Thomas

Contents

	Preface	i
1	Introduction	
1.1	Amorphous magnetic alloys	2
1.2	Nanocrystalline magnetic alloys	3
1.3	Methods of amorphous alloy formation	4
1.3.1	Liquid quenching method	4
1.3.2	Derivatives of the liquid quenching method	5
1.3.3	Other methods	5
1.4	Amorphous thin films by vapour deposition	6
1.5	A review on amorphous and nanocrystalline thin films	7
1.6	Some challenges in thin film magnetism	11
1.7	Magnetic nanostructures based on ferromagnetic alloys	13
1.8	Motivation	16
1.9	Objectives	19
2	Theory of magnetism in metallic alloys	
2.1	Magnetic dipole moments and magnetization	21
2.2	Ferromagnetic ordering (Curie) temperatures	23
2.3	Magnetic anisotropies	28
2.3.1	Magnetocrystalline anisotropy	28
2.3.2	Shape anisotropy	31
2.4	Magnetic domains and domain wall mobility	32
2.5	Random anisotropy	34
2.6	Technical magnetization	38
2.7	Magnetostriction	42
2.7.1	Magnetostriction in single crystal	43
2.7.2	Magnetostriction in poly crystalline materials	45
2.7.3	Magnetostriction in amorphous alloys	45

3	Analytical techniques employed for characterization	
3.1	Swift heavy ion irradiation	47
3.2	Structural Characterisation Techniques	49
3.2.1	Glancing angle x-ray diffraction	49
3.2.2	Electron Microscopy	50
3.2.3	Atomic Force Microscopy	54
3.2.4	Magnetic Force Microscopy	59
3.2.5	Scanning Tunneling Microscopy	62
3.3	Composition	65
3.3.1	Energy dispersive x-ray spectroscopy	65
3.3.2	X-Ray Photoelectron Spectroscopy	68
3.4	Magnetic measurements	71
3.4.1	Vibrating sample magnetometer	71
3.4.2	Ferromagnetic Resonance	74
4	Fabrication and characterisation of amorphous and nanocrystalline Fe-Ni thin films	
4.1	Introduction	79
4.2	Experiment	83
4.2.1	Preparation	83
4.2.2	Characterization	84
4.3	Results and discussions	85
4.3.1	Composition analysis	85
4.3.2	Structural and micro structural characterization	87
4.3.3	Magnetic studies	93
4.4	Conclusion	96
5	Swift heavy ion induced surface modification for tailoring coercivity in Fe-Ni based amorphous thin films	
5.1	Introduction	97
5.2	Experiment	101

5.3	Results	102
5.3.1	Glancing angle XRD studies	102
5.3.2	Atomic force microscopy studies	103
5.3.3	Vibrating sample magnetometer studies	105
5.4	Discussions	106
5.5	Conclusions	112
6	Thermal annealing induced surface smoothening and reorientation of surface magnetization in Fe-Ni thin films	
6.1	Introduction	113
6.2	Experiment	116
6.2.1	Preparation	116
6.2.2	Characterization	117
6.3	Results and discussions	117
6.4	Conclusions	131
7	Fabrication and surface evolution of amorphous nano columns of Fe-Ni grown by oblique angle deposition	
7.1	Introduction	133
7.2	Experiment	137
7.3	Results and discussions	139
7.4	Conclusion	149
8	Influence of substrate topography on the growth and magnetic properties of obliquely deposited amorphous nano columns of Fe-Ni	
8.1	Introduction	151
8.2	Experiment	153
8.2.1	Preparation	153
8.2.2	Characterization	154
8.3	Results and discussions	154
8.3.1	Evolution of morphology with substrate roughness	154

8.3.2	Magnetic properties	158
8.4	Conclusions	164
9	Characterisation of Fe-Ni amorphous thin films for possible magnetostrictive sensor applications	
9.1	Introduction	165
9.2	Experiment	168
9.3	Results and discussions	169
9.4	Conclusions	174
10	Conclusions and future outlook	175
	Symbols used in the thesis	183
	Abbreviations used in the thesis	187
	Bibliography	189

Preface

Magnetic materials have been playing an important role in the day today life of human beings from the time lodestone was discovered. They form part of many devices and the field of magnetism today provides the world's second largest industry, with magnetic materials claiming a market share next to semiconductor industry. In the current scenario the demand for magnetic material is fast rising and magnetism has taken a central stage in science and technology. Even more excitingly, several exotic magnetic phenomenon and novel materials have recently been discovered, many of which seem to hold the vital keys in unlocking fascinating as well as challenging physics. The recent discovery of giant magneto resistance and the emergence of spintronics are all a testimony to this fact.

The properties of magnetic materials range widely, from hard magnetic to soft magnetic and insulating to metallic. Materials with excellent soft magnetic properties are extensively used in power transformers, sensors and magnetic shielding devices. Most of the applications in the past were based on crystalline magnetic materials. However, the newest addition to the class of soft magnetic materials is not crystalline, but amorphous and nanocrystalline. Amorphous magnets were first fabricated in 1967 from their liquid states by means of a rapid-quenching technique. The tremendous advances made in this field during a short span of time have led to the further discovery of new magnetic materials and new phenomenon which in turn resulted in newer applications of the materials. The subject is now a hot topic of research in solid state physics and is of interest to physicists, materials scientists and electrical and electronics engineers. In fact, amorphous magnets exhibit a wide range of new phenomena, in contrast to those of their crystalline counterparts where the periodicity of constituent atoms by and large determine the overall magnetic properties. Atoms in

an amorphous magnet are distributed randomly, resulting in a disordered state and physicists are rather perplexed in explaining the magnetic order resulting out of complete absence of a specific crystal structure.

Nanocrystalline magnetic materials have been known for over twenty years since the discovery of Finemet by Yoshisawa and coworkers in 1988. However, it is only the recent developments in complex alloys and their metastable amorphous precursors which revolutionized the field of soft magnetism. Nanoscience and Nanotechnology is leading this revolution fueled by the industrial progress, the scientific ability to fabricate, model and manipulate nano magnetic materials, and the almost daily discovery of new phenomena in nanoscale magnetic materials. Nanocrystalline magnetic materials are commonly produced by the partial crystallization of its amorphous precursors. The microstructure of these materials consists of nano sized ferromagnetic materials embedded in an amorphous matrix. The matrix phase must also be ferromagnetic for facilitating the exchange coupling between the nanoparticles. As a result of this coupling, they often exhibit vanishing magnetocrystalline anisotropy. Since the soft magnetic properties are strongly related to the crystalline anisotropy, the exchange interaction in nanocrystalline magnetic materials often results in an improvement of their soft magnetic properties. Interesting properties of nanocrystalline magnetic materials are a consequence of the effects induced by the nanocrystalline structure. They include interface physics, the influence of the grain boundaries, the averaging of magnetic anisotropy by exchange interactions, the decrease in exchange length, and the existence of a minimum two-phase structure in such materials.

There has been extensive research in amorphous and nanocrystalline materials in melt-spun ribbon form, which exhibit excellent magnetic properties: large saturation magnetostriction, high saturation magnetization, low anisotropy energies and low coercivity. These factors have made soft magnetic ribbon materials excellent

candidates for sensors and actuator devices. Despite their excellent magnetic properties, the as-cast melt-spun ribbons suffer from high randomly orientated stresses, which give rise to a complicated domain structure. However, it is well established that in the stress relieved or magnetically annealed state, they exhibit excellent soft magnetic properties. The disadvantages of these ribbon materials are; it is difficult to incorporate into sub-millimeter dimensional devices and, most importantly of all, there is no suitable means of bonding such materials onto micro-fabricated structures. The ribbon materials are currently bonded to larger devices using epoxy resin. Also, it is found that the optimized domain structure obtained by magnetic annealing is disturbed on curing the epoxy resin, which induces stress into the ribbon.

Since metallic glasses are widely used for sensor applications, thin film form of this material would be of great interest for integrating thin film sensors with today's microelectronics. This can be realized by depositing thin films of this material on suitable substrates. This not only allows miniaturization of the sensor elements, as dictated by technological demands for smaller and smaller electrical components, but also enables the same micro-fabrication technologies to be used in both the production of the electronic and the magnetic devices especially for applications like MEMS, NEMS etc. This makes it commercially more attractive due to the reduced costs and the applicability to a wider range of systems.

Further, arrays of magnetic nanostructures can find immense applications in high density recording media and magnetic random access memory. They are also model candidates for studying fundamental physical properties of small magnetic particles. A very important issue in connection with these studies is to assemble these magnetic nanostructures in an effective and controllable way. Several strategies have been developed for the growth of nanostructured magnetic materials. Nanolithography-based methods, solution-based approaches and template-based

methods are some of them. Some of these methods, however, require high temperatures and special conditions while in other cases, they demand complex and tedious procedures. For instance, in template assisted growth of nanostructures, the selection of suitable catalysts and templates are not straightforward, and the removal of templates and the stabilization of unsupported nanostructures are crucial issues that may compromise the structural and physical properties. The capability of obtaining ordered arrays of well-defined and periodic nanostructures in an accurate, fast, and inexpensive fashion would be of great interest not only from an applied perspective but also from a fundamental point of view. Oblique angle vapor deposition offers advantages associated with fabrication of nanostructures over large areas, as required in many advanced technological and industrial applications. Here, vapour atoms arrive on the substrate at oblique angles relative to the surface normal of the substrate. The evaporant nucleates on the substrate; the region behind the nucleus does not receive any further vapor because of the shadowing by the nucleus. Therefore, vapor will be deposited only onto the nucleus. This preferential growth dynamics give rise to the formation of isolated columnar structures. Some advantages of this technique are the non requirement of templates, relatively low temperatures and less harmful chemicals for the nanostructure fabrication. For the synthesis of well defined nanostructures having appropriate separation and clear surface morphologies, an understanding on the interplay between the mechanisms involved in the growth process is essential. From an applied stand point, a detailed knowledge of the growth behavior of the nanostructures on a solid surface will aid in synthesizing nanostructures with well defined roughness and geometry.

It is likely that thin film and periodic nanostructures of soft magnetic materials will soon become an important part of the bigger family of magnetic materials. The emergence of these new materials also represents a significant challenge to the scientific understanding of magnetic materials, since many properties of these

materials could not be understood in the framework of the existing theories which mostly presume bulk (three dimensional) geometries. For these technological and scientific reasons, the amorphous and nanocrystalline magnetic alloys in thin film form have been very actively studied over the last few years by many researchers. These intense activities have resulted in a vast number of publications. A survey of the literature reveals the existence of plenty of reports on the various techniques available for fabrication soft magnetic thin films. But there is a lack of an understanding on the relationship of the film microstructure and film magnetic properties. The significant advancements in the development of instrumentation and techniques for characterizing magnetic materials now enable one for such a study. In particular, the combined use of atomic force microscopy and magnetic force microscopy can establish a clear correlation between the surface structure of a material and its magnetic properties. Such a study is important in the thin film scenario where one is manipulating magnetism via the surface or interface roughness or by fabricating artificial structures which do not appear in nature.

This thesis lays importance in the preparation of thin films of Fe-Ni amorphous alloys by a simple thermal evaporation technique. The focus is on Fe-Ni due to their excellent soft magnetic properties. Their saturation magnetization and magnetostriction is high compared to Co-based amorphous alloys. Also they are interesting candidates for magnetic shielding devices due to their higher permeability. The microstructure as well as surface morphology of the Fe-Ni films is modified using ion beam irradiation and thermal annealing. The evolution of the surface with various parameters like ion fluence, vapour deposition time, annealing temperature and substrate surface roughness was studied using atomic force microscopy. It was found that the film's surface roughness and microstructure has a significant influence on the magnetic properties such as coercivity, remanence, saturating field, demagnetizing field and spin reorientation transition. Attempts are made to correlate the observed

magnetic properties with film surface/microstructure. The objectives of the present investigation can be summarized as follows

- ❖ Prepare thin films of Fe-Ni amorphous alloys.
- ❖ Modify the surface morphology and micro structure of these films by thermal annealing and ion beam irradiation.
- ❖ Study the effect of nanocrystallization and surface modification on the magnetic properties.
- ❖ Prepare columnar thin films of Fe-Ni amorphous alloys by oblique angle vapour deposition.
- ❖ Study the evolution of the column with the deposition time and substrate surface roughness.
- ❖ Characterizing the amorphous Fe-Ni films for possible magnetostrictive sensor applications.

This proposed thesis is entitled *“Fabrication of thin films and nano columnar structures of Fe - Ni amorphous alloys and modification of its surface properties by thermal annealing and swift heavy ion irradiation for tailoring the magnetic properties”* and consist of nine chapters.

Chapter 1 provides an overview on amorphous and nanocrystalline magnetic materials. A review on the preparation and characteristics of various amorphous and nanocrystalline thin films is also presented. The motivation for this particular study is clearly spelt out with a listing of the objectives.

Amorphous magnetism is rarely dealt in length in text books and so a thorough literature survey is carried out on amorphous magnetism and a gist of the theory of magnetism of amorphous alloys is provided in **Chapter 2**.

Chapter 3 describes the working principle of various analytical techniques used for characterizing the amorphous and nanocrystalline Fe-Ni thin films. The films

were structurally characterized using glancing angle x-ray diffraction (GAXRD), transmission electron microscopy (TEM) and scanning electron microscopy (SEM). The surface morphology of the films was probed using atomic force microscopy (AFM) and scanning tunneling microscopy (STM). The imaging of the magnetic domains was carried out using magnetic force microscopy (MFM). Compositions of the films were determined using energy dispersive x-ray spectroscopy (EDS) and x-ray photoelectron spectroscopy (XPS). The magnetic properties of the samples were characterized employing vibrating sample magnetometer (VSM) and ferromagnetic resonance (FMR) techniques.

Chapter 4 deals with the preparation and characterization of amorphous and nanocrystalline thin film of Fe-Ni. Nanocrystalline Fe-Ni thin films were prepared by the partial crystallization of vapour deposited amorphous precursors. The microstructure was controlled by annealing the films at different temperatures. X-ray diffraction, transmission electron microscopy and energy dispersive x-ray spectroscopy investigations showed that the nanocrystalline phase was that of Fe-Ni. Grain growth was observed with an increase in annealing temperature. X-ray photoelectron spectroscopy observations showed the presence of native oxide layer on the surface of the films. Magnetic studies using vibrating sample magnetometer shows that coercivity has a strong dependence on grain size. This is attributed to the random magnetic anisotropy characteristics of the system. The observed coercivity dependence on grain size is explained using modified random anisotropy model.

Surface modification of amorphous Fe-Ni thin films by swift heavy ion irradiation and there by controlling the coercivity forms the main theme of **Chapter 5**. Fe-Ni based amorphous thin films were irradiated by 108 MeV Ag⁸⁺ ions at room temperature with fluences ranging from 1×10^{12} to 3×10^{13} ions/cm² using a 15 UD Pelletron accelerator at Inter University Accelerator Centre, New Delhi. Glancing angle x ray diffraction (GAXRD) studies showed that the irradiated films retain their

amorphous nature. The topographical evolution of the films under swift heavy ion bombardment was probed using atomic force microscope (AFM) and it was noticed that surface roughening was taking place with ion beam irradiation. Magnetic measurements using a vibrating sample magnetometer (VSM) showed that the coercivity of the films increase with an increase in the ion fluence. The observed coercivity changes are correlated with topographical evolution of the films under swift heavy ion irradiation.

Investigations on the effect of thermal annealing on the surface roughness of the Fe-Ni thin films are presented in **Chapter 6**. It was found that a surface smoothing of the film occurs at higher annealing temperature. Ferromagnetic resonance measurements revealed that the demagnetizing field along the in-plane direction was decreasing with annealing temperature while that along the out-of plane direction increased. This resulted in a transition of surface magnetization direction from out-of-plane to in-plane. The observed modifications of the magnetic properties are correlated with the annealing induced surface modification in Fe-Ni thin films.

Chapter 7 presents the growth and surface evolution amorphous nano columns of Fe-Ni prepared by oblique angle deposition. Atomic force microscopy (AFM) was used for studying the evolution of the surface of these columnar thin films with deposition time. It has been found that the root mean square (rms) roughness increased with the deposition time but showed a less significant change at higher deposition time. The separation between the nanostructures increased sharply during the initial stages of growth and the change was less significant at higher deposition time. These results suggests that during initial stages of growth, self shadowing is dominating and as the deposition time increases surface diffusion is also playing an active role in the growth process.

Chapter 8 describes the influence of substrate surface roughness on the structural and magnetic properties of obliquely deposited amorphous nano columns of

Fe-Ni. Experiments showed that the surface roughness of the substrate greatly determines the morphology of the columnar structures and this in turn has a profound influence on the magnetic properties. Nucleation of Fe-Ni nano columns on a smooth silicon substrate were at random, while that on a rough glass substrate was defined by the irregularities on the substrate surface. It has been found that magnetic interaction between the nano columns prepared on silicon substrate was due to their small inter column separation. Well separated nano columns on glass substrate resulted in exchange isolated magnetic domains. The size, shape and the distribution of nano columns can be tailored by appropriately choosing the surface roughness of the substrate which will find potential applications in thin film magnetism.

In **Chapter 9**, a technique for measuring the magnetostriction in amorphous Fe-Ni thin film is described. An optical fiber long period grating (LPG) was used for this purpose. An LPG consists of a periodic modification of the refractive index of the core of an optical fiber. For these gratings, the energy typically couples from the fundamental guided mode to discrete, forward propagating cladding mode. When a tensile stress is applied to the optical fiber long period grating the periodic spacing changes and reversibly causes the coupling wavelength to shift. This provides a sensitive mechanism to measure the stress/strain and also the magnetostriction of a material attached to the fiber grating. Fe-Ni thin films were coated on a long period grating. The magnetostriction of the films was determined from the change in the peak position of the attenuation band when a magnetic field was applied along the axis of the fiber. Results indicate that LPG in combination with Fe-Ni thin films can act as a potential candidate in the field of magnetostrictive sensors.

Chapter 10 is the concluding chapter of the thesis and in this chapter the salient observations and the inferences drawn out of these investigations are presented in a nutshell. The scope of further work is also proposed here.

Part of the work has resulted in the following publications

Peer reviewed journals

1. **Senoy Thomas**, S. H. Al-Harhi, R. V. Ramanujan, Zhao Bangchuan, Liu Yan, Wang Lan, and M. R. Anantharaman “Surface evolution of amorphous nanocolumns of Fe–Ni grown by oblique angle deposition”. (Appl. Phys. Lett. 94, 063110, 2009).
2. **Senoy Thomas**, Hysen Thomas, D. K. Avasthi, A. Tripathi, R. V. Ramanujan, and M. R. Anantharaman “Swift heavy ion induced surface modification for tailoring coercivity in Fe–Ni based amorphous thin films” (J. Appl. Phys. 105, 033910, 2009)
3. **Senoy Thomas**, S H Al-Harhi, D Sakthikumar, I A Al-Omari, R V Ramanujan, Yasuhiko Yoshida and M R Anantharaman “Microstructure and random magnetic anisotropy in Fe–Ni based nanocrystalline thin films” (J. Phys. D: Appl. Phys. 41, 155009, 2008).
4. **Senoy Thomas**, S. H. Al-Harhi, I. A. Al-Omari, R. V. Ramanujan and M.R. Anantharaman “Influence of substrate topology on the growth and magnetic properties of obliquely deposited amorphous nano columns of Fe-Ni”. (J. Phys. D: Appl. Phys. 42, 215005, 2009)
5. **Senoy Thomas**, D Sakthikumar, Yasuhiko Yoshida and M R Anantharaman “Spectroscopic and photoluminescence studies on optically transparent magnetic nanocomposites based on sol-gel glass: Fe₃O₄”. (Journal of Nanoparticle research 10, 203, 2008).
6. **Senoy Thomas**, Saritha K Nair, E Muhammad Abdul Jamal, S H Al-Harhi, Manoj Raama Varma and M R Anantharaman “Size-dependent surface

- plasmon resonance in silver silica nanocomposites” (Nanotechnology 19, 075710, 2008)
7. T N Narayanan, Soumya Jose, **Senoy Thomas**, S H Al-Harhi and M R Anantharaman “Fabrication of a quantum well heterostructure based on plasma polymerised aniline and its characterization using STM/STS”. (J. Phys. D: Appl. Phys. 42, 165309, 2009)
 8. Hysen Thomas, **Senoy Thomas**, R. V. Ramanujan and M. R. Anantharaman “On the crystallization kinetics and micro-structural transformations of $\text{Fe}_{40}\text{Ni}_{38}\text{B}_{18}\text{Mo}_4$ ” alloys. (Journal of Materials Science 43, 635, 2008)
 9. H M Widatallah, C Johnson, A M Gismelseed, I A Al-Omari, S J Stewart, S H Al-Harhi, **S Thomas** and H Sitepu “Structural and magnetic studies of nanocrystalline Mg-doped $\text{Li}_{0.5}\text{Fe}_{2.5}\text{O}_4$ particles prepared by mechanical milling” (J. Phys. D: Appl. Phys. 41, 165006, 2008).
 10. **Senoy Thomas**, D Sakthikumar, P A Joy, Yasuhiko Yoshida and M R Anantharaman “Optically transparent magnetic nanocomposites based on encapsulated Fe_3O_4 nanoparticles in a sol-gel silica network”. (Nanotechnology 17, 5565, 2006)
 11. **Senoy Thomas**, Swapna S Nair, Joana S Martins, Nikolai A. Sobolev, S H Al-Harhi, R V Ramanujan and M R Anantharaman "Thermally induced reorientation of surface magnetization in Fe-Ni thin films –A study using magnetic force microscopy and ferromagnetic resonance" (Under Revision)
 12. **Senoy Thomas**, Jinesh Mathew, P Radhakrishnan, V P N Nampoori, A K George, R V Ramanujan and M R Anantharaman "Fe-Ni based amorphous thin films as a magnetostrictive sensor material" (Under Revision)

Conference Presentations

1. **Senoy Thomas**; Salim Al-Harhi ; Imad Al-Omari; Raju. V. Ramanujan; M. R. Anantharaman “Growth and Magnetic Properties of Fe-Ni based Amorphous Nanocolumns Obtained by Oblique Angle Vapour Deposition”. International Conference on Materials for Advanced Technologies (ICMAT-2009) Singapore, 28 June-3 July, 2009.
2. **Senoy Thomas**, Hysen Thomas, D. K. Avasthi, A. Tripathi, R. V. Ramanujan, and M. R. Anantharaman. “Ion beam assisted surface modification in Fe-Ni amorphous thin films”. Indo-French Conference on Nanostructuring by Ion Beams, Bhubaneswar (Feb.26-Mar.1, 2009)
3. **Senoy Thomas**, S. H. Al-Harhi, I A Al-Omari, A. K. George, R. V. Ramanujan, and M. R. Anantharaman. “On the growth and evolution of amorphous nano columns of Fe-Ni by oblique angle vapour deposition”. Second International Conference on Frontiers in Nanoscience and Technology (Cochin Nano-2009). Jan 3-6, 2009, Cochin, India
4. **Senoy Thomas**, Ansar K., Saritha K. Nair and M. R. Anantharaman. “Surface plasmon resonance of silver nano particles in sol-gel silica”. National conference on nano photonic materials (NCNM 2008) Cochin University of Science and Technology, Kochi Oct 10-12 2008.
5. **Senoy Thomas**, D. K Avasthi and M. R. Anantharaman. “Ion-beam induced surface modification and coercivity changes in Fe-Ni based amorphous thin films”. International conference on magnetic materials and their applications for 21st century (MMA-21). Delhi Oct 21-23 2008.
6. **Senoy Thomas**, D Sakthikumar, Yasuhiko Yoshida and M R Anantharaman. “TEM studies on Fe₃O₄ nanoparticles in silica glass obtained

- by sol-gel method”. National Conference on Smart Electro ceramics (NCSE-2007), Kerala, India.
7. Geetha P, **Senoy Thomas**, D Sakthikumar, Yasuhiko Yoshida and M R Anantharaman “Transparent magnetic nanocomposites based on Iron oxide and SiO₂”. National Conference on “New horizons in theoretical and experimental physics”, NHTEP 2007, Cochin University of Science and Technology, Kochi, Oct 8-10, 2007.
 8. **Senoy Thomas** and M R Anantharaman. “Synthesis and characterization of a transparent magnetic composite”. Opto electronic Materials for Advanced Technology (OMTAT), International Conference, Cochin, India, Oct, 24-27, 2005.

Introduction

Contents

- 1.1 Amorphous magnetic alloys
- 1.2 Nanocrystalline magnetic alloys
- 1.3 Methods of amorphous alloy formation
- 1.4 Amorphous thin films by vapour deposition
- 1.5 A review on amorphous and nanocrystalline thin films
- 1.6 Some challenges in thin film magnetism
- 1.7 Magnetic nanostructures based on ferromagnetic alloys
- 1.8 Motivation
- 1.9 Objectives

Amorphous and nanocrystalline materials have been investigated over the past years, for soft magnetic applications such as in transformers and inductive devices. The crucial parameters that decide their applicability in such devices are high induction, high permeability and high Curie temperature. Apart from these requirements these materials must also possess good mechanical properties and corrosion resistance. In achieving such goals the key issues include alloy chemistry, structure and most importantly among others the ability to tailor the microstructure. Therefore materials selected for soft magnetic applications must be optimized in terms of their intrinsic and extrinsic magnetic properties as well as their morphology. Intrinsic magnetic properties such as saturation magnetic induction, B_s , and Curie temperatures, T_C , are determined by alloy composition and crystal structure. Permeability, μ which is an extrinsic property is usually determined by chemistry, crystal structure, microstructure and morphology (shape). In particular, alloys with small magnetocrystalline anisotropies and magnetostrictive coefficients give rise to excellent soft magnetic properties.

Alloys for soft magnetic applications may be single phase (Type I-Amorphous) or bi phasic materials (Type II-Nanocrystalline) with a nanocrystalline ferromagnetic phase and a residual amorphous phase at the grain boundaries. The Type II nanocrystalline alloys possess (1) high resistivity (50-80 $\mu\Omega\text{cm}$) (2) low magneto crystalline anisotropy and (3) increased mechanical strength. With properties such as these, nanocrystalline alloys have great potential as soft magnetic materials. The most common compositions for soft magnetic applications either in the amorphous or in the nanocrystalline state are metal-metalloid based (Fe, Co, Ni)-(Si, B) alloys with small additions of Mn, Nb, C and, for the nanocrystalline case, of Cu. This alloy system has a good glass forming ability and is easily accessible by rapid solidification as a thin ribbon in large scale production.

1.1 Amorphous magnetic alloys

The fundamental properties of magnetic amorphous alloys are the saturation magnetization M_s , the magnetostriction constant λ_s , the Curie temperature T_c and their crystallization temperature, T_x . The saturation magnetization M_s is highest in Fe-rich alloys and decreases with increasing Ni and Co content. It is generally lower than in crystalline alloys due to the non-magnetic additions of metalloids (Si and B) necessary for glass formation. Another magnetic parameter determined mainly by the transition metals is the magnetostriction which is isotropic in the amorphous state. For Fe-rich alloys the saturation magnetostriction λ_s is positive, typically $\lambda_s \approx 20 - 40$ ppm, while for Co-rich alloys, λ_s is negative, typically $\lambda_s \approx -5$ to -3 ppm. Thus, according to their magnetostriction values, amorphous soft magnetic materials are commonly divided into two major groups: Fe-based and Co-based alloys. Fe-based amorphous alloys are based on inexpensive raw materials and have a high saturation magnetization but their magnetostriction is large which limits their soft magnetic behaviour. On the other hand, Co-based amorphous alloys with small additions of Fe or Mn reveal nearly zero

magnetostriction. Accordingly, they can offer superior soft magnetic behaviour, but their saturation magnetization is considerably lower than that for Fe-based materials.

1.2 Nanocrystalline magnetic alloys

Nanocrystalline alloys can be synthesized by a variety of techniques such as rapid solidification from the liquid state, mechanical alloying, plasma processing or vapor deposition [1]. The requirements on the microstructure necessary for the soft magnetic properties rule out quite a number of the available processes. Thus, controlled crystallization from the amorphous state seems to be a viable method to synthesize nanocrystalline alloys with attractive soft magnetic properties. A typical nanocrystalline structure with appropriate soft magnetic properties can be obtained if the amorphous state is crystallized by the primary crystallization of bcc Fe, before intermetallic phases are formed. An example is $\text{Fe}_{73.5}\text{Cu}_1\text{Nb}_3\text{Si}_{13.5}\text{B}_9$ (at %) which was proposed by Yoshizawa in 1988. Nanocrystalline Fe-Si-B-Nb-Cu alloys have been patented under the trade name Finemet[®] [2, 3]. The combined addition of Cu and Nb is responsible for the formation of the nanocrystalline microstructure wherein copper enhances the nucleation of the bcc grains while niobium impedes grain coarsening and, at the same time, inhibits the formation of boride compounds. The nanocrystalline state is achieved by annealing the amorphous precursors at temperatures typically between 500°C and 600°C which results in primary crystallization of bcc Fe. The resulting microstructure is characterized by randomly oriented, ultrafine grains of bcc Fe- Si-20 at% with typical grain sizes of 10–12 nm embedded in a residual amorphous matrix which occupies about 20-30% of the volume with crystallites separation at about 1–2 nm [2]. These features are the basis for the excellent soft magnetic properties indicated by high values of initial permeability of about 10^5 and correspondingly low coercivities of less than 1 A/m. Both an extremely high nucleation rate and slow growth of the crystalline precipitates

are needed for obtaining such a nano scaled microstructure in an amorphous matrix. Such crystallization characteristics can be only obtained with appropriate alloy design.

The superior soft magnetic properties found in the original compositions of $\text{Fe}_{74}\text{Cu}_1\text{Nb}_3\text{Si}_{13-16}\text{B}_{6-9}$ are comparable to the excellent properties known so far from permalloys or Co-base amorphous alloys. The advantages, however, are the higher saturation induction of 1.2-1.3 T (twice the value of near zero magnetostrictive Co based amorphous alloys) and better thermal stability of the soft magnetic properties.

The search for alloy compositions exhibiting higher saturation magnetization resulted in a second family of near-zero magnetostrictive, nanocrystalline alloy based on $\text{Fe}_{84-91}(\text{Cu}_1)-(\text{Zr}, \text{Nb})_7\text{B}_{2-9}$. The major hindrance towards realizing such a high iron content alloys resulted from the requirement of a good glass forming ability. The glass forming range is the widest for Hf containing alloys and decreases in the order of $\text{Zr} > \text{Nb} \approx \text{Ta} > \text{Mo} \approx \text{W} > \text{V} > \text{Cr}$. The most stable amorphous phase is obtained in alloys containing refractory metals with large atoms and low d -electron concentrations, that is particularly Zr, Hf, Nb and Ta. The $\text{Fe}_{84-91}(\text{Cu}_1)-(\text{Zr}, \text{Nb})_7\text{B}_{2-9}$ based nanocrystalline alloys exhibits a higher saturation magnetization up to 1.7 Tesla. Their major drawback is a lower glass forming ability and castability due to the oxygen reactivity of the Zr. The preparation of Fe-Zr-B thin ribbons by rapid solidification, thus, requires substantially more effort than necessary for the more conventional Fe-(Cu,Nb)-Si-B compositions and, therefore, presently is restricted to the laboratory scale.

1.3. Methods of amorphous alloy formation

1.3.1. Liquid quenching method. The most widely used method for producing amorphous alloys is the chill-block liquid quenching method. The principle used is the direct rapid solidification of the melt through its contact with a metal block which quickly extracts heat from it. In implementing this, many variations of apparatus have been designed and built. These techniques have been reviewed by Chen *et al* [4]. The most popular technique is the melt-spinning technique. A jet of molten liquid is

squirted out of a nozzle onto a rotating disc which cools the liquid by contact and produces a long ribbon of uniform geometry. The history of the rapid solidification system goes back to the patent of Strange and Pim [5] who used it to produce metal pellets.

Amorphous alloys were first produced by the continuous solidification technique by Chen and Miller [6] and Babic *et al.* [7], who used dual rollers, and by Masumoto and Maddin [8] who used the technique of Pond and Maddin [9]. The technique of melt-spinning was described by Liebermann and Graham [10]. Since the essence of the method is the rapid extraction of heat by physical contact, the maximum thickness of the amorphous ribbon which can be produced by this method is inversely proportional to the critical cooling rate, if the thermal conductivity of the chilling block is much higher than that of the melt. The maximum thickness of the transition melt based alloy is usually in the range 10-100 μm . Sheets several inches wide are commercially available.

1.3.2. Derivatives of the liquid quenching method. The liquid quenching methods with or without a chill-block is used to produce wires and particles. By cooling the melt jet with flowing water, wires with a circular cross section can be produced. Amorphous or crystalline particles can be produced by spraying molten liquid droplets into an inert gas or cooling liquid. Small particles up to 50 μm in diameter can also be produced by a spark erosion method [11, 12]. Spraying of molten liquid droplets onto the metal surface can be used to coat the surface with an amorphous sheet. Surface coating is also possible using laser glazing which only melts the surface of the metal [13].

1.3.3. Other methods. Surface modification methods such as ion implantation and ion irradiation can also result in an amorphous structure. A change of composition due to ion implantation and the physical structural damage due to the impact of ions can result in the amorphous phase. It is known that easy glass formers can be vitrified

at a lower ion dosage. Amorphous films can be obtained by ion mixing of multilayered samples [14]. By irradiating thin multilayered crystalline films, it is possible to mix them to form amorphous films. Amorphous alloys can also be formed by chemical deposition or electro-deposition [15, 16]. Schwartz and Johnston [17] reported that amorphous La-Au alloys were formed by solid-state reaction starting from the crystalline state. Thin multiple layers of crystalline La and Au, each a few hundred angstroms thick, were alternately deposited by sputtering and were annealed at temperatures high enough to promote interdiffusion, but not too high to cause the formation of the intermetallic compound. Because of the strongly negative heat of mixing the sample was compositionally homogenised by annealing and the bulk of it became non-crystalline. Although the method may be applicable to only a limited number of alloy systems, and furthermore it is not yet clear how good an amorphous state can be achieved by this method, it represents a totally new avenue of glass formation and demonstrates the fact that the glassy state can be more stable than the mixture of pure elements or a solid solution.

It is to be noted that the soft magnetic materials obtained via the above mentioned techniques are in the form of ribbons, wires or powders. Hence alternative techniques have to be developed for preparing amorphous and nanocrystalline materials in the thin film form. This is essential for miniaturising the magnetic devices and integrating these elements into MEMS and NEMS. Thin films based on soft magnetic materials can be prepared by techniques such as thermal evaporation, electro deposition, molecular beam epitaxy, pulsed laser deposition and sputtering. Vapour deposition offers a simple alternative to other techniques in obtaining thin films of supersaturated solid solutions and other metastable states.

1.4. Amorphous thin films by vapour deposition

Rapid quenching can be achieved at an atomic level by vapour deposition. It is sometimes suggested that very high quenching rates can be achieved by these

methods, so that glasses can be formed over wider compositional ranges. Although the exact atomistic process of deposition is unknown at this moment, each atom must be deposited from vapour to the solid in a very short time, after possibly migrating on the surface momentarily. Therefore the primary cooling rate is indeed quite high. The effective quenching rate may not be so high compared to the liquid quenching, and the composition range of glass formation is largely determined by the same principle as in the case of liquid quenching [18] although a larger number of exceptions are found. An important difference is that, since this method bypasses the liquid phase, even the alloy systems which show a strongly positive heat of mixing and tend to phase-separate in the liquid state can be made amorphous. For instance, Fe and Ag are immiscible in the liquid state. Therefore Fe- Ag alloys cannot be made by liquid quenching, but apparently amorphous Fe-Ag alloys can be obtained by thin film deposition [19]. Fe-B is another example of a binary alloy which can be prepared by vapour deposition [20]. Next section will give a brief introduction to the work done so far in the field of amorphous and nanocrystalline thin films.

1.5. A review on amorphous and nanocrystalline thin films

With the advent of amorphous and nanocrystalline ferromagnetic alloys showing excellent soft magnetic properties the thin film form of this would find applications in miniaturizing magnetic devices. It is to be noted that the spectrum of accessible amorphous and nanocrystalline systems can be considerably expanded by thin film deposition techniques. One example is Hf carbide dispersed nanocrystalline Fe-Hf-C films crystallized from the amorphous state. They combine good thermal stability, good high frequency properties in the MHz range with low magnetostriction and high saturation induction of $M_s=1.7$ T which can be even increased up to 2 T by multilayering these films with Fe [21].

Another example is (Fe,Co,Ni)-(Si,B)-(F,O,N) granular alloy films which at a saturation induction of about 1 T possess a uniquely high electrical resistivity of 10^3 -

$10^4 \mu\Omega\text{cm}$ which makes them a possible candidate for high frequency devices [21]. Neagu [22] studied the optical and magneto optical properties of amorphous Fe-Cu-Nb-Si-B thin films prepared by pulsed laser ablation. The films prepared were 100-200 nm thick and were deposited on Si and glass substrates. As the thickness of the film increased the surface coercivity increased. For the same thickness, the films coated on Si substrate showed a lesser coercivity than that on glass.

Kurlyandskaya *et al.* [23] used dc focused pulsed laser ablation for the preparation of amorphous thin films of $\text{Fe}_{67}\text{Co}_{18}\text{Si}_1\text{B}_{14}$. The target used was Metglas 2605. They were able to deposit films with a coercivity in the range of 400 A/m. The films had very weak in-plane magnetic anisotropy. Okumura *et al.* [24] prepared single and multilayer thin films of HITPERM/ SiO_2 using a target composition of $(\text{Fe}_{70}\text{Co}_{30})_{88}\text{Zr}_7\text{B}_4\text{Cu}_1$. Rf sputtering was employed for film deposition. The high frequency properties of the films were studied using FMR technique. It was found that the FMR damping were independent of film thickness which implied that damping is an intrinsic property. The coercivity showed a strong variation with film thickness. $\text{Fe}_{1-x}\text{Zr}_x$ alloys were produced by magnetron co-sputtering of Fe and Zr metals on glass substrate. It was found that amorphous Fe-Zr was formed when Zr concentration was at around 9 at% for room temperature deposition. The results showed that the amorphous phase formation at room temperature was a composition dependent phenomenon [25]. Luo *et al.* [26] prepared amorphous films of CoFeB, CoFeNiSiB and CoFeHfO by magnetron sputtering for application as soft ferromagnetic electrodes in tunneling magneto resistance (TMR) devices. The results indicated a large room temperature TMR effect of approximately 50%. Chen *et al.* [27] investigated the magnetic and electric properties of amorphous Co-Fe-Zr-B alloy thin films with Al and O additions, deposited on Si substrates by dc magnetron sputtering. The films deposited were amorphous. A strong uniaxial anisotropy was introduced in the film plane by annealing the film at 200°C under an external magnetic field of 150 Oe. Co-

Fe-Zr-B-Al-O film with 7% Al exhibited a low coercivity of ~ 1.4 Oe, a large anisotropy field of ~ 38 Oe and a high resistivity of $\sim 200 \mu\Omega\text{cm}$. It was also found that the soft magnetic properties of amorphous films had a strong dependence on the film composition. Contreras *et al.* [28] studied the effect of grain size on the soft magnetic properties of FeCoV/CoNbZr multilayers which was prepared by sequential rf sputtering. The coercivity followed a D^2 law in agreement with a random anisotropy model for two dimensional systems including the uniaxial anisotropy.

Vopseroiu *et al.* [29] describes the preparation of high moment CoFe films with controlled grain size and coercivity. CoFe films were prepared using a special plasma sputtering technology. Grain size of the films was controlled via the sputtering rate and coercivity followed a strong dependence on the grain size. Sun *et al.* [30] studied the soft magnetic properties of FeCoN films deposited on glass substrates by rf diode deposition technique. Good magnetic softness with a low coercivity of ~ 240 A/m (3 Oe) was achieved in FeCoN films on glass with thickness upto 640 nm. Ha *et al.* [31] reported the results of a systematic investigation of influences of the deposition conditions on the microstructure and magnetic properties of Co-Fe-V thin films. A strong modification in the coercivity with respect to film thickness and substrate temperature was observed. It was found that rapid annealing caused considerable changes in the microstructure and hence the magnetic properties of Co-Fe-V thin films.

Yokoshima *et al.* [32] prepared soft magnetic thin films with high saturation magnetic flux density B_s by electrodeposition. The B_s value obtained was around 23 kG and was comparable to that in bulk alloys. Coercivities of around 8 Oe was attained by annealing the films in vacuum under an external magnetic field. In addition to the high B_s , Co-Fe films were also resistant to corrosion. Liu *et al.* [33] describes the electro deposition of soft, high moment Co-Fe-Ni thin films. The alloy film exhibited

a saturation magnetization B_s of 20 kG, coercivity around 1 Oe, resistivity of $22 \mu\Omega\text{cm}$ and saturation magnetostriction of about 10^{-6} .

Berling *et al.* [34] deposited $\text{Fe}_x\text{Ni}_{100-x}$ nanometric films on SiO_2/Si substrate using the pulsed laser deposition technique. The deposition was carried out at room temperature. The results indicated that the electrical and magnetic properties were strictly dependent on the Fe-Ni compositional ratio. Amorphous films of FeSiB were obtained by thermal evaporation using a target of composition $\text{Fe}_{77.5}\text{Si}_{7.5}\text{B}_{15}$ [35]. The surface magnetic properties of such films were investigated using Magneto Optical Kerr Effect. The optimum heat treatment and magnetic field annealing induced better soft magnetic properties. Sun *et al.* [36] prepared nanocrystalline $\text{Fe}_{78}\text{Si}_{10}\text{B}_{12}$ thin film with a thickness of 100 nm by annealing its amorphous precursor. The amorphous films were prepared by rf sputtering method. The nanocrystalline films exhibited weak dense stripe domains. The stripe domains were due to the out-of-plane anisotropy exhibited by these films. Finemet type amorphous magnetic thin film samples with variable Cu content (up to 35 at%) were prepared by co-sputtering a target composed of original Finemet ribbons and simultaneously an appropriate amount of Cu onto partially oxidized Si (100) substrate [37].

Ha *et al.* [38] reported the nanostructure and magnetic properties of $\text{Co}_{19.35}\text{Fe}_{53.28}\text{Hf}_{7.92}\text{O}_{19.35}$ films prepared by reactive rf-sputtering. The films exhibited a high saturation magnetization, $4\pi M_s \sim 19.86$ kG, low coercivity $H_c \sim 1.5$ Oe and high hard axis anisotropy field of $H_k \sim 84$ Oe. Apart from exhibiting excellent magnetic properties the film possessed a very high electrical resistivity too. Wang *et al.* [39] reported the fabrication of $\text{Ni}_{0.81}\text{Fe}_{0.19}/(\text{Fe}_{0.7}\text{Co}_{0.3})_{0.95}\text{N}_{0.05}/\text{Ni}_{0.81}\text{Fe}_{0.19}$ sandwich structures in which the FeCoN film is 100 nm thick and each $\text{Ni}_{0.81}\text{Fe}_{0.19}$ Permalloy layer is 5 nm thick comprising only 4.5% of the volume of sandwich. The magnetic measurements showed that the films are promising for use in extremely high-density magnetic write heads as well as in integrated inductors operating in giga hertz range.

What is evident from these studies is that although researchers were successful in preparing glassy thin films and characterizing it for various properties, little has been done on understanding the effect of surface morphology as well as microstructure on the magnetic properties of ultra thin magnetic films. A systematic study is therefore required for having a clean correlation between the microstructure and the magnetic properties of thin films.

1.6 Some challenges in thin film magnetism

Soft magnetic properties exhibited by bulk (three dimensional) amorphous and nanocrystalline alloys were explained using the random anisotropy model proposed by Alben *et al* and later on modified by Herzer. On coming to a thin film system one has to consider the reduced dimensions while modelling the magnetic softness using random anisotropy model. Also in the reduced dimension (thin film form) the surface and interface properties greatly influence the overall magnetic behaviour of the system. The reduced symmetry, lower coordination number, and the availability of highly localized surface and interface states can induce new and interesting magnetic phenomena locally or only at the surface or interface. The existence of a surface can also affect the magnetic properties in the interior of the material, such as magnetic domain structure, domain wall motion and spin arrangements. Such changes extend from the surface into the interior to depths ranging from a few tens to several thousands of angstroms or more. The surface magnetization direction in thin magnetic films can be parallel, intermediate or perpendicular to the surface plane of atoms and is determined by the competition between magneto crystalline anisotropy (K_2 and K_4) and shape anisotropy ($2\pi M^2$) [40]. The surface anisotropy energy which governs the orientation of film's surface magnetization can be modified by film thickness, roughness, temperature and composition. By changing any of these parameters, the spontaneous magnetization of the surface can be made to switch directions and a magnetization reorientation is possible [41-44]. This transition is a result of

competition between spin orbit coupling, dipolar interaction and an external magnetic field that favours different magnetization directions. If surface profile is modulated, the direction of the magnetization within the film will wander and thus magnetization \vec{M} becomes a function of position, $\vec{M}(x)$. Hence magnetic fields of dipolar character are generated and a contribution to the anisotropy energy comes from this dipolar mechanism, which can result in an angular spread of magnetic moment in out-of plane directions.

Surface roughness can also have a pronounced effect on the properties of thin magnetic films, such as coercivity and magnetization reversal [45-47]. These magnetic properties greatly affect the applications of thin magnetic films in magnetic recording industry, as well as other applications in magneto electronics. Jiang *et al.* [48, 49] studied the relation of the coercivity versus surface roughness of Co ultrathin films deposited on an atomically flat Cu substrate. Vilain *et al.* [50] investigated the coercivity versus surface roughness of electrodeposited NiCo alloy films, and Malyutin, *et al.* [51] showed that the coercivity of chemically etched Ni-Fe-Co films increases with the surface roughness. Freeland *et al.* [52] using the x-ray resonant magnetic scattering studied hysteretic behaviour of CoFe thin films with varying roughness. They also found that the coercivity increased with the surface roughness. Li *et al.* [53] performed a detailed study of thin Co films deposited on plasma etched Si (100) films. They found that the uniaxial magnetic anisotropy decreases with the increase of surface roughness. Jiang *et al.* [48, 49] also investigated ultra thin Co films on an Ar-sputtered Cu substrate, and found that the coercivity increases with increasing surface roughness. Kim *et al.* [54] studied the under layer Si₃N₄ roughness on the coercivity of the Co/Pt multilayers. They also found that the coercivity enhanced with the increase of thickness /roughness of the Si₃N₄ under layer. So far there are only a few investigations discussing the correlation of surface/interface roughness with magnetic properties of thin films [55, 56]. This is probably due to the complicated nature of the

problem. Physically, all magnetic properties are related to the magnetic energy of a thin film. Besides surface/interface roughness, many other factors such as film thickness, composition, crystalline structure of the magnetic film, magnetic domain distribution and correlation contribute to the magnetic energy and determine the magnetization mechanism of a film. These are very important factors, and cannot be neglected in practice. However, in order to distinguish the effect of surface roughness on the magnetic properties, the contributions from other mechanisms has to be eliminated. Amorphous thin films will be an ideal candidate for such an investigation due to the absence of magneto crystalline anisotropy. Moreover thin film deposition by thermal evaporation offers us the advantages of controlling the composition and thickness of the film.

Apart from these issues relating the magnetism the main challenge is in the fabrication. That is how to assemble the soft magnetic nanostructures in an effective and controllable way. The capability of obtaining ordered arrays of well-defined and periodic soft magnetic nanostructures in an accurate, fast, and inexpensive fashion would be of great interest not only from an applied perspective but also from a fundamental point of view.

1.7 Magnetic nanostructures based on ferromagnetic alloys

With the advent of amorphous alloys exhibiting excellent soft magnetic properties, the nano structured form of this could find use in miniaturized magnetic devices. The integration of magnetic components into MEMS (MagMEMS) offers the advantages of implementing wireless technology. In comparison with other MEMS technologies, for example, those incorporating piezoelectric materials, MagMEMS offer a high power density, low performance degradation, fast response times and ease of fabrication. Further interest is in arrays of one dimensional magnetic structure due to their potential practical applications in high density recording media, magnetic

random access memory and their attraction as model systems to study fundamental physical properties of small magnetic particles.

So far there are four general methods that have been employed to fabricate nanostructures. They are nano lithography based methods, solution based methods, vapour based methods and template based methods.

Nano lithography based method uses advanced lithographic methods such as electron beam lithography, X-ray lithography etc. Most nanostructures fabricated by lithography are planar structures. However, this procedure is slow and expensive, and the aspect ratio of the vertical nanostructures is limited by the etching process. Also, it is not suitable for nanostructure fabrication in large scale.

The solution based approach employs controlled wet chemical reactions to synthesize nanostructures. Many of these processes are very complicated and require thorough understanding of the chemical reaction and crystal growth mechanism. Also the products are not pure and monodispersity of the sample is far from ideal.

Vapour based methods generally consists of vapour transport or vapour reactions at suitable temperature and pressure. These methods generally employ a catalyst to promote anisotropic crystal growth. In general, a specific catalyst must be chosen for each material, and the growth temperature is usually relatively high.

Template-based methods in general use anisotropic nano porous materials, such as anodized alumina, track etched polycarbonate membranes etc., to serve as hosts. The nano channels in the hosts may be filled using solutions, sol-gel, or vapour, to generate the desired nanostructures. The products can be taken from the templates by selectively removing the host material. Many different materials have been fabricated into nano wire/rod form based upon this processes. Most pure elements, especially metals and semiconductors, as well as compound semiconductors and oxides have already been fabricated into nano wires/rod structures.

However, there exists many challenges that most of these methods cannot meet: There is still no general methodology to prepare nanostructure from different materials, which makes the fabrication of hetero-nanostructure very difficult. Therefore it is essential to develop a versatile and reliable nano structure fabrication technique suitable for most material.

The techniques mentioned above are not sophisticated enough to manipulate diameters orientations, and positions of the grown nanostructures. The control of such growth is critical for future nano scale devices. Though there are a number of novel nano devices based on nanostructures that have been realized, the fabrication processes involved are usually either very complicated, or successful largely due to luck. The yields are low, and the properties of devices fabricated by the same method are not guaranteed to be identical. So far, there is no general or reliable method for fabricating large-scale nano devices.

It has been realized that by combining oblique angle deposition (OAD) and substrate positional control, one can produce different nano-sized columnar films with controlled porosity and shapes. Since OAD is a physical vapour deposition technique, it has many advantages in terms of controlling the growth of nano structured thin films: It can form nano-column array naturally. The porosity of the film can be controlled by simply changing the incident angle. There is no restriction on materials since the growth process is a thermal evaporation. It has the advantage of self-alignment due to the shadowing effect. It can also generate three-dimensional nanostructures. These advantages make the OAD technique very promising for nanostructure fabrications.

To date, ferromagnetic nano columns have been grown by vapour phase co-deposition and oblique angle vapour deposition [57-60]. Fe-Ni-Co nano columns were grown by the self organization of vapour phase co-deposited Fe-Ni-Co [58]. Nano

columns with Co/Cu bilayers were obtained by two-source oblique angle vapour deposition [59].

Even though there exists few literature reports in the field of metal nano columns, little has been done on the growth of amorphous alloy nano columns.

1.8. Motivation for the present work

Based on the above discussions it is seen that amorphous alloys and its nanocrystalline counterparts are promising for soft magnetic applications. Metglas 2826 MB ($\text{Fe}_{40}\text{Ni}_{38}\text{Mo}_4\text{B}_{18}$) is a soft magnetic alloy that exhibits superior soft magnetic properties. Its softness after nano crystallisation can be ascribed to its bi phasic nature consisting of Fe-Ni nano crystals embedded in the remaining boron rich amorphous matrix. Additives like boron and molybdenum are incorporated in the alloy to achieve specific objectives. Boron aids in retaining the glassy characteristics while molybdenum is a known grain growth inhibitor. However, high metalliod content causes deterioration not only in the magnetic properties but also in elasticity and plasticity [61]. If B and Mo can be dispensed with in FeNi based alloys like Metglas, this brings in economy and is an attractive proposition from a commercial point of view. Since Metglas is widely used for sensor applications, thin film form of this material would be of great interest for integrating thin film sensors with today's microelectronics. This can be realized by depositing thin films of this material on suitable substrates. Although some researchers were successful in fabricating thin films of amorphous alloys, little has been done to understand the intricate relation ship between their magnetic properties and micro/surface structure. Also in these investigations the composition of the film was not ascertained and the nature of the microstructure was not established by any experimental techniques. Such a study only will give credence in correlating the microstructure with magnetic properties. Further, the amorphous interlayer in nanocrystalline magnetic material plays a crucial role in determining the magnetic and electronic properties. Hence employment of

sophisticated techniques like transmission electron microscopy in characterizing the material assumes significance from an application point of view. It is in this context that a systematic investigation on a magnetic soft alloys based on Fe-Ni assumes significance.

It is well known that the magnetic properties of a thin film strongly depend on the surface roughness. Ion irradiation has been considered as an alternative tool in modifying the surface properties. The surface evolution of a thin film under swift heavy ion irradiation will be an outcome of a competition between sputtering induced surface roughening process and the material transport induced smoothing process. Considering the prospects of fabricating thin films based on Fe-Ni from metallic glass ribbons by simple vacuum evaporation techniques and the fact that amorphous alloys are not resistant to irradiation induced damages, a detailed investigation in probing the surface modification of amorphous thin films of Fe-Ni is worthwhile. It was thought that swift heavy ions would modify the surface structure of these alloys and will eventually lead to modification of magnetic properties. Further, the studies relating to SHI induced surface modifications and the intrinsic magnetic properties of thin films are rather scarce or seldom reported. The impingement of ions with different fluence on the alloy is bound to produce systematic microstructural changes and if these changes produce a pattern, this could effectively be used for tailoring the coercivity of these materials. The in situ method of tailoring coercivity using swift heavy ion is novel and is an ingenious tool in creating surface modification which will eventually lead to changes in the bulk property. AFM is a promising tool for such a study on ion bombarded films where a minimum sample preparation is required. It offers a good lateral resolution too.

Fabrication of nanocolumnar structures of amorphous alloys by oblique angle deposition will be of great interest to scientific community. Isolated magnetic nanostructures are promising for high density magnetic recording, sensors and

magnetic random access memories. Further, they are ideal platform for studying fundamental physical properties of small magnetic particles. Generally, the morphology of the nanostructures obtained by OAD is influenced by the substrate surface roughness and the growth conditions used for the film formation along with oblique angle, deposition rate, deposition time etc. The growth of nano structures will be the resultant of the competition between the smoothing due to adatom surface diffusion and roughening by self shadowing. For the synthesis of well defined nanostructures having appropriate separation and clear surface morphologies, an understanding on the interplay between the mechanisms involved in the growth process is essential. From an applied stand point, detailed knowledge of the growth behaviour of the nanostructures on a solid surface will aid in synthesizing nanostructures with well defined roughness and geometry.

Moreover, the as prepared amorphous magnetic thin films usually present high coercivity due to stresses in the films. The magnetic property of such films strongly depends on the magnitude of magnetoelastic anisotropies. So the measurement of magnetostriction is also important in the study of the amorphous ferromagnetic thin films. Optical fibre long period grating (LPG) can be utilized to quantify the magnetostriction in thin films. It is a non destructive technique. Optical fibre long period grating based sensing methods offer other advantages of electromagnetic interference immunity, compactness, ease of fabrication and multiplexing.

It is one of the objectives of this work to fabricate thin films and nano columnar structures of Fe-Ni based amorphous alloys and put forward a clean correlation between the Fe-Ni thin film surface/microstructure and magnetic properties. Attempts will be made to integrate Fe-Ni amorphous thin films to an optical fibre long period grating for potential magnetostrictive sensor applications. Aid of state of the art techniques like Atomic Force Microscopy, Magnetic Force

Microscopy, Ferro Magnetic Resonance, Vibrating Sample Magnetometer and Transmission Electron Microscopy will be utilized for this study.

1.9. Objectives

The main objectives of the present work can be as follows.

- Fabrication of Fe-Ni based amorphous thin films and their structural and magnetic characterisation.
- Fabrication of nanocrystalline thin films of Fe-Ni by the crystallisation of its amorphous precursor. Controlling the coercivity in such films by having a control on the nanocrystallite size.
- Surface modification of amorphous Fe-Ni thin films by swift heavy ion irradiation for tailoring the coercivity, remanence, demagnetising field and saturating field.
- Surface modification of Fe-Ni thin films by thermal annealing and its effect on the in-plane and out-of-plane demagnetisation fields.
- Fabrication of nanocolumnar structures of Fe-Ni by oblique angle vapour deposition and studying the effect of deposition conditions on the growth process of the nanocolumns.
- Studying the effect of substrate surface roughness on the surface evolution and magnetic properties of amorphous Fe-Ni nanocolumns.
- Characterising Fe-Ni amorphous thin films for possible magnetostrictive sensor applications.

Theory of magnetism in metallic alloys

Contents

- 2.1 Magnetic dipole moments and magnetization
- 2.2 Ferromagnetic ordering (Curie) temperatures
- 2.3 Magnetic anisotropies
- 2.4 Magnetic domains and domain wall mobility
- 2.5 Random anisotropy
- 2.6 Technical magnetization
- 2.7 Magnetostriction

This chapter gives a brief introduction to the theory of magnetism in metallic alloys.

2.1. Magnetic dipole moments and magnetization

The vast majority of soft magnetic materials have one or more of the ferromagnetic transition metal elements, Fe, Co or Ni, or the rare earth metal Gd as a majority component. The magnetic dipole moments of elemental and alloy magnets are most completely understood through the band theory of solids [1,62-65]. The band theory of solids considers the broadening of localized atomic states with discrete eigen values into a continuum of states for more itinerant electrons over a range of energies. The theory allows for calculation of energy dispersion (i.e. energy as a function of wave vector) and orbital angular momentum specific and spin-resolved densities of states. The calculation of spin-resolved energy bands and densities of states allows for the description of atom resolved magnetic dipole moments and, therefore, spontaneous magnetization of elemental and alloy magnetic solids. Among the successes of the band theory descriptions of magnetic properties are:

1. The prediction of non-integral or half integral atomic dipole moments and resulting ground state magnetizations in metals and alloys.

2. The prediction that band widths and exchange splitting (energy differences between spin up and spin down bands) are intimately dependent on magnetic coordination number and atomic volume.

Table 1 summarizes absolute zero and room temperature magnetizations and atomic dipole moments for some important transition metal and rare earth elemental magnets. Also shown are Curie temperatures (ferromagnetic ordering temperatures) which are not ground state properties that are directly calculable from band theory.

Table 2.1 Spontaneous and room temperature magnetizations, magnetic dipole moments, and Curie temperature for elemental ferromagnets (adapted from Ref. [1]).

Element	$\mu_m @ 0K$ (μ_B)	$M_s @ 0K$	$M_s @ RT$	T_C (K)
Fe	2.22	1740	1707	1043
Co	1.72	1446	1400	1388
Ni	0.606	510	485	627
Gd	7.63	2060	-	292
Dy	10.2	2920	-	88

Fig. 2.1 shows the Slater-Pauling curve that illustrates the variation of the mean atomic magnetic dipole moment as a function of composition in transition metal alloy systems. For magnetic alloy design the Slater-Pauling curve is an important starting point. The desire for large induction limits the choice of alloys to those rich in Fe or Co and therefore near the top of the Slater-Pauling curve. As described in the Slater-Pauling curve Fe-Co alloys exhibit the largest magnetic inductions of any material, and also have Curie temperatures which are desirable for high temperature applications. Alloys near the equiatomic composition are particularly soft and exhibit large permeabilities, but this magnetic softness is rooted in small values of the first-

order magnetic anisotropy constant, K_1 . Fe-rich alloys typically have smaller inductions and lower Curie temperatures than Fe-Co alloys. Fe-Si is another premiere crystalline soft material whose significant application includes transformer laminate. Co alloys can also be soft but only if the FCC phase of Co is present. Co-rich alloys typically have smaller inductions and larger T_C 's.

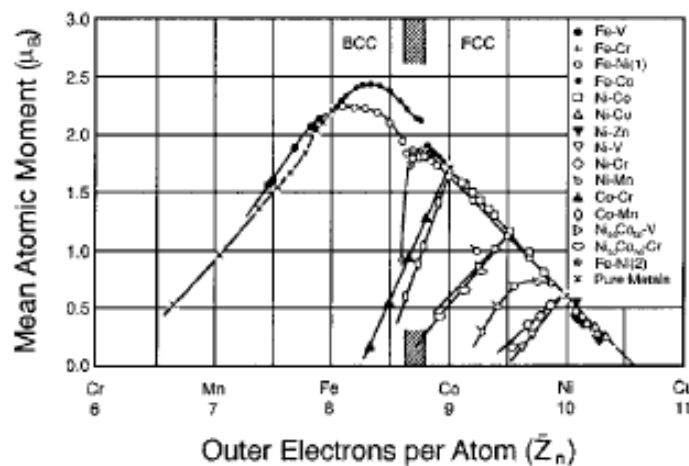


Fig.2.1 Slater-Pauling curve (adapted from Ref. [1])

2.2. Ferromagnetic ordering (Curie) temperatures

Ferromagnetism is a cooperative phenomenon since individual atomic moments interact so as to promote alignment with one another. This collective interaction gives rise to the temperature dependence of the magnetization. Two models have explained the interaction between atomic moments. Mean Field Theory considers the existence of a non-local internal magnetic field, called the Weiss field, which acts to align magnetic dipole moments even in the absence of an applied field H . Heisenberg Exchange Theory considers a local (usually nearest neighbour)

interaction between atomic moments (spins) which acts to align adjacent moments even in the absence of a field.

The basic assumption of the mean field theory is that this internal field is non-local and is directly proportional to the sample magnetization, $H_{INT} = \lambda_w M$, where the constant of proportionality, λ_w , is called the Weiss molecular field constant. To consider ferromagnetic response in an applied magnetic field, H , as well as the randomizing effects of temperature, we consider the superposition of the applied and internal magnetic fields. By analogy with the problem of paramagnetic moments, the average atomic dipole moment can be expressed in terms of the Brillouin function $\langle \mu_m \rangle = \mu_m^{atom} B_J(a')$, where $a' = \left(\frac{\mu_0 \mu_m^{atom}}{k_B T} \right) (H + \lambda_w M)$ for a collection of classical dipole moments. Similarly, the saturation magnetization can be written

$$\text{as } M_s = N_m \langle \mu_m^{atom} \rangle \text{ and } \frac{M}{N_m \mu_m^{atom}} = \frac{M}{M_s} = B_J(H + \lambda_w M)$$

Under appropriate conditions, this leads to solutions for which there is a non-zero magnetization (spontaneous magnetization) even in the absence of an applied field. For $T > T_C$, the ferromagnetic Curie temperature the only solution to the above equation is at $M=0$, i.e., no spontaneous magnetization and thus paramagnetic response. For $T < T_C$, we obtain solutions with a non-zero, spontaneous, magnetization, the defining feature of a ferromagnet.

The Heisenberg model considers ferromagnetism and the spontaneous magnetization resulting from nearest neighbour exchange interactions, which act to align spins in a parallel configuration, instead of a non-local, mean field. The Heisenberg model can be further generalized to account for atomic moments of different magnitude and signs, i.e., in alloys, and for exchange interactions, which act to align nearest neighbour moments in an anti-parallel fashion, or in a non-collinear relationship. In Heisenberg ferromagnet the atomic moments (due to a spin vector S)

on nearest neighbour sites are coupled by a nearest neighbour exchange interaction and this gives rise to a potential energy:

$$E_p = -J_{ex} \mathbf{S}_i \times \mathbf{S}_{i+1} \quad 2.1$$

Here $J_{ex} > 0$ favours parallel alignment of the spins. The exchange energy, suitably scaled, replaces the Weiss molecular field constant in the mean field theory of ferromagnetism to explain the temperature dependence of the magnetization.

Ferromagnetic exchange interactions set the scale for Curie temperatures in ferromagnetic alloys. Interatomic exchange couplings can be calculated from first principles by considering the energy change associated with rotation of individual spins in the host material. These exchange interactions can be used within a mean field theory to estimate the Curie temperature. An empirical description of the variations of the exchange energy with interatomic spacing called the Bethe-Slater curve is instructive in describing the effect of alloying on ferromagnetic Curie temperatures. In 3d transition metal solids, the Bethe-Slater curve, shown in Fig. 2.2 predicts the sign of the exchange interaction. The interplay between electron-electron Coulomb interactions and the constraints of the Pauli's exclusion principle determine the sign of the exchange interaction. In transition metal solids a measure of the overlap between nearest neighbor d-orbitals is given by the ratio of the atomic to the 3d ionic (or nearest neighbor) radius. In mean field theory the Curie temperature can be related to the exchange energy as follows:

$$T_C = \frac{2ZJ_{ex}S(S+1)}{3k_B} \quad 2.2$$

where Z is the nearest neighbor coordination number and S is the total spin angular momentum.

Alloying effects and the effects of disorder can be qualitatively understood from Eq. 2.2 and the Bethe-Slater curve (Fig. 2.2). From the shape of the Bethe-Slater curve and the relative positions of Fe and Co on the curve it can be inferred, for example, that

M(I) in Co-based alloys will be relatively invariant to disorder as compared with Fe-based alloys [1]. In the amorphous phase, structural fluctuations give rise to fluctuations in the exchange interactions.

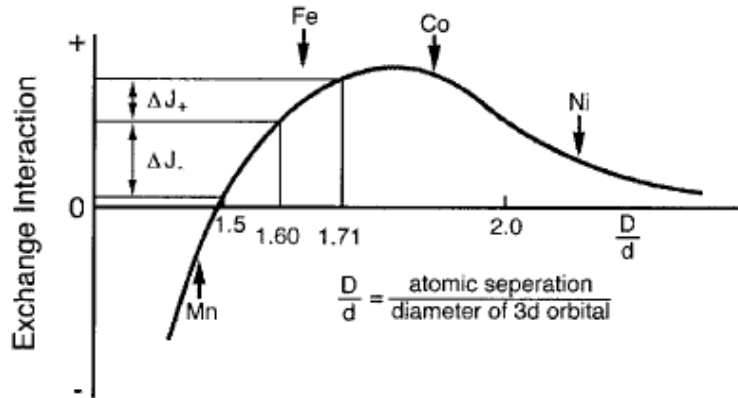


Fig.2.2 Bethe-Slater curve for the magnetic exchange interaction energy as a function of interatomic spacing (normalized by the spatial extent of the magnetic 3d orbitals). Also showing large variations of J with positions on the left of the curve [1]

A first order theory as to the fluctuation in the exchange interactions with fluctuations in interatomic spacing can be offered by considering a Taylor series expansion of the exchange interaction as a function of nearest neighbor spacing of the form:

$$J_{ex} = J_{ex}^0 + \left(\frac{\partial J_{ex}}{\partial X} \right)_{x_0} \Delta X + \dots \quad 2.3$$

It can be readily seen that alloys which have exchange energies, J_{ex}^0 , which lie near the peak in the Bethe-Slater curve (see Fig. 2.3 (b)) (e.g., Co, FeCo) will be relatively insensitive to fluctuations in the interatomic separation since $\frac{dJ}{dx} \sim 0$. On the other hand, alloys for which J_{ex}^0 lies well away from the peak (e.g. Fe- and Ni- based alloys

2.3 Magnetic anisotropies

A magnetization curve illustrates the technical magnetic properties of a ferromagnetic material. Its shape is determined by minimizing the material's magnetic free energy. The magnetic free energy consists of terms associated with the field energy (Zeeman energy), self-field (demagnetization energy), wall energy, and magnetic anisotropy energy [63].

The term magnetic anisotropy refers to the dependence of the magnetic properties on the direction in which they are measured. The magnitude and type of magnetic anisotropy affect properties such as magnetization and hysteresis curves in magnetic materials. As a result the nature of the magnetic anisotropy is an important factor in determining the suitability of a magnetic material for a particular application. The direction of a magnetization relative to body that supports it is determined mainly by two effects, shape anisotropy and magnetocrystalline anisotropy. The first arises from magnetostatic effects and the second from spin-orbit coupling between the spins and the lattice of the material.

2.3.1 Magnetocrystalline anisotropy

The tendency of the magnetization to align itself along a preferred crystallographic direction is referred to as magnetocrystalline anisotropy. Magnetocrystalline anisotropy energy is defined as the energy difference between samples magnetized along easy and hard directions.

A schematic result for single-crystal samples of magnetite is shown in figure 2.4. Depending on the crystallographic orientation of the sample in the magnetic field, the magnetization reaches saturation in different fields. In magnetite (Fe_3O_4), above 130 K, $\langle 111 \rangle$ is the easy direction of magnetization, $\langle 100 \rangle$ is the hard direction of magnetization and $\langle 110 \rangle$ is the intermediate direction of magnetization. Body centred cubic Fe has the $\langle 100 \rangle$ direction as its easy axis. In Ni, which is face-centred cubic,

the easy axis is $\langle 111 \rangle$. Note that the final value of the spontaneous magnetization is the same, no matter which axis the field is applied along, but the field required to reach that value is distinctly different in each case.

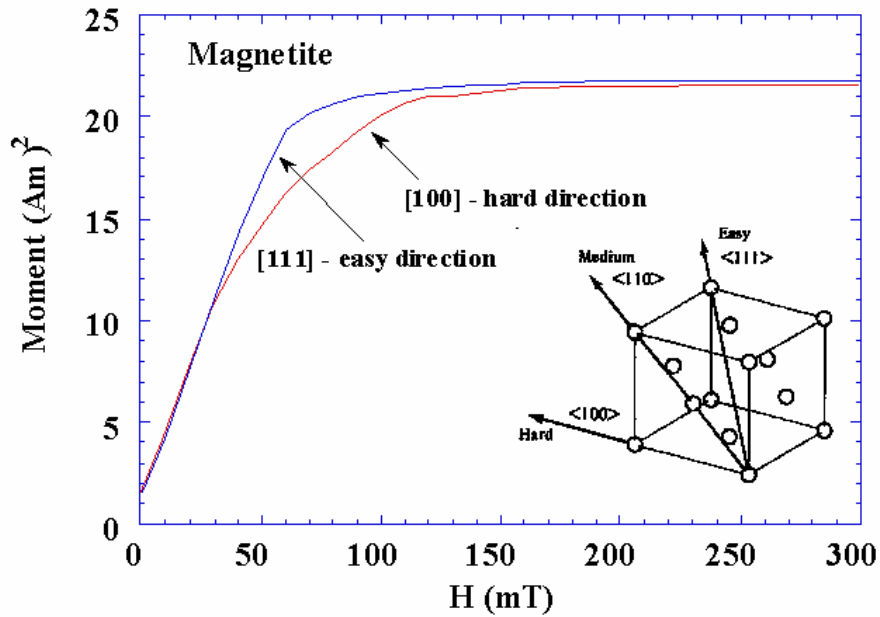


Fig. 2.4 Magnetisation curve for single-crystal magnetite along easy and hard axis

The symmetry of the magnetocrystalline anisotropy is always the same as that of the crystal structure. As a result, in iron, which is cubic, the anisotropy energy, E , can be written as a series expansion of the direction cosines α_i , of the saturation magnetization relative to the crystal axes.

$$E = K_1(\alpha_1^2\alpha_2^2 + \alpha_2^2\alpha_3^2 + \alpha_3^2\alpha_1^2) + K_2(\alpha_1^2\alpha_2^2\alpha_3^2) + \dots \quad 2.4$$

Here K_1 , K_2 etc are called the anisotropy constants. The energy E is that stored in the crystal when work is done against the anisotropy ‘force’ to move the magnetization away from an easy direction.

Cobalt is hexagonal, with the easy axis along the hexagonal (c) axis. The anisotropy energy is uniaxial and its angular dependence is a function only of the angle θ between the magnetization vector and the hexagonal axis.

In this case the anisotropy energy can be expanded as

$$E = K_1 \sin^2 \theta + K_2 \sin^4 \theta + \dots \quad 2.5$$

The energy required to rotate the spin system of a domain away from the easy direction is actually just the energy required to overcome the spin-orbit coupling. When an applied field tries to reorient the direction of the electron spin, the orbit also needs to be reoriented, because of the spin-orbit coupling. However the orbit is also strongly coupled to the lattice, and so the attempt to rotate the spin axis is resisted.

Since the magnetic anisotropy represents a barrier to switching the magnetization, for soft magnetic materials, a small magnetic anisotropy is desired so as to minimize the hysteretic losses and maximize the permeability. The desire for small magnetocrystalline anisotropy necessitates the choice of cubic crystalline phases of Fe, Co, Ni or alloys such as FeCo, FeNi, etc. (with small values of K_1). In crystalline alloys, such as permalloy or FeCo, the alloy chemistry is varied so that the first order magnetocrystalline anisotropy energy density, K_1 , is minimized. Similarly, stress anisotropy is reduced in alloys with nearly zero magnetostriction. Shape anisotropy results from demagnetization effects and is minimized by producing materials with magnetic grains with large aspect ratios. Amorphous alloys are a special class of soft

materials where (in some notable cases) low magnetic anisotropies result from the lack of crystalline periodicity.

2.3.2 Shape anisotropy

Although most materials show some magnetocrystalline anisotropy, a polycrystalline sample with no preferred orientation of its grains will have no overall crystalline anisotropy. However only if the sample is exactly spherical will the same field magnetize it to the same extent in every direction. If the sample is not spherical, then it will be easier to magnetize it along a long axis. This phenomenon is called shape anisotropy.

2.3.2.1 Demagnetizing field

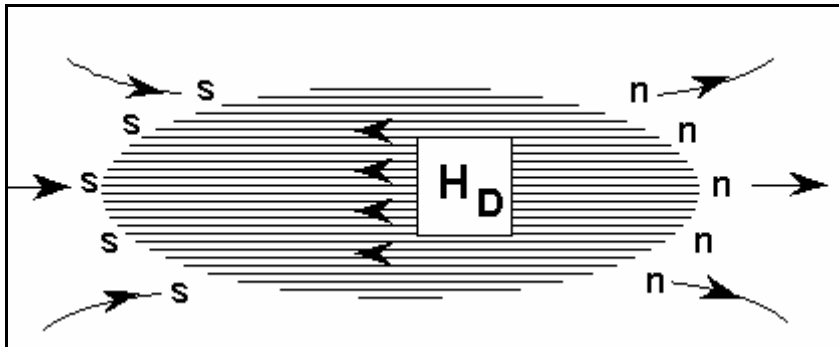


Fig. 2.5 Schematic representation of demagnetising field in a prolate spheroid

Consider a prolate spheroid shown in figure 2.5. Let it be magnetized by a magnetic field from left to right. This results in North Pole at the right end and South Pole at the left end. By definition, the lines of magnetic field radiate from the North Pole and end at the South Pole, resulting in the pattern of field lines shown in figure 2.5. We see from the figure, that the field inside the sample points from right to left-

that is in the opposite direction to the applied external field. This internal field tends to demagnetize the material and so we call it the demagnetizing field H_D .

The demagnetizing field is created by the magnetization of the sample, and in fact the size of the demagnetizing field is directly proportional to the size of the magnetization [63].

$$H_D = N_D \cdot M \quad 2.6$$

Where N_D is called the demagnetizing factor, and depends only on the shape of the sample. For elongated samples, N_D is smallest along the long axis and largest along the short axis. The anisotropy becomes stronger as the aspect ratio increases with $N_D \rightarrow 0$ as the distance between the 'poles' $\rightarrow \infty$.

Moreover, the effective field acting inside the material, H_{eff} , is smaller than the applied field by an amount equal to the demagnetizing field. That is

$$H_{eff} = H_{applied} - H_D \quad 2.7$$

So along the long axis, where N_D is small,

$$H_{eff} = H_{applied} - N_D M \approx H_{applied} \quad 2.8$$

and most of the applied field goes into magnetizing the sample. By contrast, along the short axis N_D is large, so

$$H_{eff} = H_{applied} - N_D M < H_{applied} \quad 2.9$$

and so most of the applied field goes into overcoming the demagnetizing field. As a consequence it is easier to magnetize the sample along the long axis.

2.4 Magnetic domains and domain wall mobility

In a ferromagnet there are macroscopic volumes, called magnetic domains, over which atomic magnetic moments are aligned due to the internal (Weiss) field or alternatively the ferromagnetic exchange interaction. In a typical magnetic material a

macroscopic volume of the material contains many domains. Each of these domains has a spontaneous magnetization of magnitude, M_s . In the absence of an aligning field the magnetization vectors are aligned differently from domain to domain. Thus if we take the vector average of the magnetization over many domains we arrive at zero sample magnetization, $\langle M \rangle = 0$, because of vector cancellation of the random domain moments. The magnetization process involves the growth of domains that are favorably oriented with the applied magnetic field at the expense of those that are not [63-65].

Having more than one domain requires an interfacial region between domains called a domain wall. Associated with this interface is positive domain wall energy. The ultimate number and size, of magnetic domains in a sample is determined by a balance between the volume, magnetostatic, and interfacial domain wall energies. In soft materials, which have been optimized to have very low rotational energy barriers, the major determinant of the shape of the magnetization curve is domain wall motion.

The energy per unit area in the wall of thickness $\delta = Na$ can be expressed as a sum of exchange and anisotropy energy terms:

$$\gamma_d = \gamma_{ex} + \gamma_{an} = \frac{J_{ex} S^2 \pi^2}{\delta a} + K \delta \quad 2.10$$

This energy has a minimum for a particular value of δ .

This minimum is given by

$$\frac{d\gamma_d}{d\delta} = -\frac{J_{ex} S^2 \pi^2}{\delta^2 a} + K = 0 \quad 2.11$$

OR

$$\delta = \sqrt{\frac{J_{ex} S^2 \pi^2}{Ka}} \quad 2.12$$

The exchange integral J_{ex} is proportional to the Curie temperature T_C , there fore

$$\delta = \sqrt{\frac{T_c}{K}} \quad 2.13$$

The smaller the anisotropy constant, the thicker the domain wall. Therefore, wall thickness increases with temperature, because K almost always decreases with rising temperature. Expressed in terms of the exchange stiffness, A , the domain wall width δ

$$\text{is } \delta = \pi \sqrt{\frac{A}{K}}$$

The distance over which the perturbation due to the switching of a single spin decays in a soft material is called the ferromagnetic exchange length, L_{ex} , and can be expressed

$$\text{as } L_{ex} = \sqrt{\frac{A}{\mu_0 M_s^2}} \quad 2.14$$

Structure sensitive magnetic properties may depend on defect concentration (point, line and planar defects), atomic order, impurities, second phases, thermal history, etc. In multi-domain materials, the domain wall energy density $\gamma_d = 4\sqrt{AK} = \gamma_d(x)$ is spatially varying as a result of local variations in properties due to chemical variation, defects, etc. A domain wall will prefer to locate itself in regions where the magnetic order parameter is suppressed, that is pinning sites. Since changes in induction in high-permeability materials occur by domain wall motion, it is desirable to limit variation of $\gamma_d(x)$ (pinning). This is one of the key design issues in developing soft magnetic materials, that is that of process control of the microstructure so as to optimize the soft magnetic properties.

2.5 Random anisotropy

The magnetic properties of an assembly of small grains depend strongly on the counterplay of local magnetic anisotropy energy and ferromagnetic exchange energy. For large grains the magnetization can follow the easy magnetic directions in the single grains and domains can be formed within the grains. The magnetization process, thus,

is determined by the magneto-crystalline anisotropy K_1 of the crystallites. For very small grains, however, ferromagnetic exchange interaction more and more forces the magnetic moments to align parallel, thus, impeding the magnetization to follow the easy directions of each individual grain. As a consequence the effective anisotropy for the magnetic behaviour is an average over several grains and, thus, reduced in magnitude. The dividing line between these two cases is given by the ferromagnetic exchange length

$$L_{ex} = \sqrt{\frac{A}{\langle K \rangle}} \quad 2.15$$

(A denotes the exchange stiffness) which is a basic parameter in domain wall theory representing a characteristic minimum scale over which the magnetization can vary appreciably.

2.5.1 Small grains (random anisotropy model)

In order to interpret the behaviour of the magnetic properties for very small grain sizes the random anisotropy model originally proposed by Alben *et al.* [66] for amorphous ferromagnets can be made used. The basic idea is sketched in figure 2.6 and starts from an assembly of ferromagnetically coupled grains of size D with magneto-crystalline anisotropies K_1 oriented at random. The effective anisotropy affecting the magnetization process results from averaging over the $N = \left(\frac{L_{ex}}{D}\right)^3$ grains

within the volume $V = L_{ex}^3$ of the exchange length. For a finite number, N, of grains there will always be some easiest direction determined by statistical fluctuations.

As a consequence the resulting anisotropy density $\langle K \rangle$ is determined by the mean fluctuation amplitude of the anisotropy energy of the N grains, i.e.

$$\langle K \rangle = \frac{K_1}{\sqrt{N}} = K_1 \left(\frac{D}{L_{ex}}\right)^{\frac{3}{2}} \quad 2.16$$

In turn the exchange length L_{ex} now is related self-consistently to the average anisotropy by substituting $\langle K \rangle$ for K_1 in eq. 2.15, i.e.

$$L_{ex} = \sqrt{\frac{A}{\langle K \rangle}} \quad 2.17$$

This renormalization of L_{ex} results from the counterplay of anisotropy and exchange energy: as magneto-crystalline anisotropy is suppressed by exchange interaction the scale on which exchange interactions dominate expands at the same time and, thus, the local anisotropies are averaged out even more effectively. The combination of eqs.2.16 and 2.17 finally yields

$$\langle K \rangle \sim \frac{K_1}{A^3} D^6 \quad 2.18$$

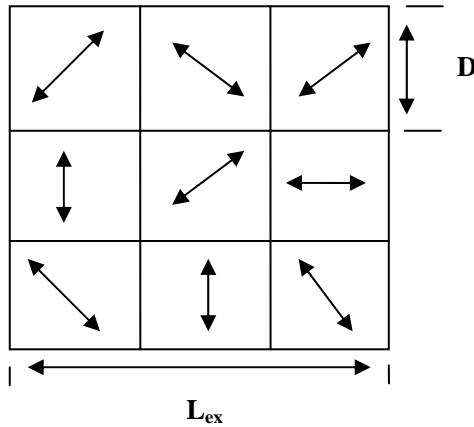


Fig. 2.6 Schematic representation of the random anisotropy model. The arrows indicate the randomly fluctuating magneto-crystalline anisotropies.

which holds as long as the grain size D is smaller than the exchange length L_{ex} . It should be noted that this result is essentially based on statistical and scaling arguments and, therefore, is not limited to the case of uniaxial anisotropies (as may be anticipated from Figure 2.6) but also holds for cubic or other symmetries [67,68]. The most significant feature of the above analysis is the strong variation, of $\langle K \rangle$ with the sixth

power D^6 of the grain size. If coercivity is related to $\langle K \rangle$ using the results for coherent spin rotation we find

$$H_c = p_c \frac{\langle K \rangle}{M_s} \sim \frac{p_c K_1 D^6}{M_s A^3} \quad 2.19$$

Where K_1 is the magnetocrystalline anisotropy constant, M_s is the saturation magnetization, A is the exchange constant and p_c is a dimensionless quantity related to the crystal structure.

Accordingly the sensitive grain size dependence of $\langle K \rangle$ should be also reflected in the soft magnetic properties. It should be finally noted that the above results for H_c is not bound to the case of coherent magnetization rotation. Indeed, the same final result can be derived assuming domain wall pinning as the prevailing magnetization mechanism.

2.5.2 Random anisotropy model extended to two dimensional systems (thin films)

If one of the dimensions of the nanocrystalline material is smaller than the exchange correlation length (L_{ex}), the averaging effect of anisotropies can be confined to two dimensions [69, 70].

$$\text{Then } \langle K \rangle = \frac{K_1}{\sqrt{N}} = K_1 \left(\frac{D}{L_{ex}} \right) \quad 2.20$$

Substituting (2.15) in (2.20) we get

$$\langle K \rangle = \frac{K_1^2}{A} D^2 \quad 2.21$$

$$\text{Therefore } H_c = p_c \frac{\langle K \rangle}{M_s} \sim \frac{p_c K_1^2 D^2}{M_s A} \quad 2.22$$

This equation suggests that for two dimensional systems the Herzer's D^6 law has to be replaced by the D^2 law.

2.6 Technical magnetization

When a magnetic field is applied to a ferromagnetic substance, the domain structure changes in such a way as to increase the resultant magnetization parallel to the external field. This process is called technical magnetization. The boundary between the domains—the domain wall—plays an important role in the technical magnetization. Inside the domain wall the spins rotate gradually from one domain to the next.

Consider the wall displacement in the domain structure shown in figure 2.7. When the external field is applied parallel to the magnetization of one domain the spins inside both domains experience a torque resulting from the field simply because their directions are either parallel or anti parallel to the field. Since the spins inside the wall do make some angle with the field direction, they, under the action of a torque, start to rotate toward the field direction. As a result of the rotation of the spins inside the wall, the centre of a wall should be displaced as seen in figure 2.7 (b), resulting in an increase in the volume of the domain which has its magnetization parallel to the external field. This process is called domain wall displacement.

Consider wall displacement in the domain structure shown in figure 2.8, which was actually observed on a Si-Fe (001) surface. When the field is applied parallel to one of the [100] direction as shown in figure 2.9(a), the domains which have their magnetization parallel to the field should increase their volume at a sacrifice to the other domains and finally cover the whole volume of the specimen. Since there can be no further changes in the magnetization, this state corresponds to the saturation magnetization.

When the field is applied in a [110] direction [figure 2.9(b)], the two kinds of domains whose magnetization directions are closest to the field direction increase their volume and finally cover the whole volume of the specimen. If the field is increased

further, the magnetizations in each domain rotate from the easy directions to the field directions, and finally the specimen reaches saturation magnetization.

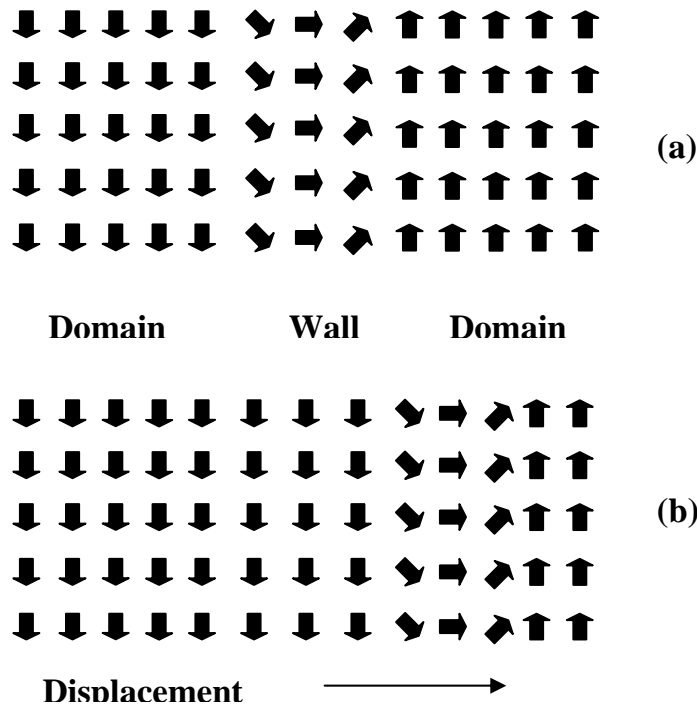


Fig. 2.7 Schematic of domain wall displacement

The magnetization curves corresponding to the process mentioned above should be like those in figure 2.10. The curves in this figure are the actual magnetization curves measured for single crystals of iron. In [100] magnetization, the entire process is performed by wall displacement which attained in a weak field, so that the magnetization curve reaches saturation in a weak field. On the contrary, [110] and [111] magnetizations require fairly large magnetic field to attain saturation magnetization, because in most cases the rotation magnetization required fairly large amount of energy other wise called magnetic anisotropy energy.

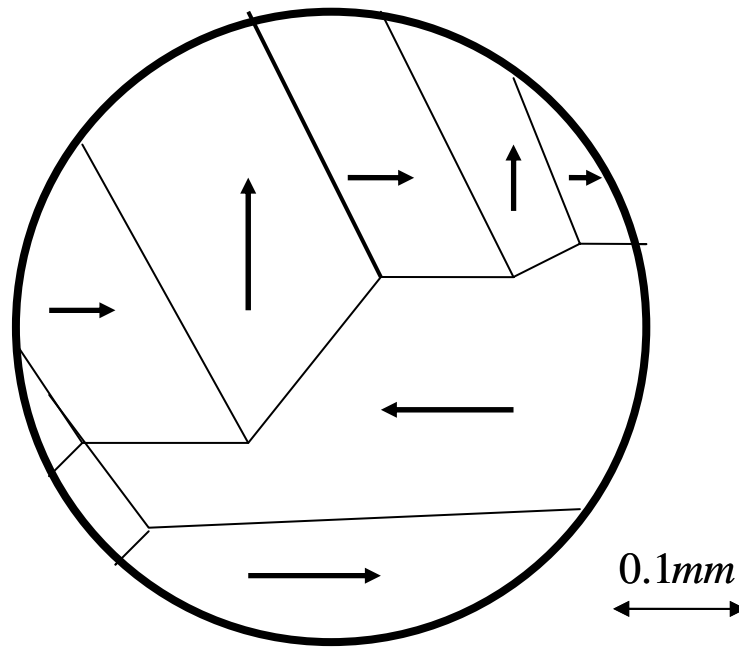


Fig. 2.8 Typical domain structure on a Si-Fe (001) surface

Magnetic materials can be classified into two groups homogeneous and inhomogeneous. In inhomogeneous magnetic materials, the displacement of wall requires a fairly large magnetic field, so that the magnetization curve is bent from the initial stage of magnetization. Another feature of inhomogeneous magnetic materials is that the stable domain structure is not a unique function of the applied field. The domain structure which is attained by increasing the field to H is different from that attained by decreasing the field from a high value to H , so that the intensity of magnetization is different for both cases. This is why the magnetization of ferromagnetic substances shows hysteresis.

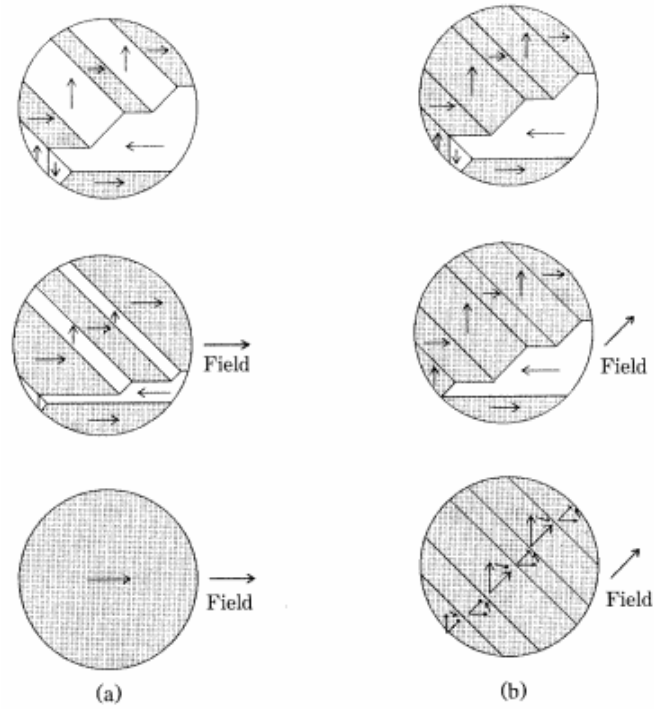


Fig. 2.9 Changes in the domain structure of a crystal of iron (schematic). **a)** Magnetic field in [100] direction **b)** field along [110] direction

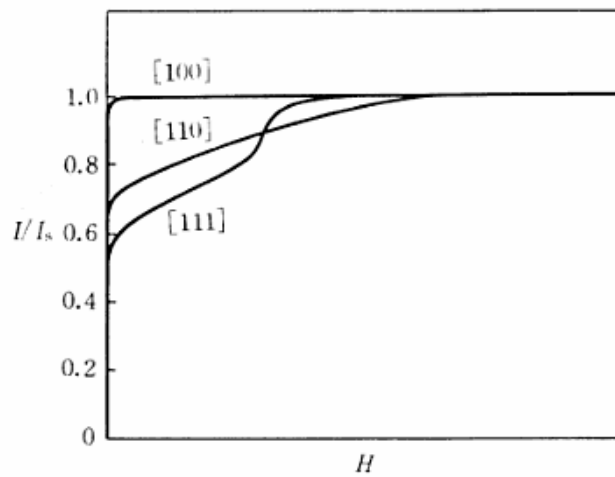


Fig. 2.10 Magnetisation curves for single crystals of iron (adapted from ref [64])

2.7 Magnetostriction

When a substance is exposed to a magnetic field, its dimension will change. This effect is called magnetostriction. The fractional change in length $\frac{\Delta l}{l}$ is simple a strain and to distinguish it from the strain ε caused by an applied stress, we give the magnetically induced strain as a special symbol λ :

$$\lambda = \frac{\Delta l}{l} \tag{2.23}$$

the value of λ measured at magnetic saturation is called saturation magnetostriction λ_s .

Magnetostriction occurs in all pure substances. However even in strongly magnetic substances, the effect is small: λ_s is typically of the order of 10^{-5} . Although the direct magnetostrictive effect is small there exists an inverse effect which causes such properties as permeability and the size of the hysteresis loop to be highly dependent on stress in many materials. Magnetostriction has many practical consequences and a great deal of research has accordingly been devoted to it.

The value of saturation magnetostriction can be positive, negative or in some alloys zero. The value of λ depends on the extend of magnetization and hence on the applied field. Figure 2.11 shows how λ typically vary with H for a substance with positive magnetostriction. The process of magnetization occurs by two mechanisms, domain wall motion and domain rotation; most of the magnetostrictive change in length usually occurs during domain rotation.

When technical saturation is reached at any given temperature, in the sense that the specimen has been converted into a single domain magnetized in the direction of the field, further increase in field causes forced magnetization. This causes a slow change in λ with H called forced magnetostriction. This is caused by an increase in the degree of spin order which very high fields can produce.

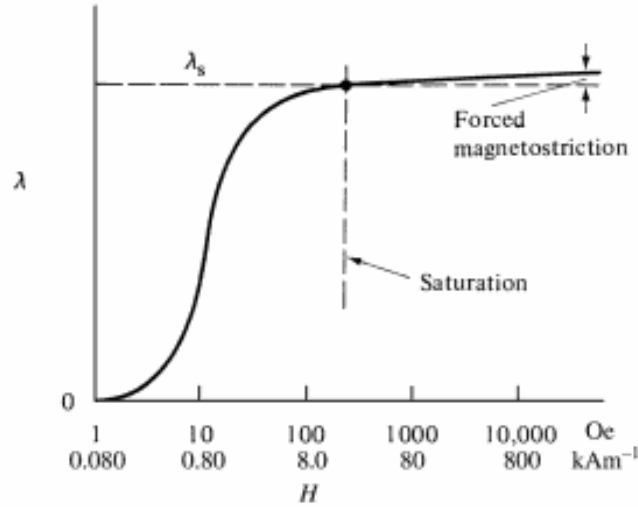


Fig. 2.11 Variation of magnetostriction λ with field H (schematic)

2.7.1 Magnetostriction in single crystal

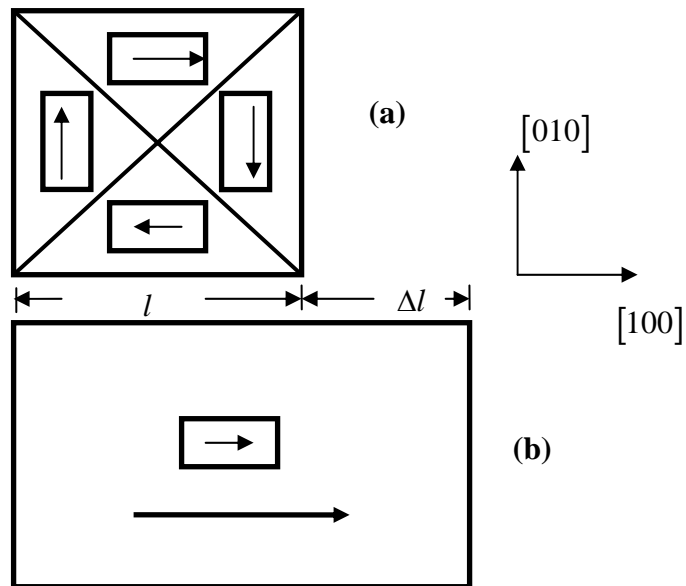


Fig. 2.12 Magnetostriction of an iron crystal in the $[100]$ direction (ref. 64)

When an iron single crystal is magnetized to saturation in a $[100]$ direction, the length of the crystal in the $[100]$ direction is found to increase. From this it can be deduced that the unit cell of ferromagnetic iron is not exactly cubic, but slightly tetragonal. The changes happening to a single crystal iron on applying a magnetic field is shown schematically in figure 2.12. If the saturated crystal is longer in the direction of its magnetization than the demagnetized crystal, then the single domain which comprises the saturated crystal must be made up of unit cells which are slightly elongated in the direction of the magnetization vector.

The same is true for each separate domain in the demagnetized state. Figure 2.12 (a) depicts this state of four sets of domains. $[100]$, $[\bar{1}00]$, $[010]$ and $[0\bar{1}0]$. The main point to notice is that these cells are all longer in the direction of the local M_s vector than they are in directions at right angles to this vector. Thus, when a region originally occupied by, say, a $[0\bar{1}0]$ domain is replaced by a $[100]$ domain by the mechanism of wall motion, that region must expand in the $[100]$ direction and contract in directions at right angles. The length of the whole crystal changes from l to $l + \Delta l$ where $\frac{\Delta l}{l} = \lambda_s$ = the saturation magnetostriction in the $[100]$ direction.

The unit cell of iron is exactly cubic only when the iron is above the Curie temperature, that is, only when it is paramagnetic and subject to no applied field. As soon as it cools below T_c , spontaneous magnetization occurs and each domain becomes spontaneously strained, so that it is then made up of unit cells which are slightly tetragonal.

There are therefore two basic kinds of magnetostriction: (1) spontaneous magnetostriction, which occurs in each domain when the specimen is cooled below the Curie point and (2) forced magnetostriction, which occurs when a saturated specimen is exposed to fields large enough to increase the magnetization of the

domain above its spontaneous value. Both kinds are due to an increase in the degree of spin order. The field induced magnetostriction in which λ changes from 0 to λ_s is caused by the conversion of a demagnetized specimen made up of domains spontaneously strained in various directions, into a saturated, single-domain specimen spontaneously strained in one direction. Figure 2.12 shows one special case of such a conversion in which the only mechanism of magnetization change is domain wall motion.

2.7.2 Magnetostriction in poly crystalline materials

The saturation magnetostriction of a polycrystalline specimen, parallel to the magnetization, is characterized by a single constant λ_p . Its value depends on the magnetostrictive properties of the individual crystals and on the way in which they are arranged, that is, on the presence or absence of preferred domain or grain orientation. If the grain orientations are completely random, the saturation magnetostriction of the polycrystal should be given by some sort of average over these orientations. When a polycrystal is saturated by an applied field, each grain tries to strain magnetostrictively, in the direction of the field, by a different amount than its neighbours, because of its different orientations.

2.7.3 Magnetostriction in amorphous alloys

The origin of magnetostriction in amorphous ferromagnetic materials has been addressed previously [71]. In macroscopically isotropic amorphous ferromagnets the average magnetic anisotropy is zero. However the material can be considered as consisting of very small structural units with strong uniaxial anisotropy and with easy axis varying randomly from site to site. These structural units exhibit spontaneous magnetostrictive strains, like small crystalline ferromagnets with corresponding orientation of easy axes [71].

For each “structural unit” characterized by a uniaxial anisotropy, the magnetostrictive strain λ_i can be calculated using equation [71]

$$\lambda_i = \frac{1}{c_{ij}} \frac{\partial E_K}{\partial \varepsilon_i} \quad 2.24$$

where ε_i is the strain in the direction i and c_{ij} is the appropriate elastic constant. The units are mechanically coupled and the macroscopic strain manifests itself by elastic strain transfer from one unit to another. The summation of these elastic strains is non-zero due to the anisotropic elastic properties of the structural units.

Analytical techniques employed for characterization

Contents

- 3.1 Swift heavy ion irradiation
- 3.2 Structural Characterisation Techniques
- 3.3 Composition
- 3.4 Magnetic measurements

Ever since optical microscopy enabled the first scientific study of phase transformation in metals and steels, the role of characterisation and importance of various characterisation tools is increasingly being felt in the realm of materials science. The advent of nanotechnology really boosted the use of various analytical tools for characterisation and tools like AFM, MFM, XPS and HRTEM thus have become house hold names. It is very essential that a proper understanding of the working principle of various tools is necessary and this chapter takes a look at some of the analytical tools employed for characterising samples at various stages.

3.1 Swift Heavy Ion Irradiation

The 15 UD Pelletron of Inter University Accelerator Centre, New Delhi, India was used for the ion beam irradiation experiment in the present study. It is a versatile, heavy ion tandem type electrostatic accelerator. In this machine, negative ions are produced and pre-accelerated to 300 KeV in Ion sources. Source of negative ions by caesium sputtering (SNICS) is a widely used source for negative ions. The negative ions are then injected into a strong electrical field inside an accelerator tank filled with sulphur hexafluoride insulating gas. At the centre of the tank there is a terminal shell,

which is maintained at a high voltage (~ 15 MV). The negative ions on traversing through the accelerating tubes from the top of the tank to the positive terminal get accelerated. On reaching the terminal, they pass through a stripper, which removes some electrons from the negative ions, thus transforming the negative ions into positive ions.

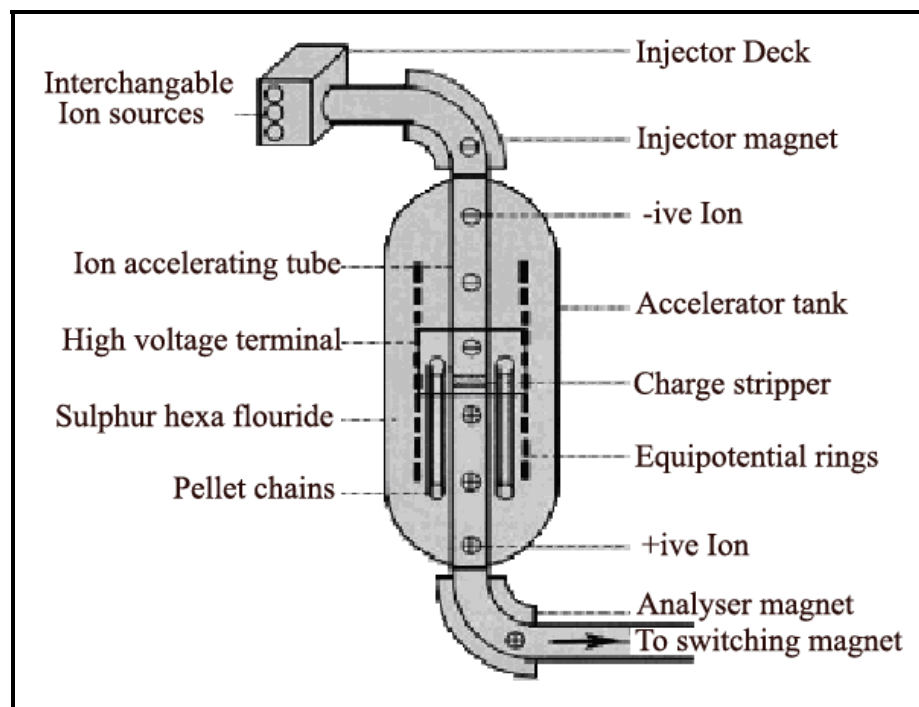


Fig.3.1 Schematic showing the principle of acceleration of ions in Pelletron

These positive ions are then repelled away from the positively charged terminal and are accelerated to ground potential to the bottom of the tank. In this manner, same terminal potential is used twice to accelerate the ions. After coming out from the tank, the ions are bent into horizontal plane by an analyzing magnet, which also selects a particular beam of ion. The switching magnet diverts the high energy ion beams into various beam lines for the different experimental areas of the beam hall.

The entire machine is computer controlled and is operated from the control room. These ions are accelerated to high vacuum chamber in the materials science beam hall, where the samples are loaded in the sample holder, made of thick block of copper. The pressure in the chamber is maintained at 1×10^{-6} Torr during the irradiation. A schematic of the Pelletron accelerator at IUAC, New Delhi is shown in figure 3.1. Further experimental details of ion beam irradiation are included in chapter 6.

3.2 Structural characterization techniques

3.2.1 Glancing angle x-ray diffraction (GAXRD)

It is sometimes very difficult to analyze thin films due to their small diffracting volumes, which result in low diffracted intensities compared to the substrate and background. This combination of low diffracted signal and high background make it very difficult to identify the phases present. So, special techniques must be employed when analyzing thin films. The most common technique for analyzing thin films as thin as 100 \AA is to use a grazing incidence angle arrangement. Glancing angle diffraction techniques are used when the information needed lies within a thin top layer of the material [72]. Figure 3.2 shows Seemann-Bohlin para-focusing geometry which is commonly used in the study of thin films.

For the Seemann-Bohlin geometry (Figure 3.2) the incident X rays impinge on a fixed specimen at a small angle, γ_G (typically 1° to 3°) and the diffracted X rays are recorded by a detector that moves along the focusing circle. This method provides good sensitivity for thin films, due to para-focusing and the large diffracting volume, which results from γ_G being small and the X-ray path length in the film being large (proportional to $1/\sin\gamma_G$). By increasing the path length of the incident X-ray beam through the film, the intensity from the film can be increased, while at the same time, the diffracted intensity from the substrate can be reduced. Overall, there is a dramatic increase in the film signal to the background ratio. Since the path length increases when the grazing incidence angle is used, the diffracting volume increases

proportionally. This is the reason for the increased signal strength. During the collection of the diffraction spectrum, only the detector rotates through the angular range, thus keeping the incident angle, the beam path length, and the irradiated area constant.

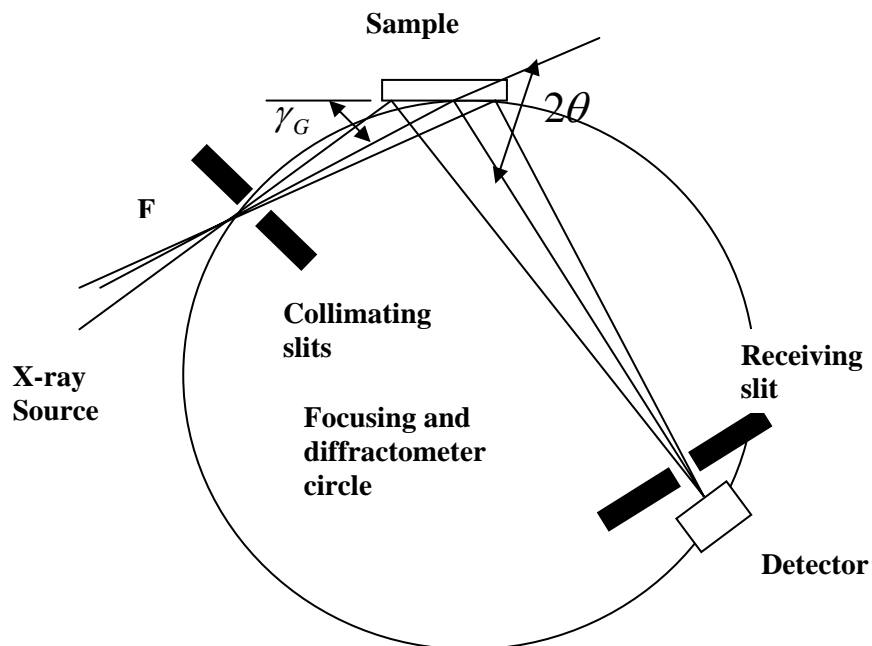


Fig.3.2 Seemann-Bohlin diffractometer. The point F is either the focal point on an x-ray tube or the focal point of a focusing monochromator.

3.2.2 Electron Microscopy

An electron microscope is employed to magnify things on a fine scale. Electron microscopes use a beam of electrons to illuminate a specimen and create a highly-magnified image. They have much greater resolving power than light microscopes. Both electron and light microscopes have resolution limitations, imposed

by the wavelength of the radiation they use. The greater resolution and magnification of the electron microscope is because the de Broglie wavelength of an electron is much smaller than that of a photon of visible light. The electron microscope uses electrostatic and electromagnetic lenses in forming the image by controlling the electron beam to focus it at a specific plane relative to the specimen. This is analogous to a light microscope using glass lenses to focus light on or through a specimen to form an image.

3.2.2.1 Scanning Electron Microscopy

Operation

In SEM, a source of electrons is focused in vacuum into a fine probe that is rastered over the surface of the specimen. The electron beam passes through scan coils and objective lens that deflect the beam horizontally and vertically so that the beam scans the surface of the sample (Figure 3.3). As the electrons penetrate the surface, a number of interactions occur that can result in the emission of electrons or photons from or through the surface. A reasonable fraction of the electrons emitted can be collected by appropriate detectors, and the output can be used to modulate the brightness of a cathode ray tube (CRT) whose x- and y- inputs are driven in synchronism with the x-y voltages rastering the electron beam. In this way an image is produced on the CRT; every point that the beam strikes on the sample is mapped directly onto a corresponding point on the screen [72]. As a result, the magnification system is simple and linear magnification is calculated by the equation:

$$M=L/l$$

where L is the raster's length of the CRT monitor and l the raster's length on the surface of the sample. SEM works on a voltage between 2 to 50 kV and its beam diameter that scans the specimen is 5nm-2 μ m. The principle images produced in SEM are of three types: secondary electron images, backscattered electron images and elemental X-ray maps. Secondary and backscattered electrons are conventionally

separated according to their energies. When the energy of the emitted electron is less than about 50 eV, it is referred to as a secondary electron and backscattered electrons are considered to be the electrons that exit the specimen with an energy greater than 50 eV [73]. Detectors of each type of electrons are placed in the microscope in proper positions to collect them.

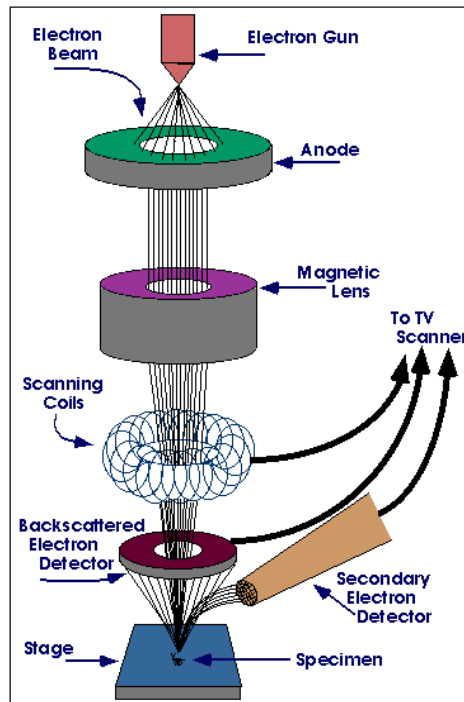


Fig.3.3 Geometry of SEM

3.2.2.2 Transmission Electron Microscopy

Transmission Electron Microscopy (TEM) is a technique where an electron beam interacts and passes through a specimen [72]. The electrons are emitted by a source and are focused and magnified by a system of magnetic lenses. The geometry of TEM is shown in figure 3.4. The electron beam is confined by the two condenser lenses which also control the brightness of the beam, passes the condenser aperture

and “hits” the sample surface. The electrons that are elastically scattered consists of the transmitted beams, which pass through the objective lens. The objective lens forms the image display and the following apertures, the objective and selected area aperture are used to choose the elastically scattered electrons that will form the image of the microscope. Finally, the beam goes to the magnifying system that consists of three lenses, the first and second intermediate lenses which control the magnification of the image and the projector lens. The formed image is shown either on a fluorescent screen or in monitor or both and is printed on a photographic film.

Operation

The operation of TEM requires an ultra high vacuum and a high voltage. TEM offers two methods of specimen observation, diffraction mode and image mode. In diffraction mode, an electron diffraction pattern is obtained on the fluorescent screen, originating from the sample area illuminated by the electron beam. The diffraction pattern is entirely equivalent to an X-ray diffraction pattern: a single crystal will produce a spot pattern on the screen, a polycrystal will produce a powder or ring pattern (assuming the illuminated area includes a sufficient quantity of crystallites), and a glassy or amorphous material will produce a series of diffuse halos. The image mode produces an image of the illuminated sample area. The image can contain contrast brought about by several mechanisms: mass contrast, due to spatial separations between distinct atomic constituents; thickness contrast, due to non uniformity in sample thickness; diffraction contrast, which in the case of crystalline materials results from scattering of the incident electron wave by structural defects; and phase contrast. If the unscattered beam is selected for image formation, one obtains the Bright Field Image. Dark Field Images are attained if diffracted beams are selected by the objective aperture. Also in TEM, analysis can be done with EDS (Energy Dispersive X-ray spectroscopy), EELS (Electron Energy Loss Spectrum) and EFTEM (Energy Filtered Transmission Electron Microscopy) data.

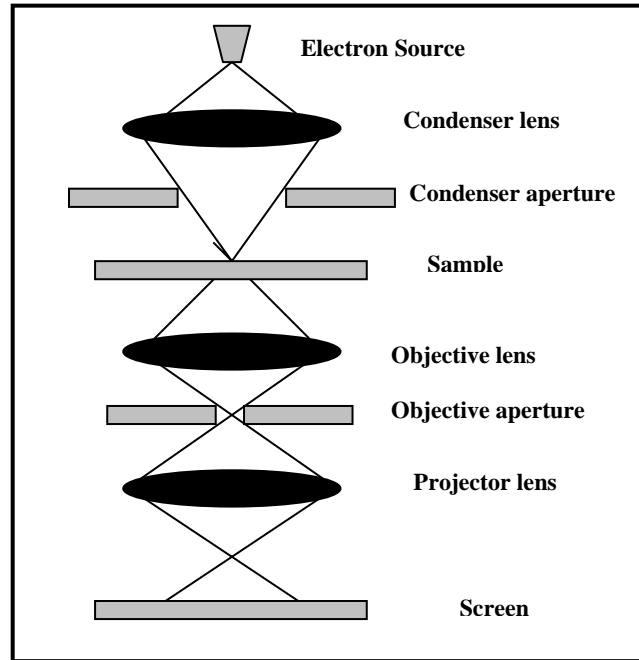


Fig.3.4 Transmission electron microscope with all of its components

3.2.3 Atomic Force Microscopy

The Atomic Force Microscope was developed to overcome a basic drawback of the STM (scanning tunneling microscope) - that it can only image conducting or semi conducting surfaces. The AFM, however, has the advantage of imaging almost any type of surface, including polymers, ceramics, composites, glass, and biological samples. Binnig, Quate, and Gerber invented the Atomic Force Microscope in 1985 [74]. Their original AFM consisted of a diamond tip attached to a strip of gold foil. The diamond tip contacted the surface directly, with the interatomic van der Waals forces providing the interaction mechanism. Detection of the cantilever's vertical movement was done using a second tip - an STM placed above the cantilever.

AFM probe deflection

Today, most AFM s use a laser beam deflection system, introduced by Meyer and Amer, where a laser is reflected from the back of the reflective AFM lever and onto a position-sensitive detector (figure 3.5). AFM tips and cantilevers are micro fabricated from Si or Si₃N₄. Typical tip radius is from a few to 10s of nm [77].

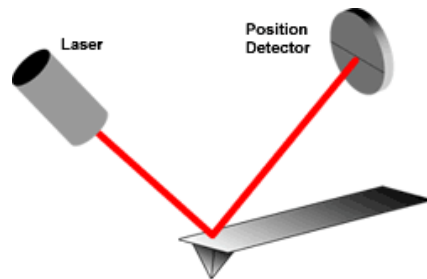


Fig.3.5 Beam deflection system, using a laser and photo detector to measure the beam position.

Measuring forces

Because the atomic force microscope relies on the forces between the tip and sample, knowing these forces is important for proper imaging. The force is not measured directly, but calculated by measuring the deflection of the lever, and knowing the stiffness of the cantilever. Hook's law gives $F = -kz$, where F is the force, k is the stiffness of the lever, and z is the distance the lever is bent. Figure 3.6 depicts the force–distance curve which shows the different forces that an AFM tip can experience from a sample.

AFM Modes of Operation

Because of AFM's versatility, it has been applied to a large number of research topics. The Atomic Force Microscope has also gone through many modifications for specific application requirements.

Contact-mode

The first and foremost mode of operation, contact mode is widely used. As the tip is raster-scanned across the surface, it is deflected as it moves over the surface corrugation. In constant force mode, the tip is constantly adjusted to maintain a constant deflection, and therefore constant height above the surface. It is this adjustment that is displayed as data. However, the ability to track the surface in this manner is limited by the feedback circuit. Sometimes the tip is allowed to scan without this adjustment, and one measures only the deflection. This is useful for small, high-speed atomic resolution scans, and is known as variable-deflection mode.

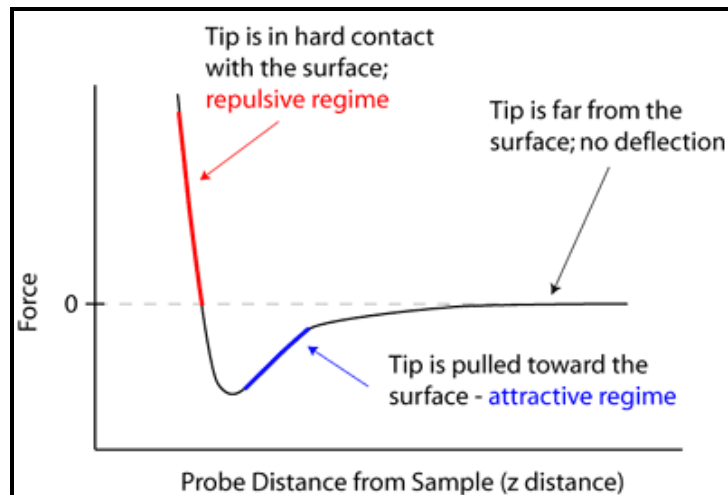


Fig.3.6 Force-distance curve

Because the tip is in hard contact with the surface, the stiffness of the lever needs to be less than the effective spring constant holding atoms together, which is on the order of 1 - 10 nN/nm. Most contact mode levers have a spring constant of $< 1\text{N/m}$.

Non-contact Mode

Noncontact mode belongs to a family of AC modes, which refers to the use of an oscillating cantilever. A stiff cantilever is oscillated in the attractive regime, meaning that the tip is quite close to the sample, but not touching it (hence, “noncontact”). The

forces between the tip and sample are quite low, on the order of pN (10^{-12} N). The detection scheme is based on measuring changes in the resonant frequency or amplitude of the cantilever.

Dynamic Force / Intermittent-contact / “tapping mode” AFM

Commonly referred to as “tapping mode” it is also referred to as intermittent-contact or the more general term Dynamic Force Mode (DFM).

A stiff cantilever is oscillated closer to the sample than in noncontact mode. Part of the oscillation extends into the repulsive regime, so the tip intermittently touches or “taps” the surface. Very stiff cantilevers are typically used, as tips can get “stuck” in the water contamination layer.

The advantage of tapping the surface is improved lateral resolution on soft samples. Lateral forces such as drag, common in contact mode, are virtually eliminated.

AFM Instrumentation

Figure 3.7 shows a schematic of the atomic force microscope. The important components are:

(Z) Coarse Z motion translator- This translator moves the AFM head towards the surface so that the force sensor can measure the force between the probe and sample. The motion of the translator is usually about 10 mm.

(T) Coarse X-Y translation stage - The XY translation stage is used to place the section of the sample that is being imaged by the AFM directly under the probe.

(X-P) X and Y piezoelectric transducer - With the X and Y piezoelectric transducer the (Y-P) probe is moved over the surface in a raster motion when an AFM image is measured.

(FS) Force Sensor - The force sensor measures the force between the probe and the sample by monitoring the deflection of a cantilever.

(ZP) Z piezoelectric Ceramic - Moves the force sensor in the vertical direction to the surface as the probe is scanned with the X and Y piezoelectric transducers.

(FCU) Feedback control unit - The feedback control unit receives the signal from the light lever force sensor and outputs the voltage that drives the Z piezoelectric ceramic. This voltage refers to the voltage that is required to maintain a constant deflection of the cantilever while scanning.

(SG) X-Y signal generator - The motion of the probe in the X-Y plane is controlled by the X-Y signal generator. A raster motion is used when an image is measured.

(CPU) Computer - The computer is used for setting the scanning parameters such as scan size, scan speed, feedback control response and visualizing images captured with the microscope.

(F) Frame - A solid frame supports the entire AFM microscope. The frame must be very rigid so that it does not allow vibrations between the tip and the surface.

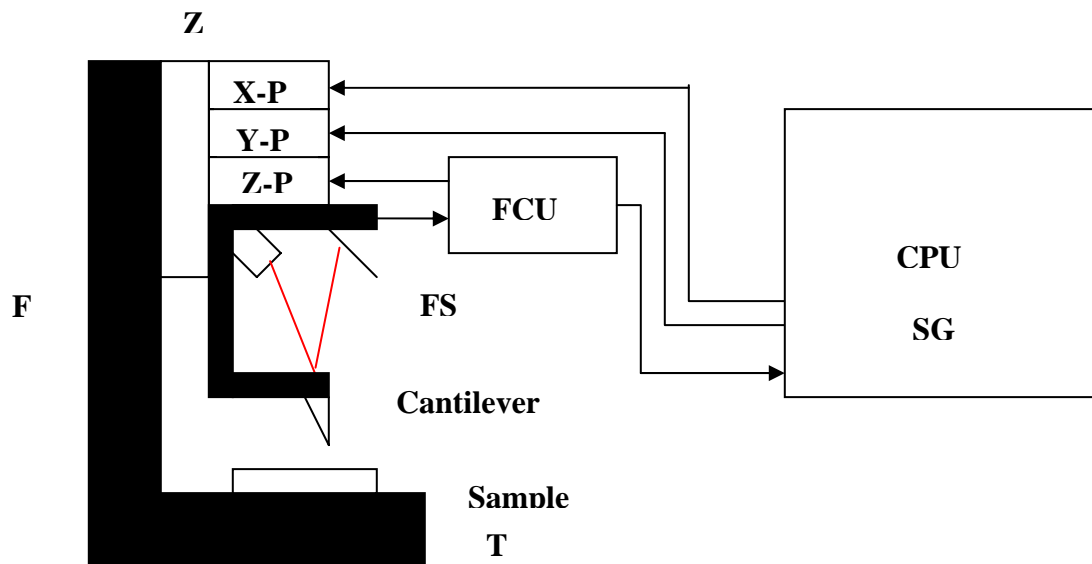


Fig.3.7 Schematic of components and subsystems of an atomic force microscope system

Resolution in an Atomic Force Microscope

Traditional microscopes have only one measure of resolution; the resolution in the plane of an image. An atomic force microscope has two measures of resolution; the plane of the measurement and in the direction perpendicular to the surface [75].

In Plane Resolution: The in-plane resolution depends on the geometry of the probe that is used for scanning. In general, the sharper the probe the higher will be the resolution of the AFM image.

Vertical Resolution: The vertical resolution in an AFM is established by relative vibrations of the probe above the surface. Sources for vibrations are acoustic noise, floor vibrations, and thermal vibrations. Getting the maximum vertical resolution requires minimizing the vibrations of the instrument.

3.2.4 Magnetic Force Microscopy (MFM)

Magnetic force microscopy detects the force (or force derivative) acting on a small magnetic probe in the stray field close to the specimen [81]. The technique can give a resolution below 20 nm with comparable low effort in sample preparation. It does not need ultra clean sample surfaces and ultra high vacuum. Also magnetic fields can be applied to the specimen during measurements.

MFM consists of a cantilever which is suspended on one side. On the free end a small volume of magnetic material, the tip is mounted. When a magnetic surface is brought close to this tip they will interact by the magnetic stray field. Magnetic force microscopy is a non-contact technique and during scanning, the sample is kept at a distance of several nanometers from the tip. The interaction between tip and sample can be measured by a detector which is placed on the back side of the cantilever. When the sample is moved with respect to the tip a one dimensional array of interaction data is put into computer and stored there. The direction of this motion is called the fast scan direction. A number of parallel scan lines will form a two-

dimensional array of data in the computer. The direction of the offset between these lines is called the slow scan direction. A computer assigns grey-or colour values to different strengths of interaction forming a microscopic image of interaction on the sample surface.

In a MFM two basic detection modes can be applied which are sensitive to two different types of interaction. The static (or DC) mode detects the magnetic force acting on the tip whereas the dynamic (or AC) mode measures the force derivative.

Static mode

According to Hooke's law the displacement Δz of the cantilever is proportional to the force that it exerts on the tip.

$$F = -c\Delta z \text{ (N)} \tag{3.1}$$

The proportionality constant c is called the cantilever constant. In this mode the cantilever is used to translate the force acting on the tip to a displacement which can be measured by the detector. The detector signal and thus the magnetic image will be a direct measure of the force acting on the cantilever.

Dynamic mode

In the dynamic mode the cantilever is oscillated at or close to its resonance frequency. The cantilever can be treated as a harmonic oscillator having the resonance frequency f which is given by

$$f = \frac{1}{2\pi} \sqrt{\frac{c_{eff}}{m}} \text{ (Hz)} \tag{3.2}$$

with 'm' the effective mass of tip and cantilever. The effective cantilever constant ' c_{eff} ' consists of two contributions

$$c_{eff} = c - \frac{\partial F}{\partial z} \text{ (N/m)}, \text{ where 'c' is the cantilever constant.} \tag{3.3}$$

In the close proximity of the sample, the forces acting on the magnetic tip change when the distance between the tip and sample is changed. This can be described by a force derivative $\frac{\partial F}{\partial z}$. This force derivative on the tip acts on the cantilever just like an additional cantilever constant. Note that in case of a large cantilever oscillation amplitude the force derivative will not be constant over one period, resulting in a non-harmonic oscillation. For low amplitudes, however a constant $\frac{\partial F}{\partial z}$ can be assumed so that the problem can still be treated as a harmonic oscillator:

$$f = \frac{1}{2\pi} \sqrt{\frac{c - \frac{\partial F}{\partial z}}{m}} \text{ (Hz)} \quad 3.4$$

From this it can be shown that a force derivative $\frac{\partial F}{\partial z}$ changes the cantilever

resonant frequency to $f = f_0 \sqrt{1 - \frac{\frac{\partial F}{\partial z}}{c}}$ (Hz) 3.5

with f_0 the free resonance frequency of the cantilever in the case of no tip-sample interaction.

The cantilever is oscillated directly at its resonance frequency f using a feedback amplifier with amplitude control. The change in resonance frequency can be directly detected by FM demodulation techniques.

During the MFM measurements, there are two forces acting on the tip; magnetic and Van der Waals forces. Hence, in MFM, the signal contains both information of surface topography (called ‘Topo signal’) and surface magnetic property (called ‘MFM signal’) generated by Van der Waals and magnetic forces, respectively. The dominating force depends on the distance between the tip and the sample surface, because the inter-atomic magnetic force persists for greater tip-to-sample separations than the van der Waals force. These van der Waals forces vary according to the tip-sample distance and therefore are used to measure the surface

topography. If the tip is close to the surface, in the region where standard Non-Contact AFM is operated, the image will be predominantly topographic. As one increase the separation between the tip and the sample, magnetic effects become apparent. Collecting a series of images at different tip heights is one way to separate magnetic from topographic effects.

The key to successful MFM imaging lies in separating the magnetic signal from the entire signal. In MFM, this is done by ‘Two Pass’ technique. In this MFM mode, sample is scanned twice to separate the signal. In the first scan, the tip scans the surface as in True Non-Contact AFM to obtain the topography of the sample. In the second scan, the tip-sample distance is increased and the biased tip is scanned along the topography line obtained from the first scan. The tip is only affected by the magnetic force and MFM image is obtained as a result.

The topographical line maintains constant tip sample distance, which equals the line of the constant van der Waals force. So, when the tip follows the topography line in the second scan of ‘MFM mode’, the van der Waals forces acting on the tip are kept constant. Thus, the only change in force affecting the signal is the change of the magnetic force. So, from the second scan, the MFM image, free of topography signal, can be obtained.

3.2.5 Scanning Tunneling Microscopy

The scanning tunneling microscope (STM) was invented by Binnig and Rohrer and implemented by Binnig, Rohrer, Gerber, and Weibel. Figure 3.8 shows its essential elements.

A probe tip, usually made of W or Pt–Ir alloy, is attached to a piezodrive, which consists of three mutually perpendicular piezoelectric transducers: x piezo, y piezo, and z piezo. Upon applying a voltage, a piezoelectric transducer expands or contracts. By applying a sawtooth voltage on the x piezo and a voltage ramp on the y piezo, the tip scans on the xy plane. Using the coarse positioner and the z piezo, the

tip and the sample are brought to within a fraction of a nanometer each other. The electron wave functions in the tip overlap electron wave functions in the sample surface. A finite tunnelling conductance is generated [76].

By applying a bias voltage between the tip and the sample, a tunneling current is generated. The most widely used convention of the polarity of bias voltage is that the tip is virtually grounded. The bias voltage V is the sample voltage. If $V > 0$, the electrons are tunneling from the occupied states of the tip into the empty states of the sample. If $V < 0$, the electrons are tunneling from the occupied states of the sample into the empty states of the tip. The tunneling current is converted to a voltage by the current amplifier, which is then compared with a reference value. The difference is amplified to drive the z piezo.

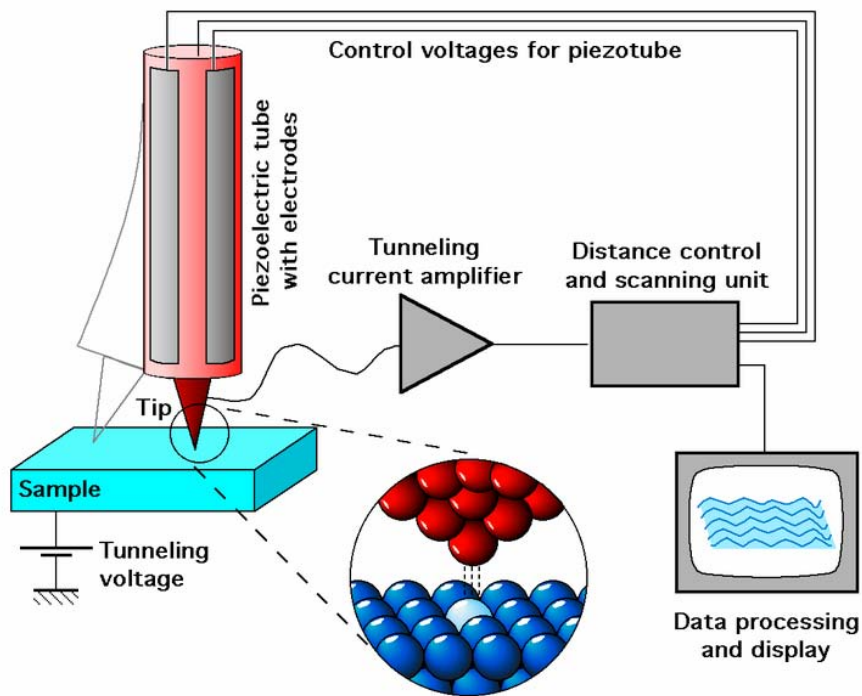


Fig.3.8 Schematic of a STM instrument

The phase of the amplifier is chosen to provide a negative feedback: if the absolute value of the tunneling current is larger than the reference value, then the voltage applied to the z piezo tends to withdraw the tip from the sample surface, and vice versa. Therefore, an equilibrium z position is established. As the tip scans over the xy plane, a two-dimensional array of equilibrium z positions, representing a contour plot of the equal tunneling-current surface, is obtained, displayed, and stored in the computer memory. The topography of the surface is displayed on a computer screen, typically as a gray-scale image. Usually, the bright spots represent high z values (protrusions), and the dark spots represent low z values (depressions). The z values corresponding to the gray levels are indicated by a scale bar. To achieve atomic resolution, vibration isolation is essential. This is achieved by making the STM unit as rigid as possible, and by reducing the influence of environmental vibration to the STM unit [77]

Modes of Operation

Constant Current Mode

By using a feedback loop the tip is vertically adjusted in such a way that the current always stays constant. As the current is proportional to the local density of states, the tip follows a contour of a constant density of states during scanning. A kind of a topographic image of the surface is generated by recording the vertical position of the tip.

Constant Height Mode

In this mode the vertical position of the tip is not changed, equivalent to a slow or disabled feedback. The current as a function of lateral position represents the surface image. This mode is only appropriate for atomically flat surfaces as otherwise a tip crash would be inevitable. One of its advantages is that it can be used at high

scanning frequencies (up to 10 kHz). In comparison, the scanning frequency in the constant current mode is about 1 image per second or even per several minutes

3.3 Composition

3.3.1 Energy dispersive x-ray spectroscopy

Photons of X-radiation with wavelength and energy characteristic of the elements in the specimen are emitted under electron bombardment in all forms of electron microscope. The spectrum of radiation can thus be used for elemental identification, using forms of x-ray spectroscopy based on either wavelength or energy (known as wavelength dispersive or energy dispersive x-ray spectroscopy) [73].

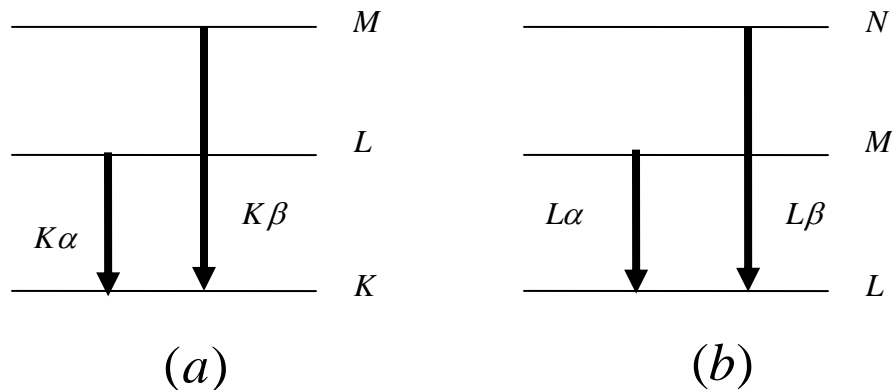


Fig.3.9 Schematic of electron transitions responsible for the production of (a) $K\alpha$, $K\beta$ (b) $L\alpha$ and $L\beta$ x-rays

An inelastic collision between a K shell electron and a primary electron with energy greater than the binding energy of the K shell electron can result in the ejection of core electron from the atom. The resulting vacancy in the K shell can be filled by an electron from one of the higher energy shells, L, M, etc. The excess energy of this electron, that is the difference between the energy states in the two shells, is irradiated during the transition as a x-ray photon. Thus the energy of the K x-radiation equals

EL-EK if the transition is between L, K shells and EM-EK if it is between M, K shells. The former is designated as $K\alpha$ radiation and later as $K\beta$. A similar situation exists with respect to electrons in the L shell. The energy of the L x-radiation equals EM-EL if the transition is between M, L shells and EN-EL if it is between N, L shells. The former is designated as $L\alpha$ radiation and later as $L\beta$. Figure 3.9 shows a schematic of the electron transitions responsible for the production of $K\alpha$, $K\beta$, $L\alpha$ and $L\beta$ x-rays. Every atom species has, therefore, a characteristic x-ray emission spectrum which can be excited by supplying energy equal to or in excess of the appropriate binding energy, by electron bombardment. The characteristic line spectrum forms the 'fingerprint' of the different atomic species. Since the actual energy levels depend on the atomic number of the elements, it follows, therefore, that the elements present in a specimen can be identified by analysis of the emission spectrum. The characteristic lines are superimposed on a background continuum (Bremsstrahlung continuum).

The technique uses a semiconductor detector to classify x-radiation according to energy. The EDS x-ray detector measures the relative abundance of emitted x-rays versus their energy. The detector is a single crystal disc of lithium-drifted silicon [Si(Li)] or high purity germanium [HPGe] having 3-5 mm thickness and with an active area between 10 and 30 mm². When an incident x-ray strikes the detector, it creates a charge pulse that is proportional to the energy of the x-ray. The charge pulse is converted to a voltage pulse (which remains proportional to the x-ray energy) by a charge-sensitive preamplifier. The signal is then sent to a multichannel analyzer where the pulses are sorted by voltage. The analyzer may have 1000 channels each 10, 20, 40 or 80 eV wide, so that the total energy range covered by the analysis would be 10, 20, 40 or 80 keV, respectively. Thus ED spectrometer is able to analyze a whole spectrum simultaneously. The spectrum of x-ray energy versus counts is evaluated to determine the elemental composition of the sampled volume.

Analytical Information

Qualitative Analysis - The sample x-ray energy values from the EDS spectrum are compared with known characteristic x-ray energy values to determine the presence of an element in the sample. Elements with atomic numbers ranging from that of beryllium to uranium can be detected. The minimum detection limits vary from approximately 0.1 to a few atom percent, depending on the element and the sample matrix.

Quantitative Analysis - Quantitative results can be obtained from the relative x-ray counts at the characteristic energy levels for the sample constituents. Semi-quantitative results are readily available without standards by using mathematical corrections based on the analysis parameters and the sample composition. The accuracy of standard less analysis depends on the sample composition. Greater accuracy is obtained using known standards with similar structure and composition to that of the unknown sample.

Elemental Mapping - Characteristic x-ray intensity is measured relative to lateral position on the sample. Variations in x-ray intensity at any characteristic energy value indicate the relative concentration for the applicable element across the surface. One or more maps are recorded simultaneously using image brightness intensity as a function of the local relative concentration of the element(s) present. About 1 μm lateral resolution is possible.

Line Profile Analysis - The SEM electron beam is scanned along a pre-selected line across the sample while x-rays are detected for discrete positions along the line. Analysis of the x-ray energy spectrum at each position provides plots of the relative elemental concentration for each element versus position along the line.

3.3.2 X-Ray Photoelectron Spectroscopy

The detection and energy analysis of photoelectrons produced by radiation whose energy exceeds their binding energies is the subject of an extensively used technique known as photoelectron (PE) spectroscopy. This technique can be conveniently divided into two broad areas, the first employing ultraviolet radiation, hence called ultraviolet photoelectron spectroscopy (UPS) and the second using X-rays, termed X-ray photoelectron spectroscopy (XPS).

Figure 3.10 (a&b) shows a schematic of the process involved in the emission of a photo – or auger electron. XPS involves the removal of a single core electron, while AES is a two electron process subsequent to the removal of the core electron. Auger electrons are produced in XPS along with photoelectrons.

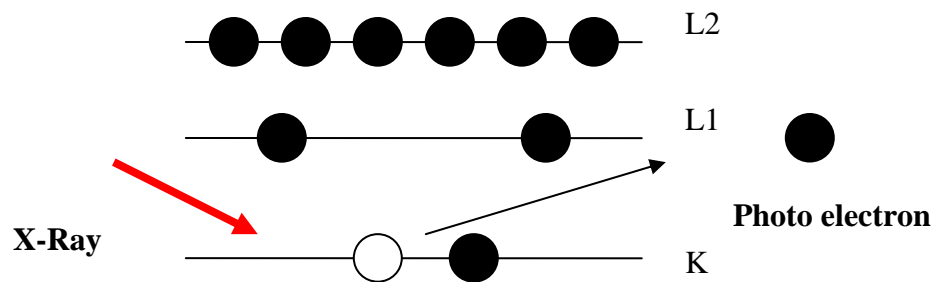


Fig.3.10 (a) Process involved in photoelectron emission

In XPS the sample is irradiated with x-rays of known energy, $h\nu$ and electrons of binding energy (BE) E_b are ejected, where $E_b < h\nu$. These electrons have a kinetic energy (KE) E_k which can be measured in the spectrometer, and is given by [78, 79]

$$E_k = h\nu - E_b - \Phi_{sp} \quad 3.6$$

where Φ_{sp} is the spectrometer work function, and is the combination of sample work function, Φ_s , and the work function induced by the analyzer. Since we can compensate for the work function term electronically, it can be eliminated, leaving

$$E_k = h\nu - E_b \quad 3.7$$

or

$$E_b = h\nu - E_k \quad 3.8$$

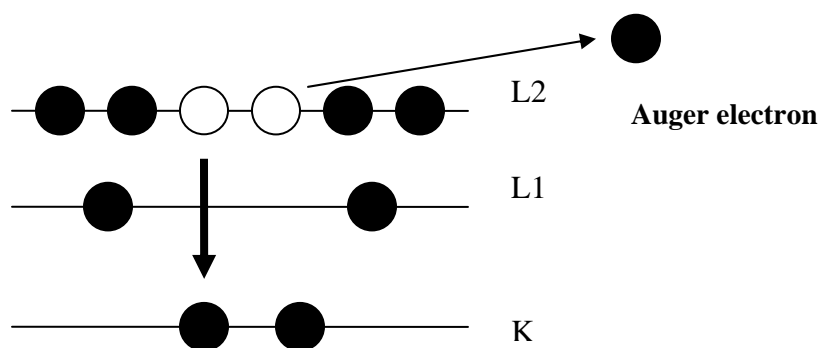


Fig.3.10 (b) Process involved in Auger electron emission

Thus by measuring the KE of the photoelectrons we can determine the BE of the electrons. An XP spectrum is generated by plotting the measured photoelectron intensity as a function of BE. The resulting series of lines are superimposed on a background caused by the Bremsstrahlung radiation inherent in non-monochromatic X-ray sources. The BEs of these lines is characteristic for each element, and is a direct representation of the atomic orbital energies.

The exact binding energy of an electron depends not only upon the level from which photoemission is occurring, but also upon the formal oxidation state of the atom and the local chemical and physical environment. Changes in either of the above will give rise to small shifts in the peak positions in the spectrum - so-called chemical

shifts. Such shifts are readily observable and interpretable in XP spectra because the technique is of high intrinsic resolution (as core levels are discrete and generally of a well-defined energy) and is a one electron process (thus simplifying the interpretation). Atoms of a higher positive oxidation state exhibit a higher binding energy due to the extra coulombic interaction between the photo-emitted electron and the ion core. This ability to discriminate between different oxidation states and chemical environments is one of the major strengths of the XPS technique.

XPS is a surface sensitive technique and the surface sensitivity of XPS is due to the low inelastic mean-free path, λ_m of the electrons within the sample. For XPS, the main region of interest relates to electron energies from 100-1200 eV, which gives rise to a λ_m value of 0.5 to 2 nm. However the actual escape depth λ of the photoelectrons depends on the direction in which they are traveling with in the sample, such that

$$\lambda = \lambda_m \cos \theta \quad 3.9$$

where θ is the angle of emission to the surface normal. Thus electrons emitted perpendicular to the surface ($\theta=0^\circ$) will arise from the maximum escape depth, whereas electrons emitted nearly parallel to the surface ($\theta=90^\circ$) will be purely from the outermost surface layers.

The basic requirements for a photoemission experiment (XPS or UPS) are:

1. A source of fixed-energy radiation (an x-ray source for XPS or, typically, a He discharge lamp for UPS).
2. An electron energy analyzer (which can disperse the emitted electrons according to their kinetic energy, and thereby measure the flux of emitted electrons of a particular energy).
3. A high vacuum environment (to enable the emitted photoelectrons to be analyzed without interference from gas phase collisions).

Such a system is illustrated schematically in figure 3.11

There are many different designs of electron energy analyzer but the preferred option for photoemission experiments is a concentric hemispherical analyzer (CHA) which uses an electric field between two hemispherical surfaces to disperse the electrons according to their kinetic energy.

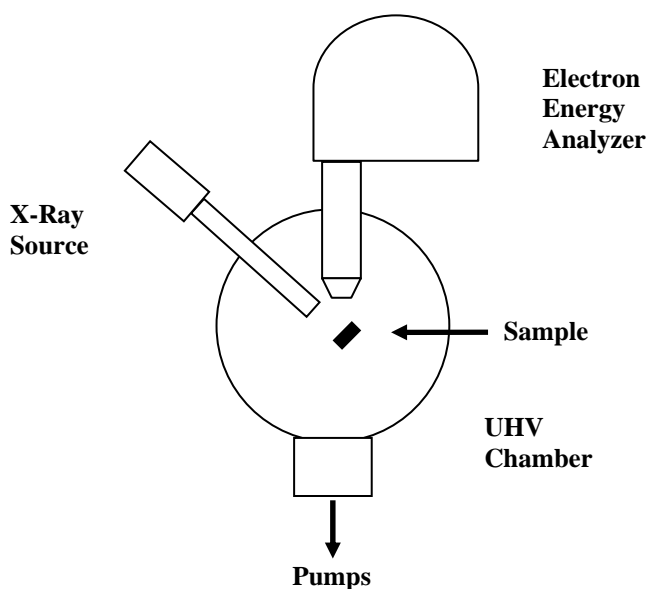


Fig.3.11 Schematic of XPS system

3.4 Magnetic measurements

3.4.1 Vibrating sample magnetometer

The magnetic characterization of the samples was carried out using a Vibrating Sample Magnetometer (VSM), model: DMS 1660. The main parts of a VSM and the simplified block diagram are given in figure 3.12 and 3.13. Saturation magnetization (M_s), Retentivity (M_r) and Coercivity (H_c) were evaluated from the hysteresis loops.

The magnetic samples are kept in the sample holder, which is centered in the region between the pole pieces of an electromagnet. A slender vertical sample rod connects the sample holder with a transducer assembly located above the magnet. The transducer converts a sinusoidal ac drive signal into a sinusoidal vertical vibration of the sample rod and the sample thus made to undergo sinusoidal motion in a uniform magnetic field. Coils mounted on the pole pieces of the magnet pick up the signal resulting from the sample motion. This ac signal at the vibrating frequency is proportional to the magnitude of the moment induced in the sample. Thus, the pick up coil output accurately gives an account of the moment level of the sample.

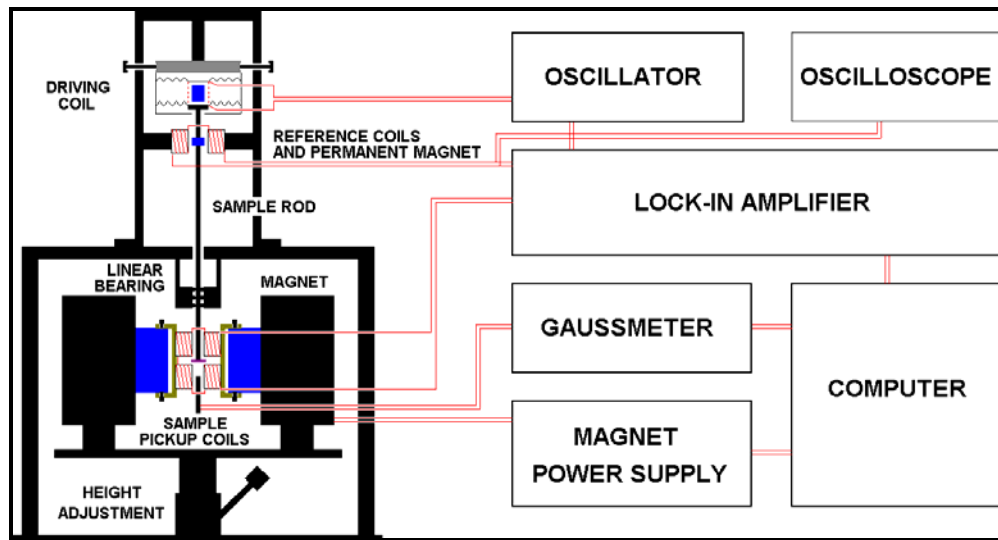


Fig.3.12 Main Parts of VSM

Vibrating sample magnetometry is employed to determine the magnetization of the samples synthesized. When a magnetic material is placed in a uniform magnetic field, a dipole moment is induced which is proportional to the susceptibility of the

sample and the applied field. If the sample is vibrated periodically then it can induce an electrical signal in a pickup coil. The position of the pickup coil is adjusted in such a way as to give the maximum induction without much noise. The induced signal in the pickup coil will be proportional to the magnetic moment produced in the sample and the vibrating frequency of the sample [80].

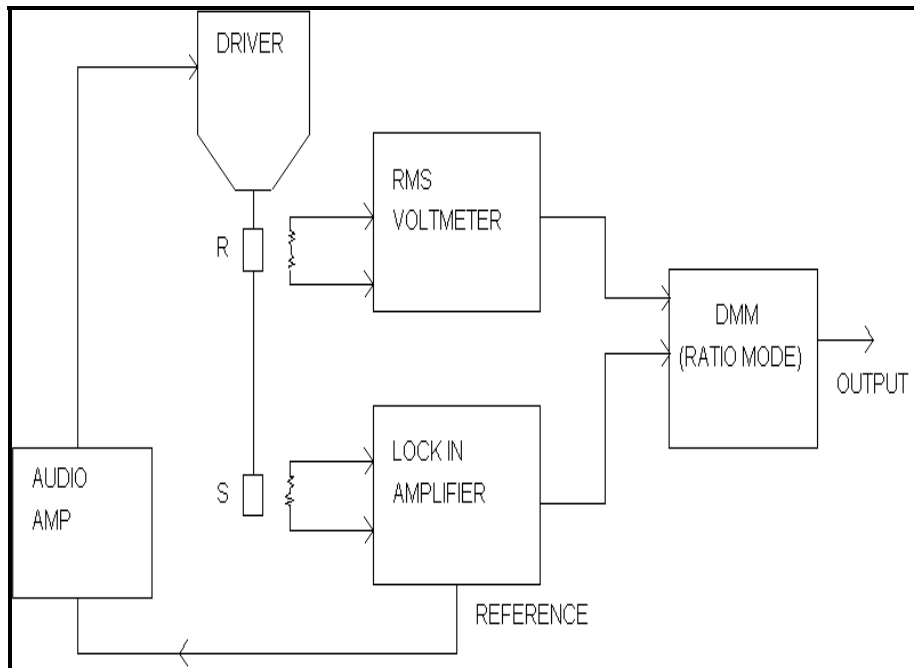


Fig.3.13 Block Diagram of VSM.

This is the basic principle used in the design of a VSM to measure the magnetic properties. The material under study is loaded in the sample holder, and it is placed at the centre region of the pole pieces of a laboratory electromagnet. A slender vertical sample rod connects the sample holder with a transducer assembly located above the magnet, which in turn supports the transducer assembly by means of sturdy adjustable support rods.

A transducer is used to convert the electrical oscillations into mechanical vibrations. An electronic oscillator circuit produces a constant frequency and it is fed to the transducer to vibrate the sample rod. The vibrating sample in the uniform magnetic field induces a signal in the pickup coils mounted to it. The strength of the ac signal at the vibrating frequency is proportional to the magnetic moment induced in the sample. However, vibration amplitude and frequency also will have some contributions to the induced emf. A servomechanism is used to stabilize the amplitude and frequency of the drive so that the output accurately tracks the moment level without degradation due to variation in the amplitude and frequency of the oscillator.

This servo technique uses a vibrating capacitor located beneath the transducer to generate an ac control signal that varies solely with the vibration amplitude and frequency. The signal, which is at the vibration frequency, is fed back to the oscillator where it is compared with the drive signal so as to maintain constant drive output. It is also phase adjusted and routed to the signal demodulator where it functions as the reference drive signal. The signal developed in the pick up coils is then buffered, amplified and applied to the demodulator. There it is synchronously demodulated with respect to the reference signal derived from the moving capacitor assembly. The resulting dc output is an analog signal, which depends only on the magnitude of the magnetic moment, and not influenced by the amplitude and frequency drift. The cryogenic setup attached to the sample assembly can be used to study the magnetization of samples at low temperatures.

3.4.2 Ferromagnetic Resonance

FMR is a method to measure magnetic properties by detecting the precessional motion of the magnetization in a ferromagnetic sample.

It is thus related to the electron paramagnetic resonance technique. From a macroscopic point of view, the applied static magnetic field H_0 causes the total

magnetic moment to precess around the direction of the local field H_{eff} , before relaxation processes damp this precession and the magnetization aligns with H_{eff} (figure 3.14).

If the sample is irradiated with a transverse rf field (microwaves of typically 1–35 GHz), and if the rf frequency coincides with the precessional frequency, the resonance condition is fulfilled and the microwave power is absorbed by the sample.

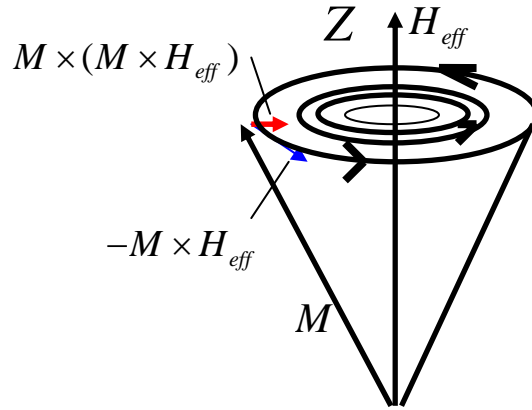


Fig.3.14 Precessional motion of magnetic moment in an applied magnetic field

The motion of the magnetization is described by the Landau-Lifshitz-Gilbert equation [40]

$$\frac{\partial \mathbf{M}}{\partial t} = -\gamma (\mathbf{M} \times \mathbf{H}_{\text{eff}}) + \frac{G}{\gamma M_s^2} \left[\mathbf{M} \times \frac{\partial \mathbf{M}}{\partial t} \right] \quad 3.10$$

The first part corresponds to the precession. The second part introduces a viscous damping (Gilbert damping constant G). The effective magnetic field H_{eff} includes the applied DC field, the rf microwave magnetic field component, the demagnetizing field (shape anisotropy) and the magnetocrystalline anisotropy field. γ is the gyromagnetic ratio $\gamma = g\mu_B/\hbar$.

Microscopically, the H field creates a Zeeman splitting of the energy levels, and the microwave excites magnetic dipole transitions between these split levels (figure 3.15). Since it is difficult to vary the microwave frequency over larger ranges, the DC magnetic field H_0 is varied instead [82].

Usually the absorption derivative is measured. The resonance signal resembles a Lorentzian line shape (figure 3.16). The resonance field position H_{res} depends on the angles, anisotropy parameters, g -factor, and magnetization of the sample.

The linewidth ΔH is directly connected to the relaxation processes. In ultra thin films, Gilbert damping is commonly used to describe the relaxation. But several other possible relaxation paths are also known, e.g. two-magnon scattering, spin-pumping effect, etc., which can contribute to the linewidth. The anisotropy constants can be easily deduced from angle dependent measurements of single crystalline samples. For magnetic multilayers, also the interlayer exchange coupling constant can be determined by FMR in absolute units.

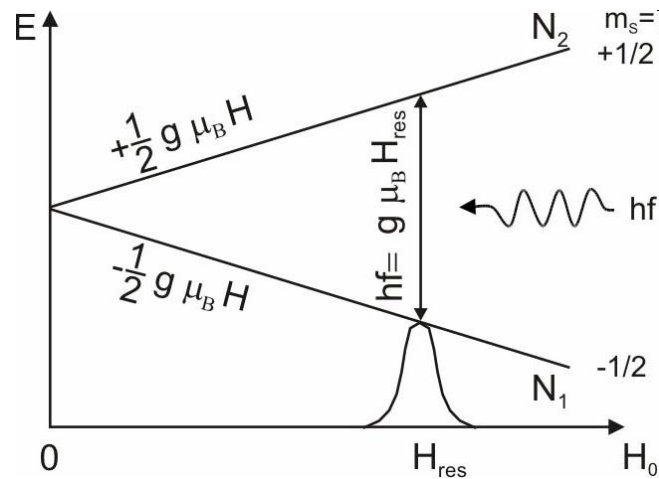


Fig.3.15 Zeeman splitting of energy levels by a magnetic field

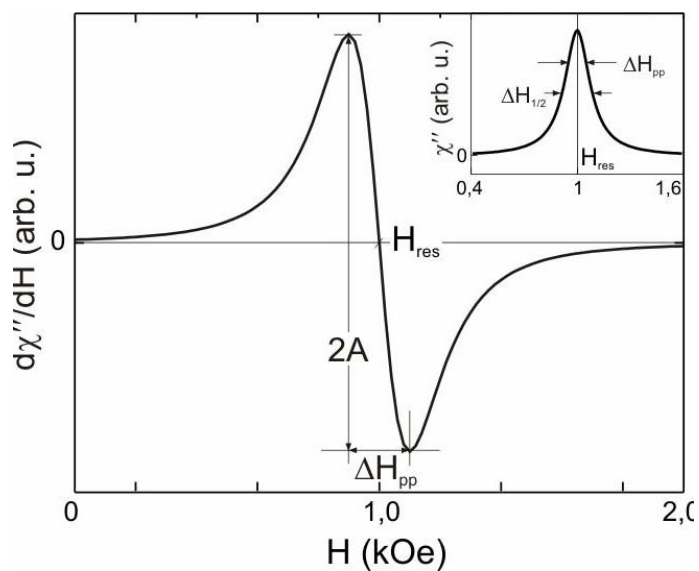


Fig.3.16 A typical FMR spectra

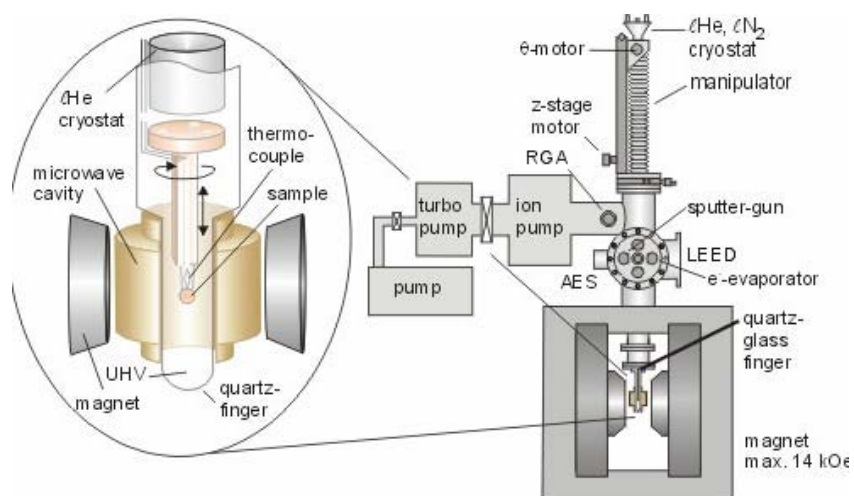


Fig.3.17 Schematic of the experimental set up for FMR measurements

Figure 3.17 shows a schematic of the experimental setup for FMR measurements. The sample is kept under UHV inside a quartz glass finger connected to the UHV chamber. It fits into the microwave cavity. The microwave components and the electromagnet coils are outside the vacuum and therefore conveniently accessible or removable.

Fabrication and characterisation of amorphous and nanocrystalline Fe-Ni thin films

4.1	Introduction
4.2	Experiment
4.3	Results and Discussions
4.4	Conclusion

4.1. Introduction

Nanocrystalline magnetic materials is increasingly becoming a hot topic of research because of their potential in finding end uses in fields such as power electronics, sensors, actuators, soft under layer for perpendicular recording media and as the core material for write elements in the modern recording heads [39,83,84]. The microstructure of these materials consists of nano sized ferromagnetic materials embedded in an amorphous matrix. The matrix phase must also be ferromagnetic for facilitating the exchange coupling between the nanoparticles. As a result of this coupling, they often exhibit vanishing magnetocrystalline anisotropy. Since the soft magnetic properties are strongly related to the crystalline anisotropy, the exchange interaction in nanocrystalline magnetic materials results in an improvement of its soft magnetic properties.

The averaging out of magnetocrystalline anisotropy in these materials can be explained in terms of random anisotropy model proposed by Alben *et al* [66]. The effective anisotropy energy density in this model is given by the square root of the mean square fluctuation of the anisotropy energy in the exchange coupled volume. Although the random anisotropy model was propounded to explain the magnetic

softness in amorphous materials, Herzer showed that the model is also applicable to nanocrystalline systems [67].

For an assembly of ferromagnetically coupled grains of size D ($D < L_{ex}$) with randomly oriented magnetocrystalline anisotropies K_1 , the average anisotropy $\langle K \rangle$ is

$$\text{given by } \langle K \rangle = K_1 \left(\frac{D}{\left(\frac{A}{K_1}\right)^{1/2}} \right)^{2n/(4-n)} \quad [68] \text{ where } n \text{ denotes the dimension of the}$$

system. This means that $\langle K \rangle$ follows a $D^{2/3}$, D^2 and D^6 dependence on grain size for one-dimensional, two-dimensional and three dimensional structures, respectively. The coercivity (H_c) and permeability (μ) are related to $\langle K \rangle$ through the relation

$$H_c \propto \langle K \rangle \text{ and } \mu \propto \frac{1}{\langle K \rangle}.$$

The sensitive grain size dependence on the soft magnetic properties in these materials is related to the interplay of local magnetocrystalline anisotropy energy and the ferromagnetic exchange interaction. For large grains the magnetization can follow the local easy magnetic directions and the magnetization process is determined by the magnetocrystalline anisotropy K_1 of the crystallites. However for very small grains, the ferromagnetic exchange interaction forces the magnetic moments to align parallel to each other. Thus the effective anisotropy will be an average over several grains and will be reduced in magnitude. The dividing line between these two extremes is the ferromagnetic exchange correlation length $L_{ex} = \left(\frac{A}{K_1}\right)^{1/2}$, where A is the exchange stiffness constant and K_1 is the anisotropy constant.

Amorphous alloys which are precursors of nanocrystalline materials can be synthesized by a variety of techniques such as rapid solidification from the liquid state, mechanical alloying, plasma processing and vapour deposition [1]. Nanocrystalline

microstructure can be obtained by the controlled crystallization of the amorphous state. There are several reports in the literature pertaining to this method of preparation [85, 86, 2, 87]. Melt quenching or high energy ball milling was used for preparing the metastable states and most of the studies were carried out in ribbons or in powders. With the advent of nanocrystalline materials exhibiting excellent soft magnetic properties thin films of these materials also assume significance from an application point of view.

Vapour deposition offers a simple alternative for sputter deposition in obtaining thin films of supersaturated solid solutions and other metastable states. Amorphous magnetic thin films thus obtained presents high coercivity due to the stresses in the films. One way of improving the magnetic softness is by precipitating nanocrystals with in the amorphous matrix. Further, nanocrystallisation allows one to tailor the magnetic properties by controlling the size of the precipitates. Control of magnetic properties is highly essential in order to obtain miniaturized magnetic devices with improved performance characteristics. Since the magnetic properties are strongly dependent on the microstructure, the soft magnetic properties can be tuned by modifying the microstructure.

Metglas 2826 MB ($\text{Fe}_{40}\text{Ni}_{38}\text{Mo}_4\text{B}_{18}$) is a soft magnetic alloy that exhibits superior soft magnetic materials. Its softness after nanocrystallisation can be ascribed to its two phase nature consisting of Fe-Ni nanocrystals embedded in the remaining boron rich amorphous matrix. Additives like boron and molybdenum are incorporated in the alloy to achieve specific objectives. Boron aids in retaining the glassy characteristics while molybdenum is a known grain growth inhibitor. However, high metalliod content causes deterioration not only in their magnetic properties but also in elasticity and plasticity [61]. If B and Mo can be dispensed with in Fe-Ni based alloys like Metglas, this brings in economy and is an attractive proposition from a commercial point of view. Since Metglas is widely used for sensor applications, thin

film form of this material would be of great interest for integrating thin film sensors with today's microelectronics. This can be realized by depositing thin films of this material on suitable substrates.

Some attempts of preparation of Metglas thin films by thermal evaporation have been reported in the literature [88, 70]. Thin films of $\text{Fe}_{40}\text{Ni}_{38}\text{Mo}_4\text{B}_{18}$ were prepared by flash evaporation techniques [88]. The electron microscopy and diffraction investigations on these films showed that the films decompose in a eutectic fashion with thermal annealing. Magnetic studies were not carried out on these samples and the main focus of the work was on the structural evolution of these films with thermal annealing. An alloy film with the same composition was studied by Hysen *et al.* [70]. Thin films (thickness around 36 nm) of $\text{Fe}_{40}\text{Ni}_{38}\text{Mo}_4\text{B}_{18}$ were prepared by thermally evaporating Metglas 2826 MB ribbons. The deposited films were amorphous and were thermally annealed to obtain nanocrystalline microstructure. A lowering in crystallization temperature was observed (~ 473 K) when compared to bulk alloy system (683 K) which was attributed to the lower volume fraction of molybdenum in the thin films. The observed changes in coercivity with annealing temperature were explained using random anisotropy model extended to two dimensional systems. However in these investigations the composition of the film was not ascertained and the nature of the microstructure were not established by any experimental techniques. Such a study only will give credence in correlating the microstructure with the magnetic properties. Also, the amorphous interlayer in nanocrystalline magnetic material plays a crucial role in determining the magnetic and electronic properties. Hence employment of sophisticated techniques like transmission electron microscopy in characterizing the material has significance from an application point of view. It is in this context that a systematic investigation on a magnetic soft alloys based on Fe-Ni assumes relevance.

The main objective of the work presented in this chapter is to gain an insight into the microstructural evolution with thermal annealing in Fe-Ni based amorphous thin films and to correlate the observed magnetic properties with microstructural evolution. For this, Fe-Ni based amorphous thin films were prepared by thermal evaporation technique. Nanocrystalline microstructure was obtained by the partial crystallization of the amorphous films. Microstructure was controlled by annealing the films at different temperatures. The films were characterized using x-ray diffraction technique (XRD), transmission electron microscopy (TEM), selected area electron diffraction (SAED), Energy Dispersive x-ray Spectrometry (EDS), x-ray photoelectron spectroscopy (XPS) and vibrating sample magnetometer. Finally the grain size dependence of coercivity is explained using random anisotropy model extended to two dimensional systems.

4.2. Experiment

4.2.1 Preparation

Commercially available Metglas 2826 MB ribbon of composition $\text{Fe}_{40}\text{Ni}_{38}\text{Mo}_4\text{B}_{18}$ was employed as a source material to deposit Fe-Ni thin films on silicon, glass and NaCl substrates. The silicon and glass substrates were cleaned with acetone, ethanol and trichloroethylene and were immediately loaded into the vacuum chamber. The distance from source to the centre of 1 cm^2 substrate was 20 cm. The films were deposited by thermal evaporation using a current of 23 A at a pressure of about 1×10^{-5} mbar. The base pressure of $\sim 1 \times 10^{-5}$ m bar was achieved by a diffusion pump backed with a rotary pump. These thin films have also been heat treated at 373 K, 473 K, 573 K and 673 K to follow microstructural evolution of the as deposited films. The annealing treatment consisted of increasing the temperature of the samples at about 10 K /minute to the desired temperature, holding it for 1 hr and cooling to room temperature. The annealing was performed in a vacuum of 1×10^{-5} mbar.

4.2.2 Characterization

The thicknesses of the films were determined using scanning electron microscopy cross-sectional measurements (JOEL JSM 6390). X-ray diffraction measurements were performed using an x-ray powder diffractometer technique employing a copper target (Cu $K\alpha = 1.5418 \text{ \AA}$, Rigaku Dmax C). The scanning speed was adjusted to 2°min^{-1} with a sampling interval of 0.05. Transmission electron microscopy experiments were carried out on films coated on NaCl substrates. A Joel JEM-2200 FS electron microscope operated at 200 kV was used for this. The compositions of the films were analyzed using an energy dispersive x-ray spectrometer which was attached to the TEM column. STM studies were carried out using a Veeco-Digital Instruments multimode scanning probe microscope operated under ambient conditions. The measurements were performed using tungsten tips. The STM images were recorded in the constant current mode at a sample bias of 1.2V and a current set point of 0.4 nA. The topographical images represent the height of the tunnelling tip above the sample. The images are digitally filtered to remove the low frequency noises. X-ray photoelectron spectroscopy (XPS) measurements were carried out using an Omicron Nanotechnology Multiprobe Instrument. XPS spectra were obtained using a high resolution hemisphere analyzer EA 125 HR equipped with a detection system consisting of seven channeltrons. A monochromated Al $K\alpha$ source of energy $h\nu = 1486.6 \text{ eV}$ was used to probe the films which was attached to a molybdenum sample holder. Pressure in the XPS chamber during the measurements was $5 \times 10^{-10} \text{ mbar}$. Room temperature magnetization measurements were carried out using a vibrating sample magnetometer (DMS 1660 VSM) with an external field varying from -1 to $+1 \text{ kOe}$.

4.3 Results and discussions

4.3.1 Composition analysis

Figure 4.1 shows the energy dispersive x-ray spectrum (EDS) of the as deposited film. The composition of the films was measured from the peak intensities of Fe $K\alpha$ and Ni $K\alpha$ lines in the EDS spectrum. The atomic percentage of Fe and Ni were 55 and 45 respectively.

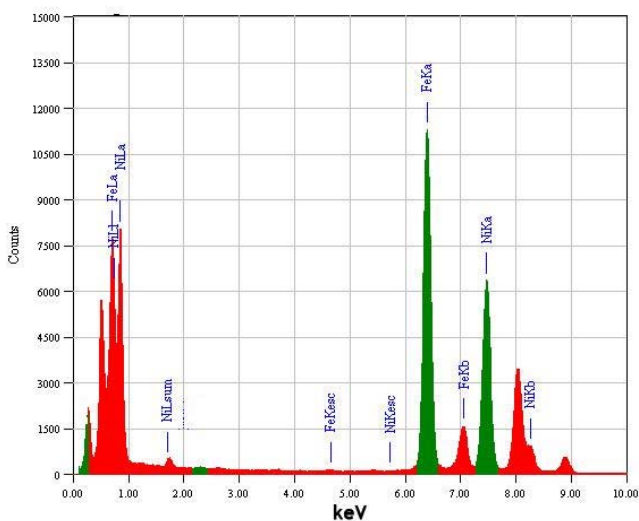


Fig.4.1 EDS profile for as deposited film

XPS survey scan was collected for as deposited film and is depicted in figure 4.2. The spectrum exhibits characteristic photoelectron lines of Fe, Ni, O and C. The C 1s peak corresponds to the unavoidable contaminant carbon on the top surface of the specimen. The O 1s spectrum consists of peak originating from oxygen in metal-oxygen bond. The survey scan also exhibited lines corresponding to the emission of Auger electrons (Ni LMM, Fe LMM and O KLL). Boron and molybdenum were not detected in the XPS survey scan. The absence of molybdenum and boron in XPS indicates that the film is deficient in boron and molybdenum. In XPS the relative

sensitivity of Fe, Mo and B compared to Ni is 0.86, 0.64 and 0.06 respectively. The low sensitivity for B is due to the small photoionization cross section for boron. However we were able to detect Mo and B in Metglas 2826 MB ribbon (the source material used for evaporation). The spectrum for B 1s and Mo 3d acquired from Metglas ribbon is shown in figure 4.3 (a) and 4.3 (b) respectively. The scan for B 1s and Mo 3d lines in thin films [figure 4.3(c) and 4.3 (d)] doesn't show these elements in thin films. Since the detection limit of XPS is in the range 0.1 to 1 atom% we attribute the absence of Mo and B peaks in the XPS to the absence of these elements in the film.

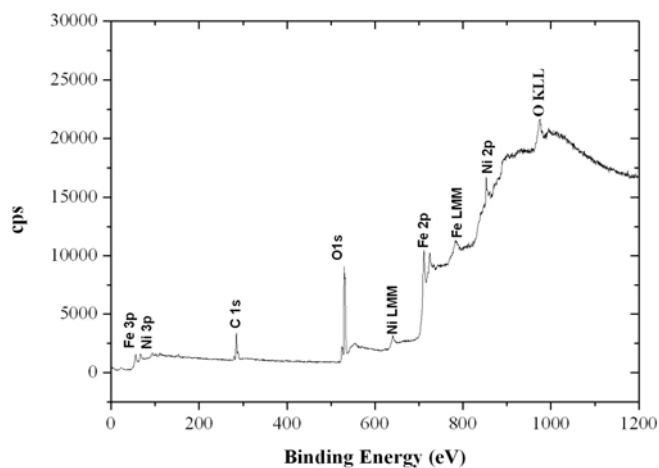


Fig. 4.2 XPS survey scan for as deposited film

The absence of molybdenum and boron in both EDS and XPS indicates that the film is deficient in boron and molybdenum. This is expected because out of the four elements Fe, Ni, Mo and B, boron and molybdenum has the highest melting point and lowest vapour pressures. So it is believed that boron and molybdenum do not evaporate off easily from the target material.

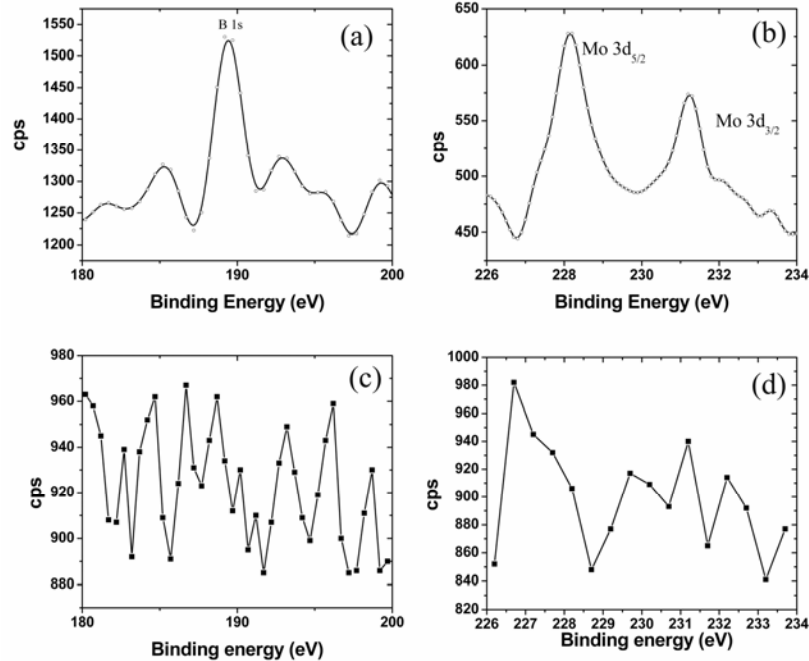


Fig. 4.3 (a) B 1s spectrum of the source material used for evaporation (Metglas 2826 MB ribbon) (b) Mo 3d of the source material used for evaporation (Metglas 2826 MB ribbon) (c) XPS scans for B 1s in thin films and (d) XPS scans for Mo 3d in thin films

4.3.2 Structural and micro structural characterization

Figures 4.4(a) show the STM image of the as-deposited film. The topography reveals an island-like structure which implies that the film grows according to the Volmer–Weber model [89]. According to this growth model the interaction between the adatoms will be greater than the interaction with the substrate. So the resultant will be a three-dimensional nucleus. The morphology of such films will exhibit island-like features. The AFM line scan in figure 4.4(b) illustrates the 3D nature of the growth. Cross sectional SEM images showed that the films were of 25 nm thickness (figure 4.5). The XRD pattern of as deposited and annealed films is depicted in figure 4.6.

The XRD pattern of the as deposited thin film does not show any sharp diffraction peaks indicating that they are amorphous. The amorphous state is stable up to a temperature of 373 K. The onset of nanocrystallization is at around 473 K. It should be noted that in Metglas 2826 MB ribbons $[\text{Fe}_{40}\text{Ni}_{38}\text{Mo}_4\text{B}_{18}]$ the crystallization temperature is at around 683 K [14, 90]. The reduced crystallization temperature in the case of thin films is due to the depletion of metalloids. The diffraction pattern of the annealed samples at 473 and 573 K shows a peak centered at 44° which can be assigned to FCC phase of Fe-Ni.

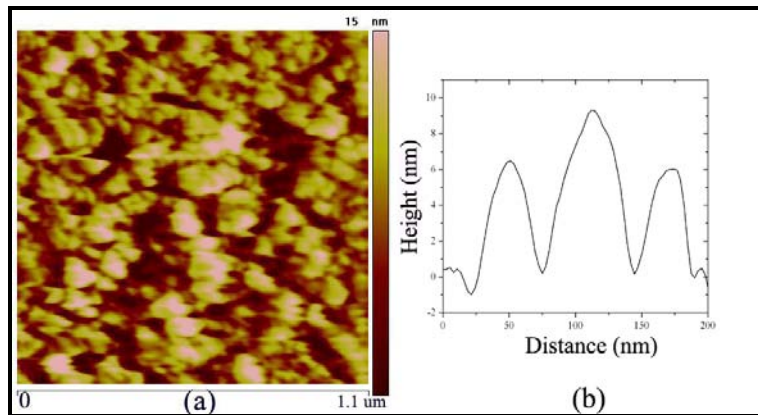


Fig. 4.4 STM image of (a) as deposited film. Figure (b) shows a line scan indicating the 3D nature of the growth.

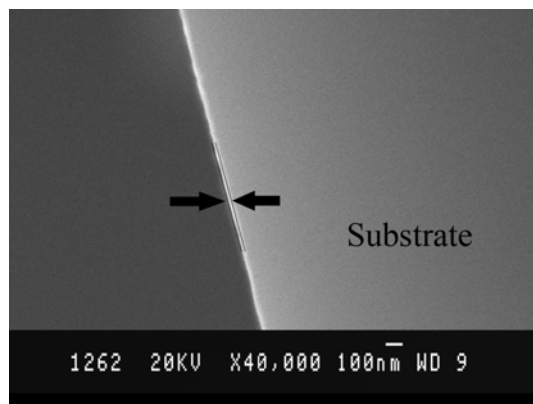


Fig. 4.5 Cross sectional SEM image showing the thickness of the film

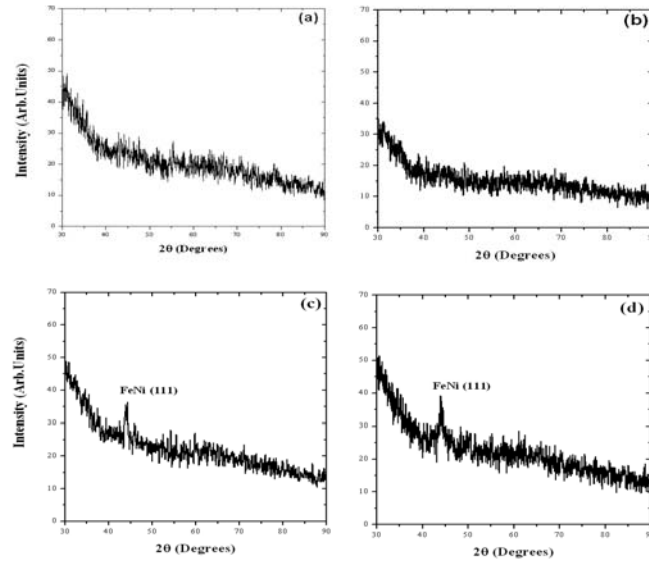


Fig. 4.6 XRD pattern of (a) as deposited film and films annealed at (b) 373 K (c) 473 K and (d) 573 K

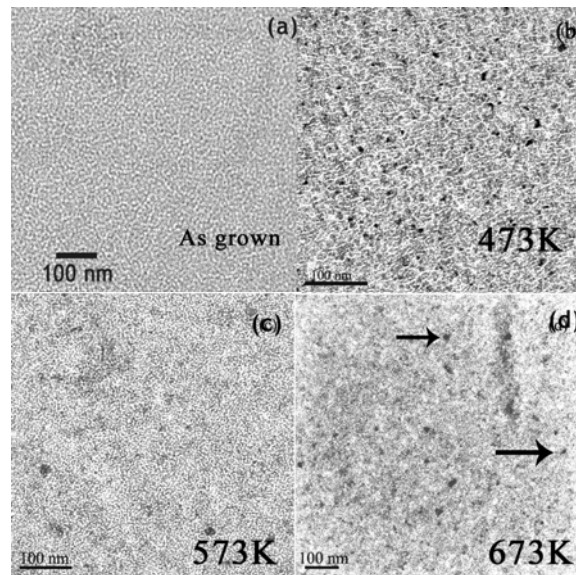


Fig. 4.7 TEM bright field image of (a) as deposited film and films annealed at (b) 473 K (c) 573 K and (d) 673 K. The arrow in (d) points to the nanocrystalline precipitates

The as deposited and annealed films were also investigated by TEM. Figure 4.7 (a) shows the bright field image of the as deposited thin films. The microstructure exhibits a contrast typical of an amorphous material.

The electron diffraction pattern (figure 4.9(a)) consists of a wide diffraction ring corresponding to an inter-planar distance $d = 2.014 \text{ \AA}$. This corresponds to an average distance (x_m) between atoms in the amorphous structure, where $x_m = 1.23d = 2.5 \text{ \AA}$. This value is in agreement with the observations of Dunlop *et al* [91] in Finemet alloys.

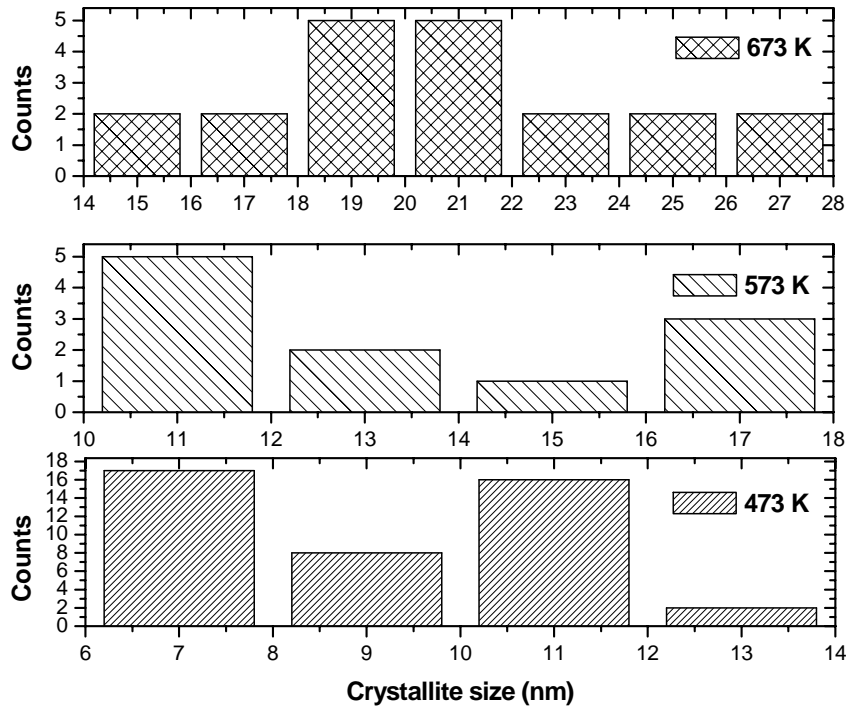


Fig.4.8 Crystallite size distribution obtained from TEM bright field image of 473 K, 573 K and 673 K annealed samples

Figure 4.7 (b), (c) and (d) shows the bright field image of the films annealed at 473 K, 573 K and 673 K respectively. The microstructure consists of fine

nanocrystallites embedded in an amorphous phase. Grain growth is observed with an increase in annealing temperature. The selected area diffraction pattern [figure 4.9(b)] confirms that these are nanocrystallites of the Fe-Ni phase which is consistent with our XRD observations. The EDS point analysis on the nanocrystals showed that they are of composition $\text{Fe}_{57}\text{Ni}_{43}$. The mean grain size (D) as estimated from the bright field image is around 10 nm, 16 nm and 20 nm for samples annealed at 473 K, 573 K and 673 K. Figure 4.8 shows that there is a distribution of nanocrystallite sizes in 473 K, 573 K and 673 K annealed samples.

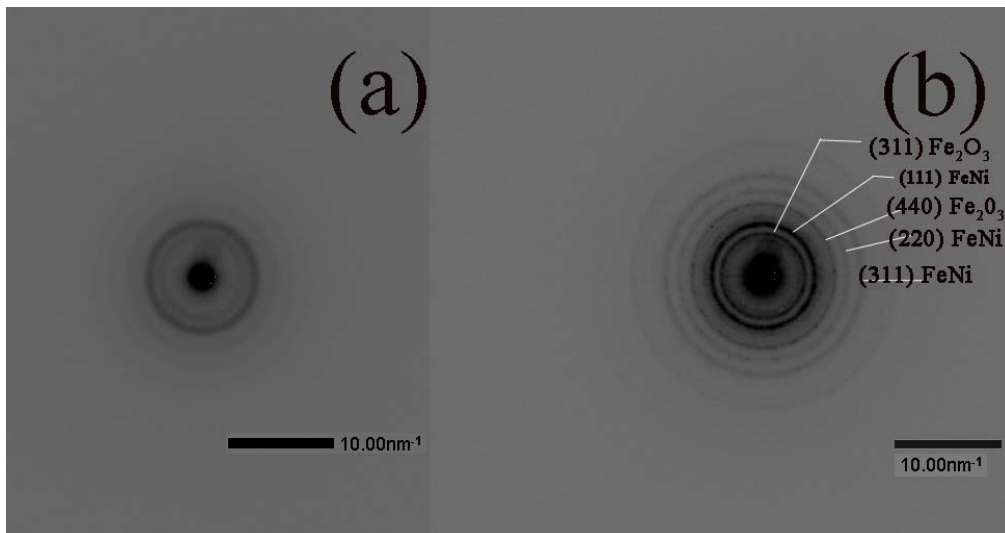


Fig. 4.9 Electron diffraction pattern of (a) as deposited film and (b) film annealed at 473 K.

There is also a ring in the selected area diffraction pattern of 473 K annealed sample which corresponds to Fe_3O_4 or Fe_2O_3 . It is not possible to differentiate between these two oxides phases by electron diffraction because of their structural

similarities (inverse spinel). However Fe 2p XPS spectrum (figure4.10) shows that the oxide formed is that of Fe_2O_3 .

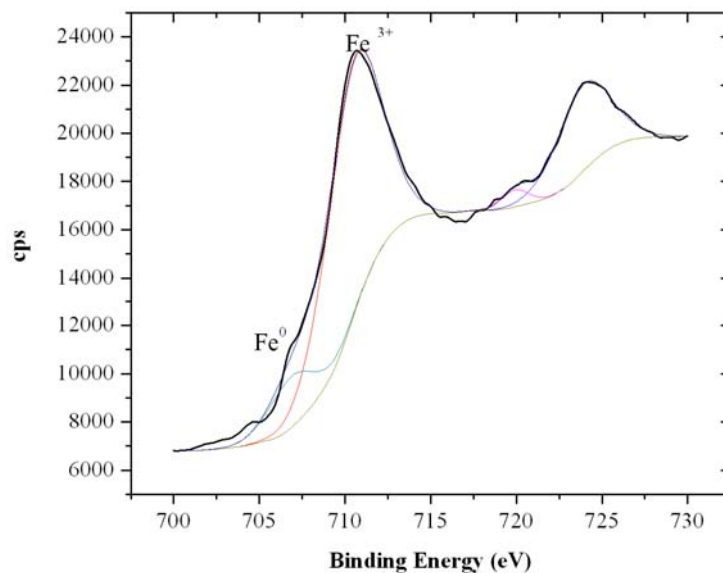


Fig. 4.10 XPS Fe 2p spectrum

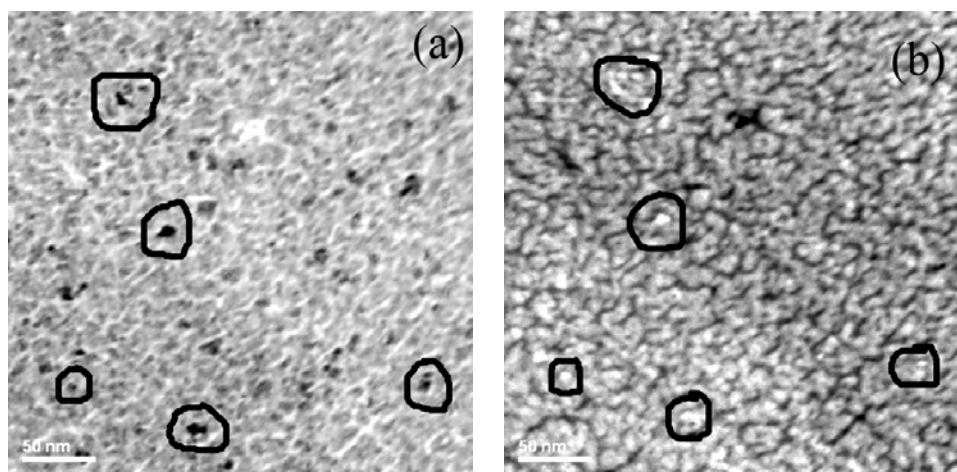


Fig. 4.11 TEM (a) bright field image and (b) dark field image for 473 K annealed sample. The circles drawn are a guide to eye to locate the position of nanocrystallites.

The Fe 2p_{3/2} peak occurs at around 710 eV which indicates the presence of Fe₂O₃ on the surface of the film. Curve fitting shows that Fe 2p peak can be resolved into two components with binding energies centered at 710 and 707 eV which corresponds to Fe³⁺ and Fe⁰ respectively [92]. The absence of oxide peaks in the XRD pattern implies that their percentage concentration is very low and is well below the detection limits of XRD. Since we were not employing any capping agents against oxidation the formation native oxide layer on the surface of the films cannot be ruled out.

The presence of nanocrystals in an amorphous matrix is further evident from the TEM dark field image shown in figure 4.11 (b). In bright field imaging we are probing the electrons which have traversed the specimen without significant change in direction. Hence we cannot distinguish the contrast changes due to thickness variation or due to the presence of crystallites. Dark field imaging is more informative because it uses deflected electrons rather than the transmitted ones for forming images. In dark field imaging one is using the electrons which have actually interacted with the specimen. The dark field image in figure 4.11(b) shows the coexistence of both amorphous and crystalline phases in 473 K annealed samples.

4.3.3 Magnetic studies

Figure 4.12 shows the hysteresis loops for the as deposited and annealed films measured in a field parallel to the film's plane. It is clear that there is a marked difference in the observed coercivity of as deposited and annealed films.

The variation of coercivity with annealing temperature is plotted and is shown in figure 4.13. It is evident from the graph that softening occurs at around 373 K before the onset of crystallization. This is because of the stress relief from the amorphous matrix. From 473 K onwards the coercivity shows a strong dependence on grain size. It is to be noted that the nanocrystallization occurs at around 473 K and TEM images shows that grain growth is facilitated at higher annealing temperatures.

The coercivity increased from 36 Oe to 107 Oe as the grain size increased from 10 to 20 nm.

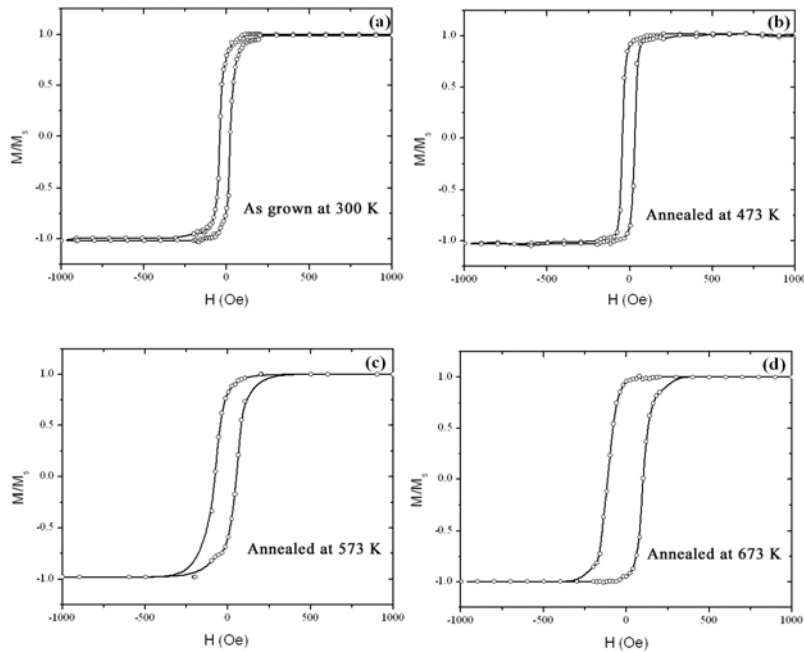


Fig. 4.12 Room temperature hysteresis loop of (a) as deposited and films annealed at (b) 473 K (c) 573 K and (d) 673 K measured in a parallel field

The coercivity in nanocrystalline ferromagnetic films can also be described by the random anisotropy model extended to two dimensional systems [ref Chapter 2].

The experimental dependence of H_c on grain size, D is shown in figure 4.14. Solid line is a linear fit to the experimental points. The slope of the curve was found to be ~ 1.5 . One can notice that there is a discrepancy in the value of calculated and theoretical slopes. It should be noted that while deriving the D^2 law a single value for the grain size D was assumed. But the size distribution chart from the electron micrographs (figure 4.8) show that there is a distribution in grain size, D . The inhomogeneity in the

grain size has a pronounced effect on the effective anisotropy [93]. This can be a reason for the discrepancy observed in the theoretical and calculated slopes.

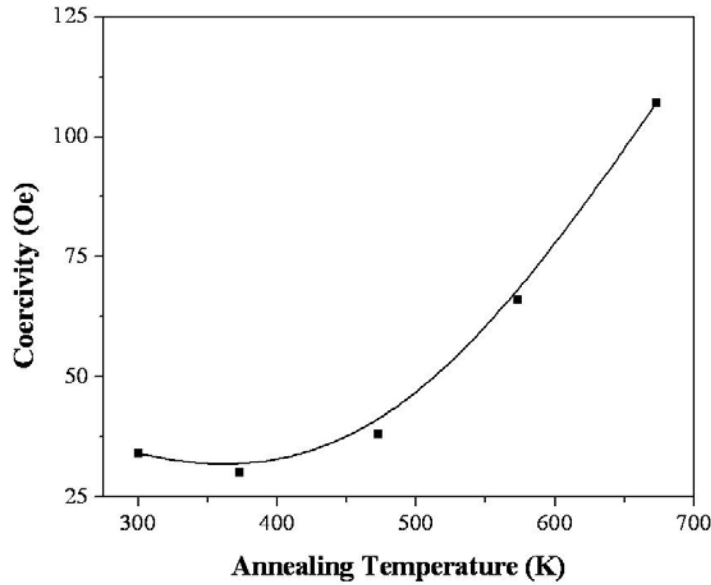


Fig.4.13 Coercivity dependence on annealing temperature. Solid line is a guide to the eye.

Local magnetic anisotropy can be evaluated using the equation $H_c = \frac{p_c K_1^2 D^2}{M_s A}$

. Substituting the values for M_s ($M_s = 861 \text{ emu/cm}^3$), A ($A=10^{-11}\text{J/m}$) and assuming $p_c=0.6$. The anisotropy constant K_1 was calculated from the slope of the H_c Vs D^2 plot. The value of K_1 was found to be 5.7 kJ/m^3 . This value is slightly greater than the reported values for bulk Fe-Ni with similar composition (1 kJ/m^3) [94]. This enhancement can be attributed to the surface anisotropy that is reported in ultra fine particles [95]. Knowing the value of K_1 and A one can determine L_{ex} using the

equation $L_{ex} = \sqrt{\frac{A}{K_1}}$. The value of L_{ex} is found to be 40 nm. The film thickness in the

present investigation is well below the exchange length which supports the applicability of two dimensional random anisotropy model to the films in the current investigation.

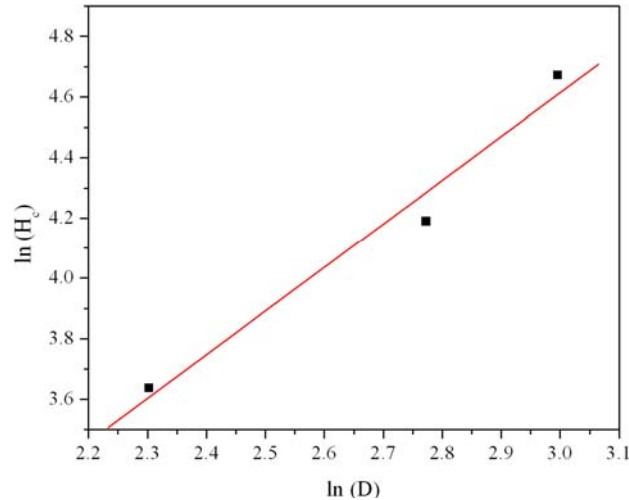


Fig.4.14 Dependence of H_c on grain size D

4.4 Conclusion

Vapour deposited thin films of Fe-Ni were thermally annealed to obtain nanocrystalline microstructure. Electron microscopy investigations showed that the microstructure consisted of Fe-Ni nanocrystals embedded in an amorphous matrix. The size of the nanocrystals was controlled by annealing the films at different temperatures. Coercivity had a strong dependence on grain size. The observed grain size dependence of coercivity is attributed to the random magnetic anisotropy characteristics of the system and was explained using random anisotropy model extended to two dimensional systems.

Swift heavy ion induced surface modification for tailoring coercivity in Fe-Ni based amorphous thin films.

Contents	5.1	Introduction
	5.2	Experiment
	5.3	Results
	5.4	Discussions
	5.5	Conclusion

5.1. Introduction

Fe-Ni based amorphous thin films are increasingly becoming an interesting topic of research because of their potential applications in soft magnetic devices [1, 39, 84, 96, and 97]. Metallic alloys with disordered structure are produced from the liquid state during cooling and are also known as metallic glasses [98]. There are several methods in vogue for the preparation of amorphous alloys. Here, physical vapour deposition, high energy ball milling, ion beam irradiation and melt spinning needs special mention.

Control of magnetic properties is highly essential in order to obtain miniaturized magnetic devices with improved performance characteristics. The magnetic properties are strongly dependent on the microstructure and hence the magnetic properties of these materials can be tailored by modifying the microstructure. For example, the variation in the sputtering rate during the sputter deposition of magnetic thin films can result in the modification of coercivity [29]. Coercivity of magnetic thin films can also be tailored by depositing films on seed layers [99]. Recently, the modification of the magnetic properties in Fe based nanocrystalline

alloys by thermal annealing was reported [69]. In thin magnetic films, the surface roughness plays an important role in the magnetization reversal mechanisms and this in turn determines the coercivity of the material [100,101].

Ion irradiation has been considered as an alternative tool to modify the surface properties. An energetic ion that penetrates a solid loses energy mainly via two independent process: (a) electronic excitation and ionization [electronic energy loss, $(dE/dx)_e$] which is dominant in the high energy regime (greater than 1MeV/ nucleon) and (b) elastic collisions with nuclei of the target atoms [nuclear energy loss $(dE/dx)_n$] which are dominant in the low energy regime. The ion energy loss per unit path length depends strongly on the ion velocity. Swift heavy ion passes through a solid with a velocity comparable to the Bohr velocity of electrons and loses its energy while traversing through the material. The rapid energy transfer during the inelastic collision results in a transient excitation of the medium that finally culminates in the production of point defects, clusters, columnar defects and phase transformation along the path of the heavy ion beam [102-106].

The mechanism by which the energy can be deposited is through two different process, namely thermal spike and coulomb explosion [107-109]. In the former the ion beam excites the electronic system at the local site and electrons transfer this energy to phonons via electron-phonon coupling resulting in an increase in the local temperature. In the latter, ions create ionization zones during their passage through the material. The ionization zone with positive charges may explode under electrostatic force and induces strain in the material.

Metallic glasses were thought of resistant to irradiation induced modifications. This hypothesis was based on the fact that irradiation induced disorder is easily absorbed in the heavily disordered structure of an amorphous system. But in the 1980s it was observed that metallic glasses when subjected to irradiation produced damages [110,111]. Glassy alloys like $\text{Pd}_{80}\text{Si}_{20}$ and $\text{Cu}_{50}\text{Zr}_{50}$ when irradiated with high energy ions

were found to be undergoing dimensional changes perpendicular to the ion beam, whereas the sample shrunk in dimension parallel to the ion beam. Measurements using x-ray diffraction and electrical resistivity revealed that the structural modifications of radiation deformed samples were small in comparison to the dimensional changes. This discovery was rather surprising because of the following: (1) At that time there was a supposition that a metallic glass, as a completely disordered metal, would be more radiation resistant than any crystalline metal (2) In crystalline materials any radiation induced anisotropic change in sample dimensions are due to a natural crystallographic anisotropy. In sharp contrast, dimensional changes in glassy $\text{Pd}_{80}\text{Si}_{20}$ and $\text{Cu}_{50}\text{Zr}_{50}$ was introduced by the beam itself and (3) the number of atoms, which occupied new positions in order to accommodate the dimensional changes exceeded by one or two orders of magnitude than the number of atoms which are displaced via the nuclear energy loss.

Later on, the anisotropic growths in metallic glasses were experimentally evidenced by many researchers [112,113]. Audouard *et al* [112] observed that the irradiation of $\text{Fe}_{85}\text{B}_{15}$ ribbons with 850 MeV ^{207}Pb and 350 MeV ^{238}U results in the formation of hillocks and hollows. The formation of hillocks was attributed to the damage created in individual ion tracks and hollows were linked to the occurrence of anisotropic growth phenomenon. Later on, FeBSiC and $\text{Fe}_{55}\text{Zr}_{45}$ ribbons were subjected to investigate the role of linear rate of electronic excitation $(dE/dx)_e$ and temperature on defect creation and growth process [113]. Contrary to the earlier belief that the effect of swift heavy ion on metallic glasses was limited to the anisotropic growth, Dunlop *et al.* in 2003 showed that partial crystallization of an amorphous alloy (FINEMET) is also possible by a high level of electronic energy deposition [91]. This crystallization phenomenon was interpreted in terms of an irradiation induced pressure wave which allowed a rearrangement of the local atomic structure of the alloy. These findings lead to the conviction that electronic excitation could induce

structural modification in metallic glasses and also macroscopic variations in the dimensions of irradiated metallic glass should induce modifications of the topography of the sample surface.

$\text{Fe}_{40}\text{Ni}_{38}\text{Mo}_8\text{B}_{14}$ (Metglas 2826) is an amorphous alloy which shows superior soft magnetic properties [114-115]. Since Metglas is widely used for sensor applications, thin film form of this material would be of great interest for integrating thin film sensors with today's microelectronics. This can be realized by depositing thin films of this material on suitable substrates.

The surface evolution of a thin film under swift heavy ion irradiation will be an outcome of a competition between sputtering induced surface roughening process and the material transport induced smoothing process. The final film morphology thus depends on the dominant process. Mayr and Averback [116] observed that the smoothing of a rough amorphous film occurred during ion beam irradiation and radiation induced viscous flow was identified as the dominant surface relaxation mechanism. Mieskes *et al.* [117] observed an increase in surface roughness in Au, Zr, Ti when irradiated with 230 MeV Au ions. The increased surface roughness was attributed to the sputtering induced by Swift heavy ions. The magnetic properties of thin films are strongly dependent on the surface/interface roughness and SHI is an effective tool in modifying the surface of a material.

Considering the prospects of fabricating thin films based on Fe-Ni from metallic glass ribbons by simple vacuum evaporation techniques and the fact that amorphous alloys are not resistant to irradiation induced damages, a detailed investigation in probing the surface modification of amorphous thin films of Fe-Ni is worthwhile. It was thought that swift heavy ions would modify the surface structure of these alloys and will eventually lead to modification of magnetic properties. Further, the studies relating to SHI induced surface modifications and the intrinsic magnetic properties of thin films are rather scarce or seldom reported. The impingement of ions

with different fluence on the alloy is bound to produce systematic microstructural changes and if these changes produce a pattern, this could effectively be used for tailoring the coercivity of these materials. The *in situ* method of tailoring coercivity using swift heavy ion is novel and is an ingenious tool in creating surface modification which will eventually lead to changes in the bulk property. AFM is a promising tool for such a study on ion bombarded films where a minimum sample preparation is required. It offers a good lateral resolution too. The present study was carried out in order to investigate the effect of swift heavy ion irradiation on the magnetic and surface properties of Fe-Ni based amorphous alloys. Attempts are made to correlate the observed magnetic properties with surface evolution.

5.2. Experiment

Fe-Ni films with a thickness of 35 nm were deposited using a composite target having the composition $\text{Fe}_{40}\text{Ni}_{38}\text{Mo}_8\text{B}_{14}$ (Metglas 2826) onto ultrasonically cleaned glass substrates employing thermal evaporation techniques. During deposition the base pressure in the chamber was maintained at 1×10^{-5} mbar with the help of a diffusion pump backed with a rotary pump. These samples were irradiated by 108 MeV Ag^{8+} ions at room temperature with different fluences ranging from 1×10^{12} to 3×10^{13} ions cm^{-2} using a 15 UD Pelletron accelerator at Inter University Accelerator Centre, New Delhi, India. A uniform irradiation over an area of 1×1 cm^2 was achieved using a raster scanner. With the computer code SRIM, the nuclear stopping power $(dE/dx)_n$, electronic stopping power $(dE/dx)_e$ and the residual range R_p were calculated as a function of ion energy. The value of $(dE/dx)_e$ is close to 28 keV/nm and are greater than the corresponding $(dE/dx)_n$ values (1.6 eV/nm) [figure 5.1]. The projected range of 108 MeV silver ions ($R_p = 7 \mu\text{m}$) is higher than the film thickness so that the ion beam traverses through the material thickness and finally gets deposited in the substrate. The films were subjected to x-ray diffraction (XRD) at grazing incidence

using Bruker AXS diffractometer. Cu K α of wavelength 1.54 Å was employed for X-ray measurements at a glancing angle of 2°. The scanning speed was adjusted to 1°/min.

The surface morphology of pristine as well as irradiated films was examined using an atomic force microscope (Digital Instruments Nanoscope II). Room temperature magnetization measurements were carried out using a vibrating sample magnetometer (DMS 1660 VSM) with an external field varying from -3 to +3 kOe.

5.3. Results

5.3.1 Glancing angle XRD studies

Glancing angle XRD studies showed that both pristine and irradiated samples are amorphous in nature. The GXRD pattern of pristine and irradiated films is depicted in figure 5.2. The amorphous nature of these films is clearly evident from these studies.

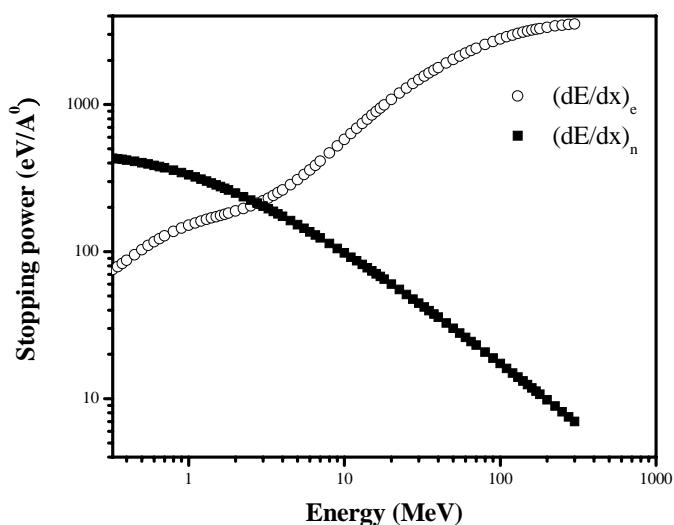


Fig. 5.1 SRIM simulation for calculating electronic and nuclear energy loss for 108 MeV Ag⁸⁺ ions in Fe-Ni target

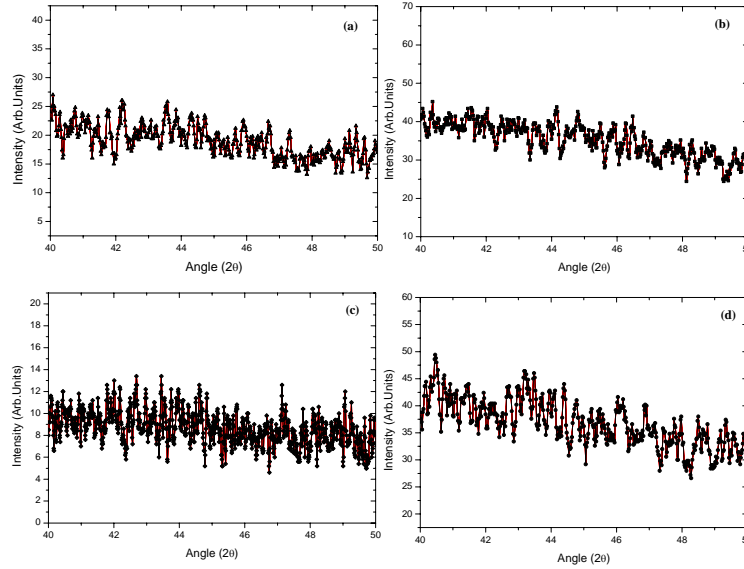


Fig. 5.2 GAXRD pattern for (a) pristine and irradiated films with fluence (b) 1×10^{12} (c) 3×10^{12} (d) 3×10^{13} ions/cm²

5.3.2 Atomic force microscopy studies

The surface topography of pristine and irradiated Fe-Ni thin films is shown in figure 5.3. It can be observed that there is a marked difference in the surface morphology of pristine and irradiated films. The best known parameter in characterizing the morphology of a surface is the rms roughness (ρ_{rms}), which expresses the variation of the height function $h(r,t)$ over a two-dimensional substrate with linear size L .

$$\rho_{rms} = \sqrt{\frac{1}{L^2} \sum (h(r,t) - \bar{h}(t))^2}$$
 where r is the position vector and the mean height is given by $\bar{h}(t) = \frac{1}{L^2} \sum h(r,t)$. The rms roughness was calculated for both pristine as

well as irradiated films and is depicted in figure 5.4 as a function of fluence. It is clear that roughness increases with increase in ion fluence.

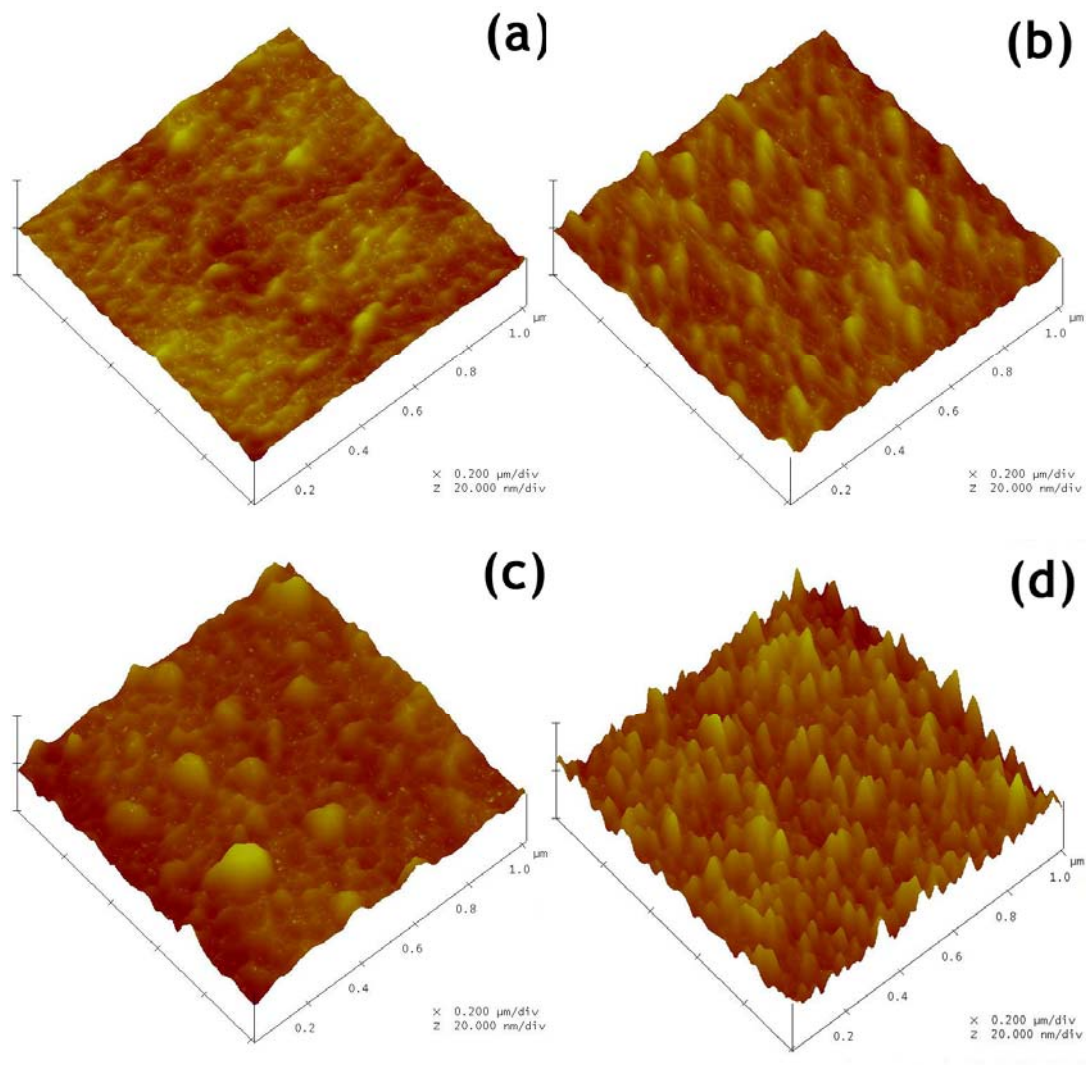


Fig.5.3 AFM images for (a) pristine and irradiated films with fluence (b) 1×10^{12} (c) 3×10^{12} (d) 3×10^{13} ions/cm² (x scale 0.2 micron per division, z scale 20 nm per division)

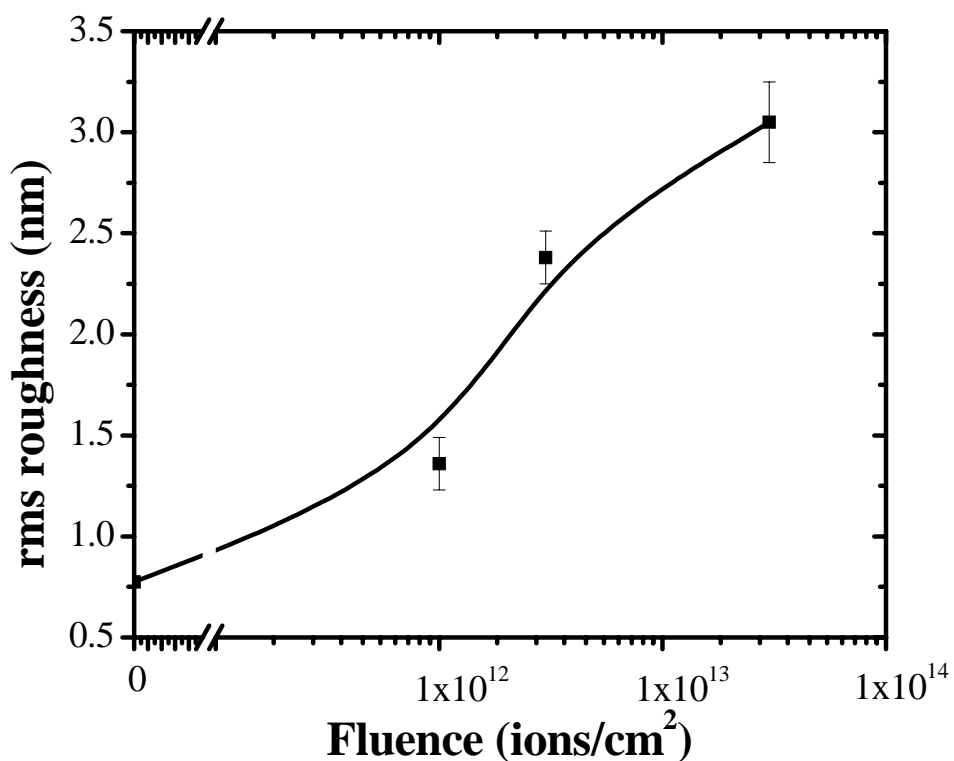


Fig. 5.4 Variation of rms roughness with ion fluence

5.3.3 Vibrating sample magnetometer studies

Figure 5.5 shows the hysteresis loop for pristine and irradiated films measured with the applied field parallel to the film plane. It can be noticed that the coercivity for pristine and irradiated films are different. The variation of coercivity with fluence is plotted and is depicted in figure 5.6. The squareness ratio (M_r/M_s) for pristine and samples irradiated with swift heavy ions at various fluences of 1×10^{12} , 3×10^{12} and 3×10^{13} ion/cm² are 0.75, 0.67, 0.50 and 0.44 respectively. It is clear that the squareness decreases with increase in the ion fluence.

5.4 Discussions

GAXRD studies showed that both pristine and irradiated films are amorphous. It is to be noted that Rizza *et al.* observed a crystallization phenomena in $\text{Fe}_{73.5}\text{Nb}_4\text{Cr}_5\text{Cu}_1\text{B}_{16}$ and $\text{Fe}_{90}\text{Zr}_7\text{B}_3$ meltspun ribbons [118]. The non observance of such a phenomena in the present case can be due to following reasons. Ion Fluence in the present case ($\sim 10^{13}$ ions/cm²) is high so that it may be above a critical fluence. Assuming that $1 \leq S_c/S_{th} \ll 2.7$, the ion track radii can be approximated as $R_c^2 = \ln S_c$ [119].

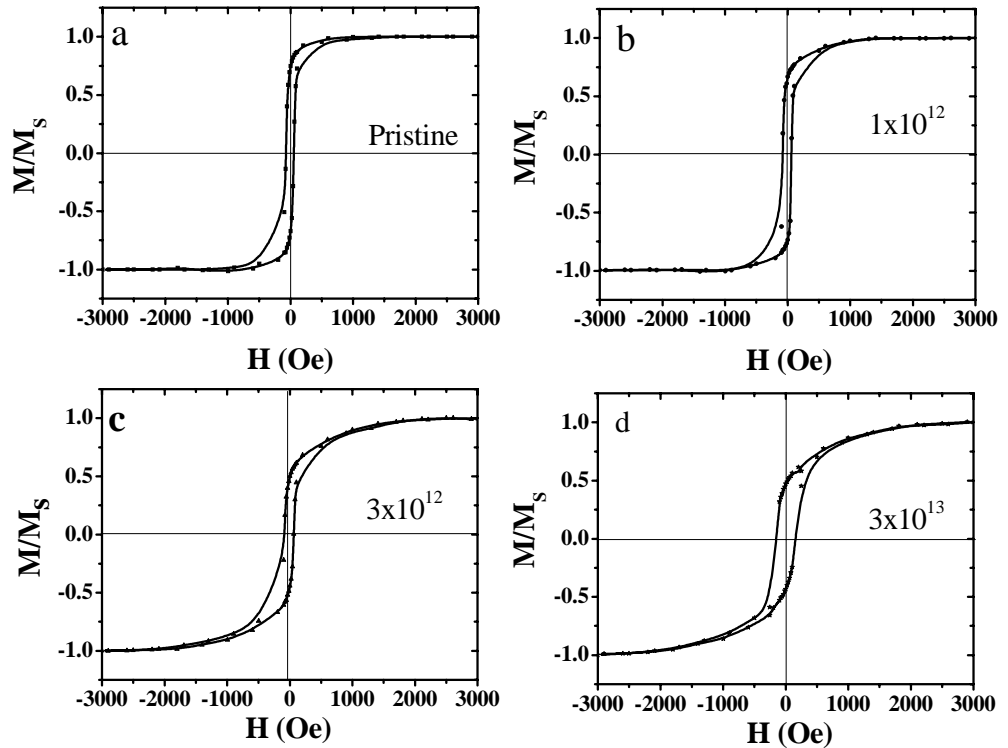


Fig. 5.5 Room temperature hysteresis loops for (a) pristine and irradiated films at a fluence of (b) 1×10^{12} (c) 3×10^{12} (d) 3×10^{13} ions/cm²

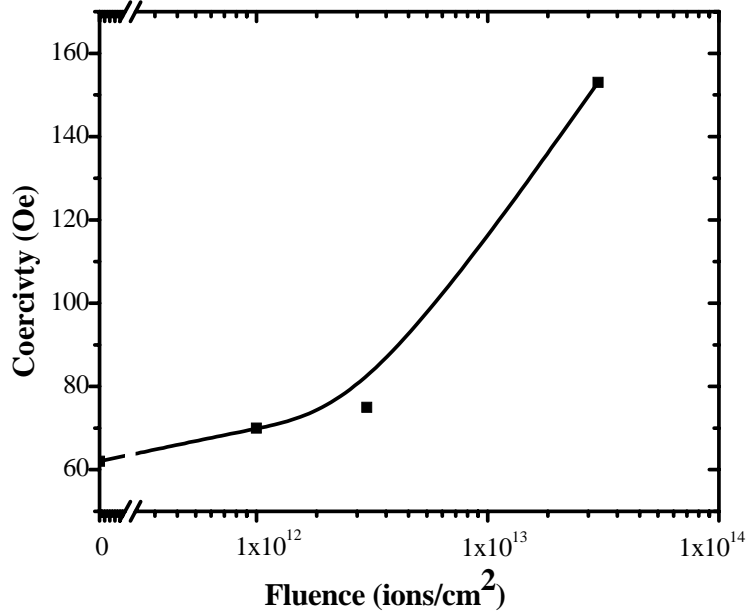


Fig. 5.6 Variation of coercivity with ion fluence

Here R_c is the track radius, S_e is the electronic energy loss and S_{th} is the threshold energy for track formation. The approximate value of R_c in the present study is ~ 1.8 nm. Since the estimated track diameter is ~ 3.6 nm, the 1 cm^2 sample will be fully covered with ion tracks at a fluence of about 1×10^{13} , corresponding to $1/\pi R_c^2$. Therefore there will be a considerable overlapping of tracks at 3×10^{13} ions/ cm^2 . The impinging ions may overlap and therefore there will be an enhanced probability for re-amorphisation or sputtering of the crystallites formed if any. The chemical composition is different in the present work [rich in Fe, Ni and deficient in metalloids (B and Mo)]. It has been previously reported that the local composition plays a major role in stabilizing or destabilizing the amorphous structure upon swift heavy ion bombardment [118]. Also in the previous work the ion energy was in the GeV regime and linear electronic energy deposition in the present work is low (~ 28 keV/nm) when compared to the previous work (~ 45 keV/nm) [118]. Regardless of roughness

variation, AFM images show that the lateral size of the surface features increase with ion fluence and at 3×10^{13} ion/cm² the size decreases. Ion beam irradiation is known to increase the adatom diffusivity [120]. It is clear from AFM images that the pristine samples itself has some irregularities on the surface with an average height of ~ 0.6 nm. The diffusing atoms can be trapped by these irregularities resulting in the accumulation of adatoms. This results in an increase in the lateral size with ion beam irradiation. It is also to be noted that the estimated fluence for track overlapping is $\sim 1 \times 10^{13}$ ions/cm². The reduction in lateral size at 3×10^{13} could be due to the fragmentation of surface structures as a result of multiple ion impacts on the surface.

The topographical evolution of a solid surface during ion beam irradiation is governed by the interplay between the dynamics of surface roughening that occurs due to sputtering and smoothing induced by material transport during surface diffusion. The increased surface roughness with fluence implies that the roughening process is predominant here.

The swift heavy ion induced roughening of Fe-Ni surfaces is in accordance with the expectation of an inelastic thermal spike model. According to this model, during the passage of the swift heavy ion a large amount of energy is deposited in the electronic system of the solid and is transferred to the atoms by electron-phonon interaction. The first step in this process is the electronic excitation and ionization along the track of the projectile (with in less than 10^{-16} s). The heat transfer from electronic to atomic subsystem become substantial between 10^{-14} and 10^{-12} s depending on the magnitude of the coupling between both subsystems. After about 10^{-10} s the region virtually cools down to ambient temperatures.

Temperature of the thermal spikes thus generated depends upon (a) the volume in which the energy imparted by the swift heavy ions diffuses due to the mobility of the hot electron gas and (b) strength of the electron-phonon coupling that determines the efficiency of the transfer of the energy from the electronic system to

the lattice. Depending on the amount of energy transferred to the atomic system and the attained temperature, specific phase changes can be induced such as transitions from the solid to liquid phase or liquid to vapour phase. Surface roughening is assumed to be because of the evaporation of atoms from a hot surface heated by an inelastic thermal spike. This gives credence to the hypothesis that swift heavy ion induced sputtering plays a predominant role in the surface roughening process of Fe-Ni thin films.

Similar increase in surface roughness with an increase in ion fluence was also observed by Mieskes *et al* [117] in Gold, Zirconium and Titanium metals. In their work Au, Zr and Ti metals irradiated with 230 MeV Au ions exhibited an increase in surface roughness with ion fluence. In the case of Ti the rms roughness increased from 100 nm to 1 μm range when the ion fluence was increased from 2×10^{14} to 1×10^{15} ions/cm². The increased surface roughness was attributed to the SHI induced sputtering and the combined electronic and nuclear heating effect contributed to the sputtering yield and was explained using an extended thermal spike model.

The observed coercivity changes can be correlated with the surface evolution of the films with SHI irradiation. It is known that surface topography only affects the magnetic properties of the surface region within 10-20 nm depth [121]. Hence surface techniques such as MOKE (Magneto Optic Kerr Effect) bring about a better correlation between the surface morphology and magnetic properties because of their surface sensitivity [122]. However it is to be noted that the thickness of the films in the present study is ~ 35 nm and though VSM is a bulk technique, the hysteresis loop traced by the VSM represent the surface effects due to the limited thickness of the film. The coercive force is a measure of the magnetic field necessary to reduce the net magnetization of a ferromagnetic material from its saturation value in some selected direction to zero in that direction. The coercivity depends on the way in which the magnetization changes. There are two mechanisms by which this occurs a)

by net magnetization rotation 2) by domain wall motion. In soft magnetic materials the change in magnetization is primarily due to domain wall motion. Since this is a low energy process when compared to rotation of the net magnetization, the domain wall motion is associated with small coercive fields. Also it should be noted that pinning centers such as dislocations and grain boundaries are non-existent in an amorphous alloy. So the possible mechanism for the increase in coercivity is the presence of surface pinning states. In the present case the changes in coercivity are entirely due to the modifications on the surface of the film and no other mechanisms (for example nano-crystallization by heating effects of ion beams) are contributing to it. Very small irregularities on the surface of a film inhibit the passage of a domain wall because the energy stored within a domain wall surrounding such a region is smaller than in an undisturbed domain wall and consequently the system energy must be increased to enable the domain wall motion. A possible mechanism involved in this surface pinning can be as follows. When the magnetization within a domain wall intersects the surface, the magnetostatic energy is greater for surface regions which are normal to the domain wall than for those which are not. Consequently, the wall prefers irregular surface regions and may be pinned at such locations [123].

From AFM images and data it is clear that the surface roughness increases with increase in ion fluence and therefore more sites will be available for domain wall pinning and this resulted in an increased coercivity at higher ion fluences [see figure 5.7]. The increase in the value of coercivity with an increase in surface roughness is in line with the observations of other researchers [124-126]. Li *et al.* [124] studied the magnetization reversal process of Co film deposited on plasma etched Si substrates. The increased coercivity was attributed to the contribution of domain wall pinning in the magnetization reversal mechanism. Doherty *et al.* [125] observed an increase in coercivity with increased surface roughness in magnetic multilayer systems. They explained that roughness caused a discontinuity in the magnetization at the surface,

which in turn created a self pinning field due to induced surface or interface magnetic poles. Swerts *et al.* [126] studied the magnetization reversal mechanism and coercivity in 30 nm Fe films deposited on Ag buffer layers having different surface roughness. They observed that coercivity increases with an increase in surface roughness and the magnetization reversal process is influenced by the surface roughness.

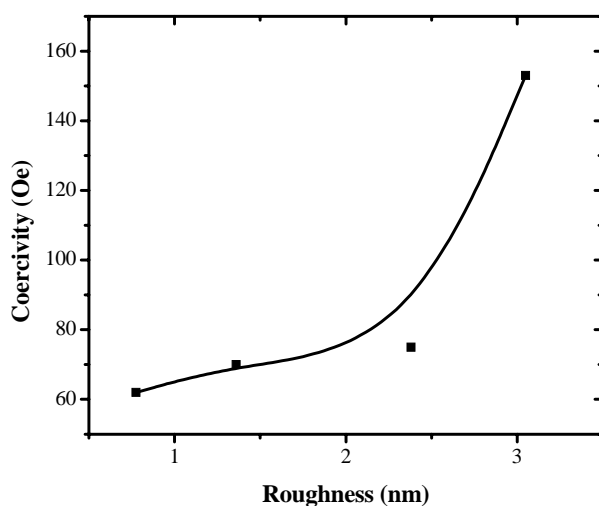


Fig. 5.7 Variation of coercivity with rms roughness

The increase in coercivity with an increase in surface roughness found in the Fe-Ni amorphous alloy is in agreement with the findings of these researchers. The observed decrease of squareness with increase in ion fluence is due to the increase in the in-plane demagnetization factor with an increase in surface roughness [127]. Roughness induced local in-plane magnetic poles results in non uniform response of spins to an applied magnetic field [128]. This increases the saturating field for samples irradiated at higher fluences. Though SHI irradiation deteriorates the soft magnetic properties of the films, the increased coercivity and reasonable remenance (~ 0.5) suggests that a judicious choice of fluence can alter the magnetic characteristics which

suits novel applications of magnetic thin films. For example, there is intense interest, for data storage applications, in patterned magnetic media; in such media magnetic “contrast” is required at periodic intervals. This contrast can be obtained by alternate soft and hard magnetic regions by subjecting selected areas to SHI irradiation. The present study demonstrates that swift heavy ion is an effective tool in modifying the surface morphology of a magnetic thin film. This property can be used for controlling useful magnetic properties like coercivity.

5.5 Conclusions

In conclusion, it was found that bombardment of 108 MeV Ag^{8+} ions can result in roughening of Fe-Ni based amorphous thin film surfaces. The ion irradiation induced roughening can be due to the sputtering phenomena exhibited as a result of high electronic energy deposition. The coercivity of these films was found to increase with an increase in ion fluence. The increased coercivity is due to the increased surface roughness which provides pinning sites for inhibiting domain wall motion. These results are promising and can be useful in tailoring the magnetic properties of a magnetic material in a controlled fashion.

Thermal annealing induced surface smoothening and reorientation of surface magnetization in Fe-Ni thin films

Contents

- 6.1 Introduction
- 6.2 Experiment
- 6.3 Results and Discussions
- 6.4 Conclusion

6.1 Introduction

The magnetic behaviour near a surface or an interface in a magnetically ordered solid may differ in many respects from that of the bulk [129]. The reduced symmetry, lower coordination number, and the availability of highly localized surface and interface states can induce new and interesting magnetic phenomena locally or only at a few atomic layers below, the surface or interface [130-132]. Such changes extend from the surface through the interior to depths ranging from a few tens to several thousands of angstroms or more. The magnetization direction in thin magnetic films can be parallel, intermediate or perpendicular to the surface plane of atoms and is determined by the competition between magnetoelastic, magnetocrystalline and shape anisotropies [40]. The surface anisotropy energy which governs the orientation of film's surface magnetization can be modified by film thickness, roughness, temperature and composition. By changing any of these parameters, the spontaneous magnetization of the surface can be made to switch directions and a magnetization reorientation is possible [41-44]. This transition is a result of competition between spin

orbit coupling, dipolar interaction or an external magnetic field that favors different magnetization directions.

Few theoretical and experimental reports exist in the literature that focuses on the magnetocrystalline contributions to the surface anisotropy [133-137]. Experimental investigations and theoretical calculations by Reichl *et al.* [133] showed that a reorientation transition of the magnetization in Fe/Au(100) from an out-of-plane to an in-plane direction at about three monolayers of Fe. Based on *ab-initio* calculations within the density functional theory, Gallego *et al.* [134] studied the origin of the magnetic reorientation transition in Fe/Cu₃Au(001). Hammerling *et al.* [135] provided a better picture on the magnetic anisotropy energy and inter layer exchange coupling in Cu₄Ni₈Cu_NNi₉/Cu(001) trilayers through a combination of experiment and *ab initio* calculations. Hong *et al.* [136] described a novel technique to manipulate spin reorientation transition in ultrathin ferromagnetic films. They observed that the oxygen assisted surfactant growth of Ni monolayers reduced the surface anisotropy energy which in turn shifted the spin reorientation transition down by about five monolayers. These experimental observations were amply supported by theoretical calculations. Recently, Denk *et al.* [137] observed an extremely sharp spin reorientation transition in ultrathin films of Ni on Cu (110)-(2x1)O.

It is to be noted that most of the studies mentioned above are confined to ultra thin films of a few monolayer thickness. The reason for this is the 1/d dependence of surface magnetocrystalline and magnetoelastic anisotropies. Here 'd' is the thickness of the film. Surface magnetocrystalline and magnetoelastic anisotropies which are major contributors to magnetization reorientation are only active at a few monolayer thicknesses. In thicker films the contributions from surface/interface crystalline as well as magnetoelastic anisotropies will be minimal and the magnetization direction will be predominantly determined by shape anisotropies (magnetic dipole-dipole interactions)

In such films the contributions to surface magnetization can come from dipolar anisotropy [138]. In a thin film with perfectly flat surfaces, in the absence of perpendicular anisotropy, the magnetization will be constant in magnitude and direction, and parallel to the film surface. If surface profile is modulated, the direction of the magnetization within the film surface will wander and thus magnetization \vec{M} becomes a function of position, $\vec{M}(\vec{x})$. Hence magnetic fields of dipolar character are generated both by the effective volume magnetic charge density $-\nabla \cdot \vec{M}$, and also by surface charges which originate in regions where $\vec{M}(\vec{x})$ has a non-zero perpendicular component [138]. Energy density associated with these fields is a function of the angle between the average magnetization, and the preferred direction associated with the modulated surface profile. Thus, a contribution to the surface anisotropy energy is from this dipolar mechanism, which can result in an angular spread of surface magnetic moments in out-of plane directions.

A number of experimental results show that surface and interface roughness in real films greatly affect magnetic properties such as coercivity, magnetic domain structure, magnetization reversal, magnetoresistance, and spin reorientation transition. For example, in a study of ultrathin Fe films on Ag (001), Schaller *et al.* [139] observed spin reorientations induced by morphology changes of the top Fe surfaces and explained the results by a change of both the magnetic dipolar and the magnetocrystalline anisotropy due to the roughness. Weinberger *et al.* [140] reported the influence of interfaces on the magnetoresistance of Au/Fe/Au/Fe multilayer. Lee *et al.* [141] reported the modification of interface magnetic anisotropy in epitaxial Cu/Ni/Cu(002)/Si(100) films by ion beam irradiation and its influence on spin reorientation transition. Pouloupoulos *et al.* [142] performed a scanning tunneling microscopy roughness study of a Ni/Cu (001) thin film surface and concluded that, while the effect is small, roughness favors the easy magnetization direction to be out-

of-the-film plane. Theoretical studies by Zhao *et al.* [143] also predicted a strong dependence of surface magnetization on surface roughness.

However, there are very few direct studies on surface magnetization reorientation of magnetic thin films showing the relation between surface roughness and surface magnetization reorientation even though it is not only a fundamentally interesting issue but also a technologically important issue in developing perpendicular recording media.

In this chapter the observations on annealing induced reorientation of surface magnetization in Fe-Ni based thin films is presented. Here atomic force microscopy (AFM) is employed to procure direct spatial information of the morphology. Direct comparison of the structural results with magnetic force microscopy (MFM) and Ferromagnetic resonance (FMR) measurements enabled to observe magnetization reorientations induced solely by morphology changes.

6.2. Experiment

6.2.1 Preparation

Commercially available METGLAS 2826 MB ribbon of composition $\text{Fe}_{40}\text{Ni}_{38}\text{Mo}_4\text{B}_{18}$ was employed as a source material to deposit Fe-Ni thin films on silicon substrates. The silicon substrates were cleaned with acetone, ethanol and trichloroethylene and were immediately loaded into the vacuum chamber. The distance from source to the centre of 1 cm^2 substrate was 20 cm. The films were deposited by thermal evaporation using a current of 23 A at a pressure of about 1×10^{-5} mbar. The base pressure of $\sim 1 \times 10^{-5}$ m bar was achieved by a diffusion pump backed with a rotary pump. These thin films have also been heat treated at 373 K, 473 K and 573 K to study the surface evolution of the as deposited films. The annealing treatment consisted of increasing the temperature of the samples at about 10 K

/minute to the desired temperature, holding it for 1 h and cooling to room temperature. The annealing was performed in a vacuum of 1×10^{-5} mbar.

6.2.2 Characterization

FMR measurements were carried out on a Bruker ESP 300E spectrometer operating in the X-band (9.47 GHz) at Room temperature. Out-of-plane angular measurements were performed from 0 to 180° in steps of 5° . The imaging of surface morphology as well as magnetic domains was performed with a commercial AFM (Veeco Instrument, Multimode) operated in tapping plus lift mode. This ensures separation between the topographic and magnetic data. A commercial Si tip coated with a CoCr thin film (80 nm thick) that was magnetized vertically was used (Micro Masch NSC35/Co-Cr). The radius of curvature of the tip was less than 90 nm. The full tip cone angle was less than 30° . Images were collected at a tip to sample separation (lift height) of 30 nm. The film thickness which was measured using a stylus profilometer was found to be 25 nm. The composition of the film was found to be $\text{Fe}_{55}\text{Ni}_{45}$. A detailed investigation of the composition and structure of thin film samples carried out using x-ray photoelectron spectroscopy and transmission electron microscopy is presented in chapter 4 and is published elsewhere [69].

6.3 Results and discussions

The surface magnetization direction can be obtained from magnetic force microscopy observations. Figure 6.1 (a), (b) & (c) shows MFM images of the as deposited and films annealed at 473 K and 573 K. The contrast in MFM images indicates out-of-plane magnetic components on the surface. It is clear that the contrast decreases with annealing temperature and almost vanishes at 573 K. The MFM Line scan [figure 6.1 (d)] gives a clear picture of the decrease in out-of-plane magnetic component with increasing annealing temperature. The results indicate that the surface

magnetization direction changes gradually from out-of-plane to in-plane subsequent to thermal annealing.

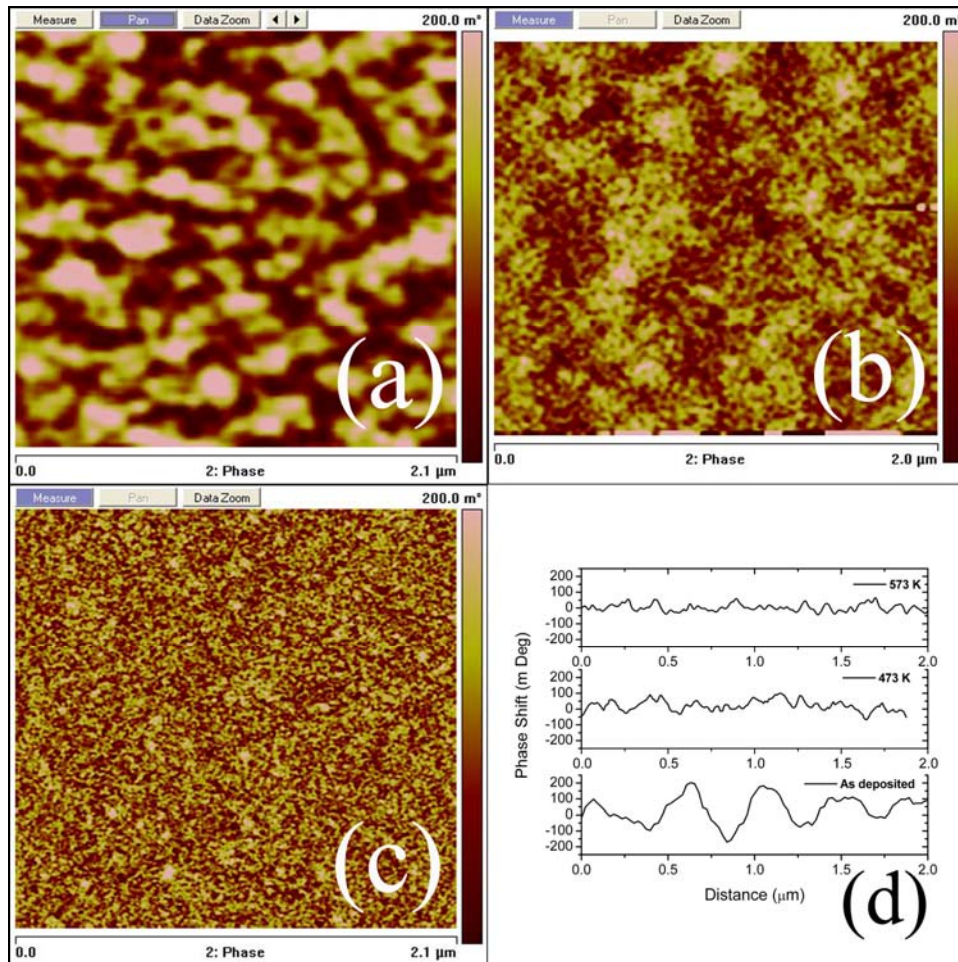


Fig. 6.1 MFM image for (a) as deposited film (b) film annealed at 473 K and at (c) 573 K. Line scan along the MFM images of the three samples is shown in (d)

The direction of surface magnetization is a result of competing forces that favours different directions of magnetizations such as spin orbit coupling, dipolar interaction

or an external magnetic field. The direction of the easy axis of thin films is described by the magnetization anisotropy energy and is given by [144]

$\Delta E = -2\pi M^2 + K_{MC}^b + B^b e + (K^s + B^s e)/d$, where 'M' is the saturation magnetization and 'd' is the thickness of the film. K_{MC}^b is ascribed to bulk magnetocrystalline anisotropy, B^b is the bulk magnetoelastic coupling coefficient, and e is the strain tensor. K^s/d is the magnetocrystalline anisotropy at the surface and $B^s e/d$ is the surface magnetoelastic anisotropy. If ΔE is positive, perpendicular magnetization is favored. FMR studies showed that the bulk magnetization is in in-plane direction in all the films and this indicates the domination of shape anisotropy over bulk magnetocrystalline anisotropy K_{MC}^b and bulk magnetoelastic anisotropy $B^b e$. Moreover, due to the finite thickness of the film (25 nm), the surface crystalline anisotropy K^s/d and surface magnetoelastic anisotropy $B^s e/d$ will be minimal. Hence in the present case the contributions to surface magnetization can be from dipolar anisotropy arising from the rugged surface.

It is to be noted that in the present case we can rule out the role of chemisorbed species (as was observed in some other experiments [145-148]) in surface magnetization reorientation due to the following reasons. XPS curve fitting showed that concentration of metal-oxygen bonds on the surface is more or less the same in both pristine and annealed films. Figure 6.2&6.3 shows the results of Fe 2p XPS studies on both as deposited films and films annealed at 473 K. The percentage of iron in its oxide form is 91% and 92% respectively in as deposited and annealed films. That is within the probing depth of XPS (~2nm) the concentration of oxide phases is more or less the same in both cases. Curve fitting to the O 1s spectra revealed that 85% of the total oxygen on the surface is bonded with metal atoms (figure 6.4 & 6.5). The percentage contribution was the same in both pristine and annealed films. Ni 2p XPS showed that nickel was in pure elemental form in both as deposited and 473 K annealed samples (figure 6.6 & 6.7). Since the oxygen bonded to the surface is same in

both cases, any contributions from this to the magnetization direction will remain the same in both pristine and annealed samples. These enabled to conclude that the observed reorientation of surface magnetization in the present case is entirely due to the surface morphology change on thermal annealing.

Demagnetizing fields due to dipolar interactions have a pronounced effect on the magnetization direction of surface layers. In thin magnetic films with a relatively high saturation magnetization even a small surface roughness can produce significant demagnetizing fields. A simple calculation of the demagnetizing field by Scholmann [55] for 100 nm permalloy film with surface roughness around 0.2 nm shows that the demagnetizing field is roughly around 5 Oe and this is roughly the magnitude of the induced uniaxial anisotropy field observed in such films. It appears very likely that the demagnetizing fields associated with a rough surface have a significant influence on the surface magnetization orientation.

The demagnetizing field of a magnetic material is caused by the generation of “magnetic poles” near its boundaries due to the finite shape of a material. The magnetic poles give rise to a demagnetizing field H_D , which opposes the applied field. The strength of H_D depends on the geometry and magnetization of a material, M . $H_D = N_D \cdot M$ where N_D is the demagnetizing factor which depends on the shape of the magnetic object. For a smooth and infinitely large thin magnetic film, the demagnetizing factor along the out-of-plane direction of a thin film is nonzero. However, if the film is rough, the local roughness features will induce local in-plane “magnetic poles” which can result in a nonzero in-plane demagnetizing factor. The observed surface magnetization reorientation arises from the surface morphology of the different films.

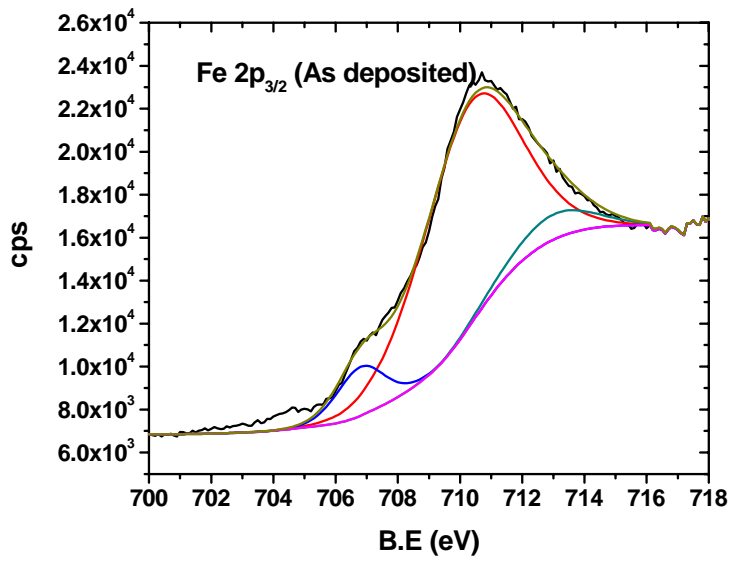


Fig.6.2 Fe 2p spectrum of as deposited film

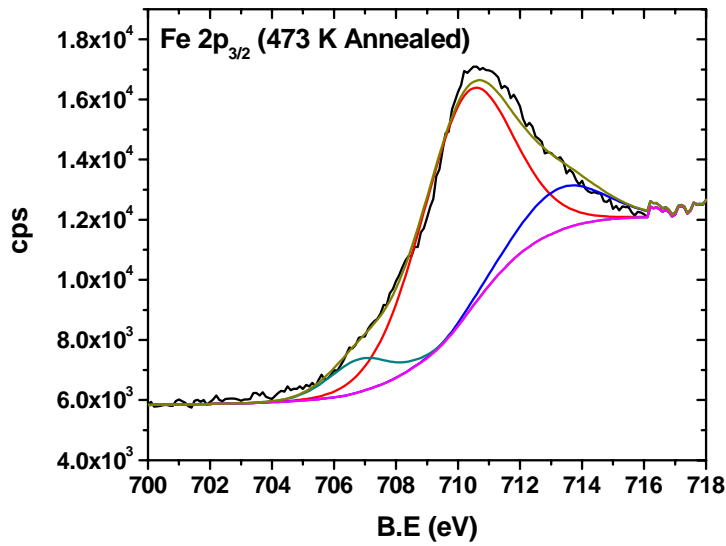


Fig.6.3 Fe 2p spectrum of 473 K annealed film

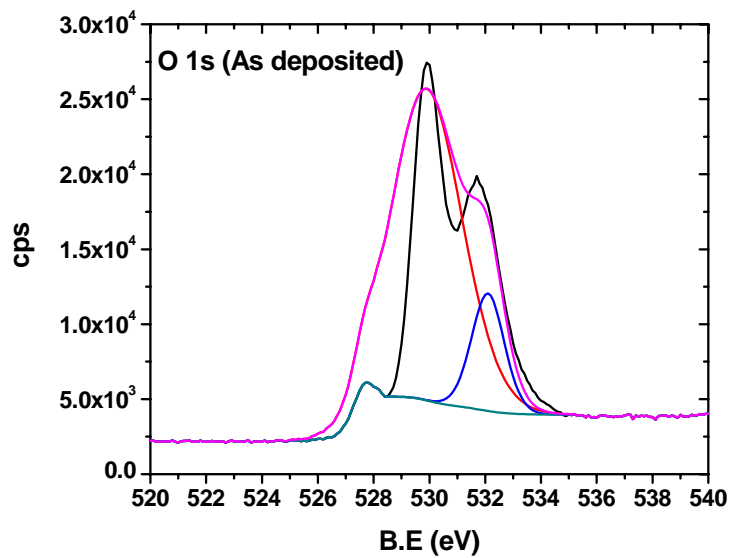


Fig.6.4 O 1s spectrum of as deposited film

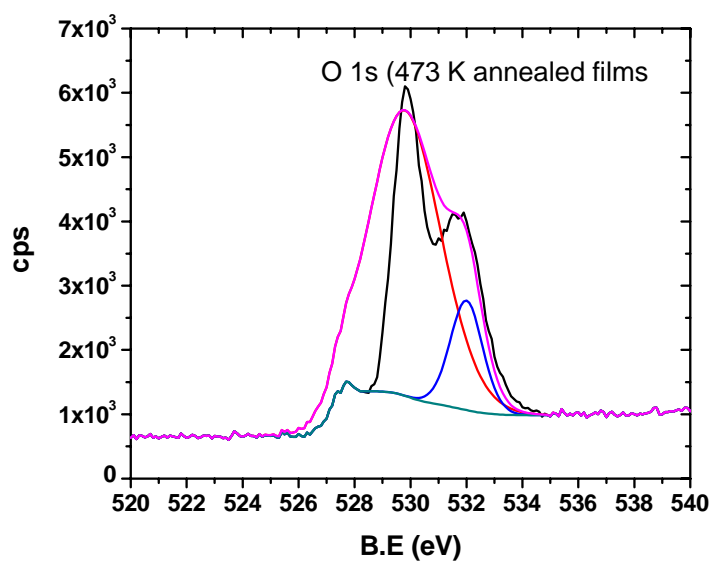


Fig.6.5 O 1s spectrum of 473 K annealed film

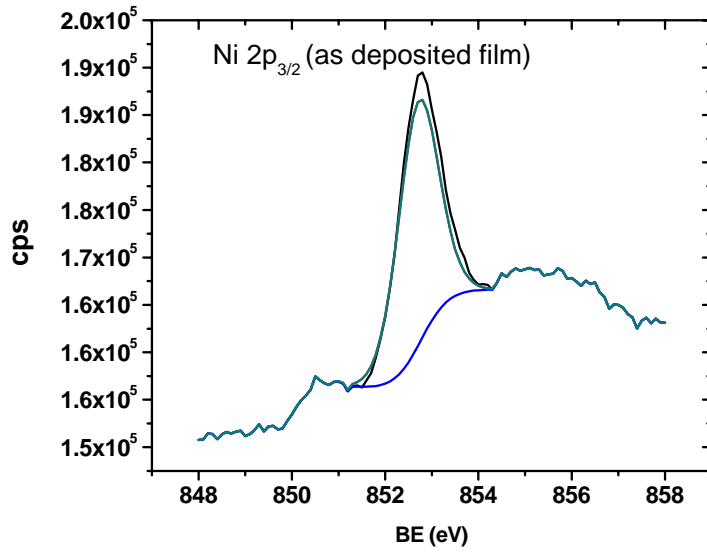


Fig.6.6 Ni 2p spectrum of as deposited film

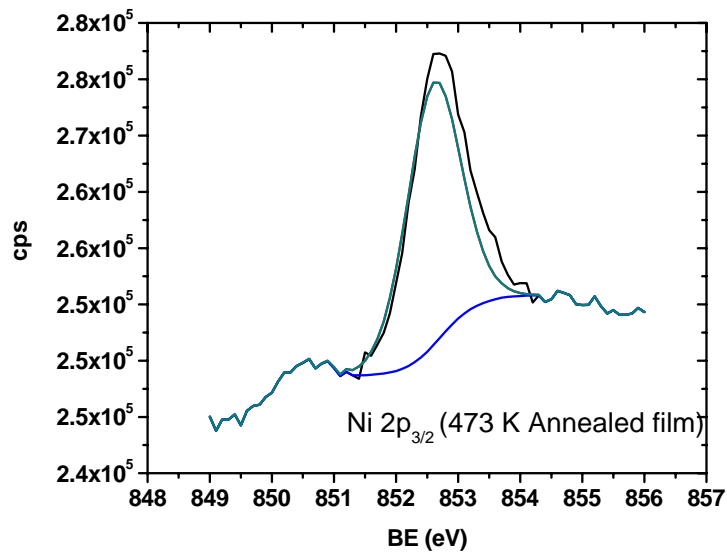


Fig.6.7 Ni 2p spectrum of 473 K annealed film

Figure 6.8 (a), (b) and (c) shows the AFM images of the as deposited and annealed films. The rms roughness determined from the AFM scan are respectively 2.38 nm, 0.76 nm and 0.50 nm for as deposited, 473 K and 573 K annealed samples. It is clear that a smoothening of the film surface takes place with thermal annealing. The decrease in surface roughness on thermal annealing can be due to the surface smoothening induced by ad atom surface diffusion.

Surface roughness can modify the demagnetizing fields. The demagnetizing fields determine the magnetization orientation in shape anisotropic systems. A detailed study on the effect of surface smoothening on the demagnetizing fields was performed employing FMR.

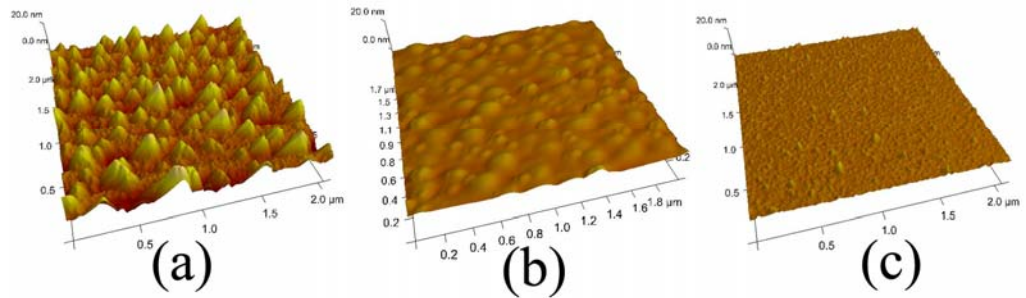


Fig. 6.8 3-D AFM image of (a) as deposited film (b) film annealed at 473 K and at (c) 573 K (z scale 20 nm/ division).

Figure 6.9 illustrates the experimental configuration of the sample for FMR measurements. Here n is a vector normal to the surface of the film. H is the direction of the field applied and θ_H is the angle between n and H .

Figure 6.10, 6.11, 6.12, & 6.13 displays a sequence of FMR spectra as a function of the angle θ_H for as deposited and annealed Fe-Ni thin films at 373 K, 473 K and 573 K. It is clear that a shift of resonance line takes place towards lower fields as the sample is rotated from $\theta_H=0^\circ$ to $\theta_H=90^\circ$.

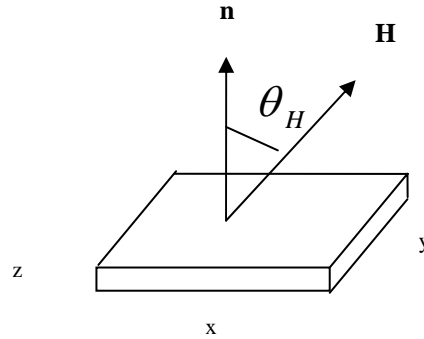


Fig. 6.9 Experimental configuration of the sample for FMR measurements

Figure 6.14 shows the change of resonance field as a function of annealing temperature. In the figure 6.14, $H_r(0)$ and $H_r(90)$ denote the resonance field for the applied dc field perpendicular and parallel to the sample plane respectively. The difference in resonance field $H_r(0) - H_r(90)$ increases with annealing temperature, T_A . As T_A increases, $H_r(0)$ moves towards high field and $H_r(90)$ to low field, i.e., the demagnetizing field increases perpendicular to the plane of the sample and decreases parallel to the film plane. This can be correlated with the change in surface morphology with thermal annealing. AFM images (figure 6.8) showed that the rms roughness of the films decreased to 0.50 from 2.38 nm on annealing at 573 K. Theoretical work by Zhao *et al* [143] points to the fact that for thin magnetic films, the in-plane demagnetization factor should increase with an increase in the surface roughness and correspondingly the out of plane demagnetization factor should decrease. The $H_r(0)$ and $H_r(90)$ variation is thus due to the surface modification of Fe-Ni thin films on thermal annealing. Similar observations were also made by Sang *et al.* [149] in thermally annealed CoAg granular thin films.

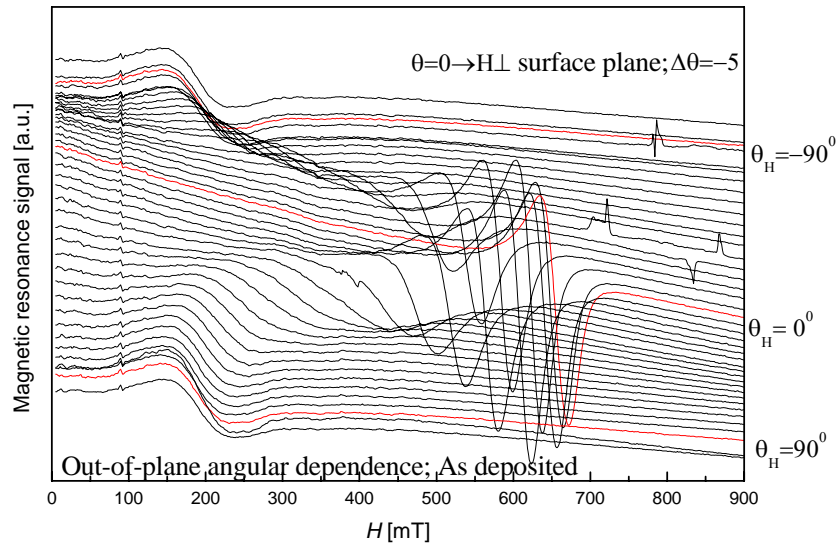


Fig. 6.10 Derivative of FMR signal from as deposited samples and different angles.

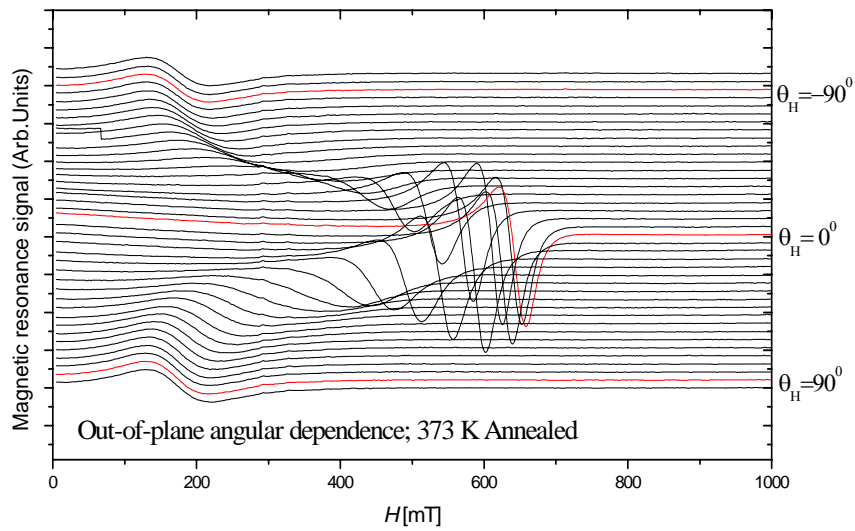


Fig. 6.11 Derivative of FMR signal from 373 K annealed samples and different angles.

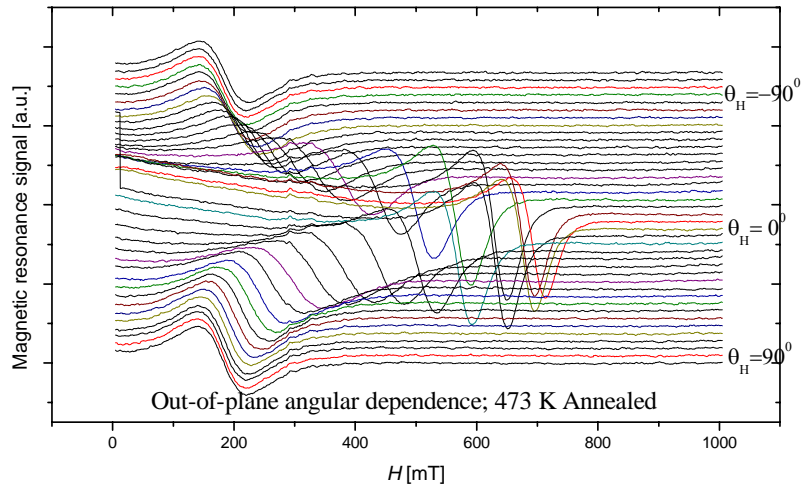


Fig. 6.12 Derivative of FMR signal from 473 K annealed samples and different angles.

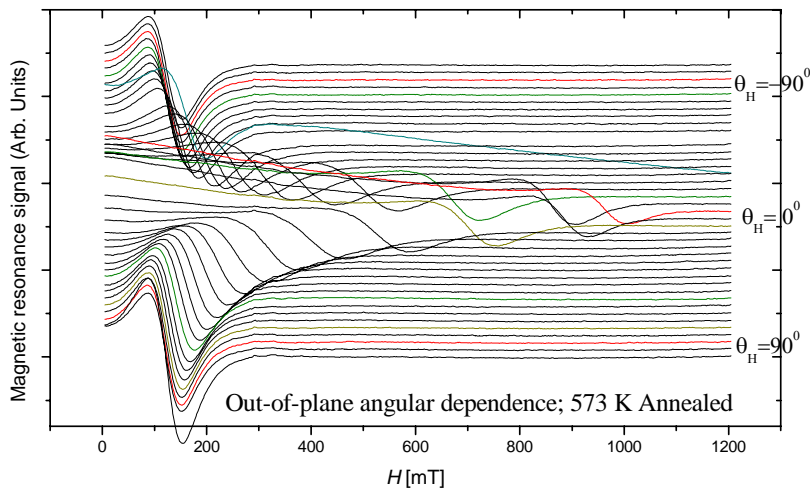


Fig. 6.13 Derivative of FMR signal from 573 K annealed samples and different angles.

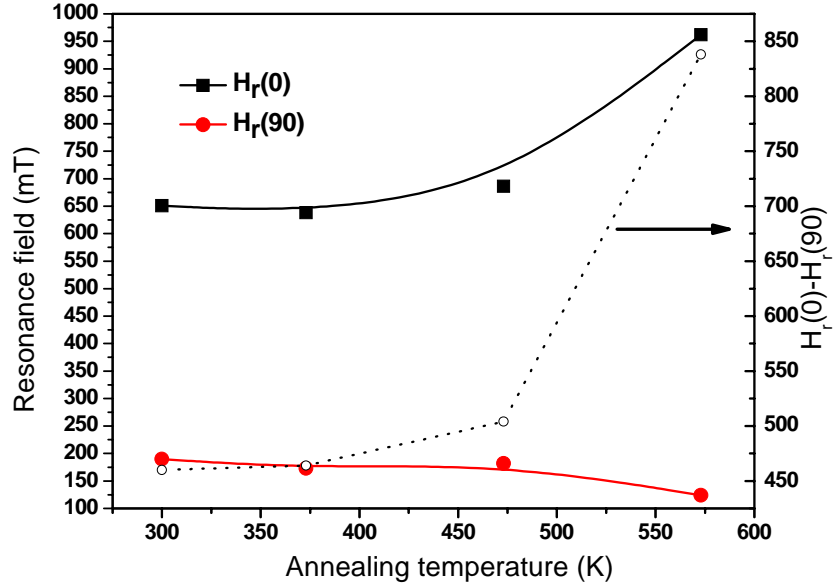


Fig. 6.14 Resonance field and the difference of resonance field, $H_r(0) - H_r(90)$ as a function of annealing temperature. Lines were drawn to guide the eyes.

As mentioned above, the demagnetizing field vector is determined by the shape of the sample and characterized by the demagnetizing factors N_x , N_y and N_z , with $N_x + N_y + N_z = 4\pi$. In the case of smooth thin film, the only component of the demagnetizing field is normal to the plane i.e., $N_z = 4\pi$ and $N_x = N_y = 0$, and will strongly oppose the tilt away of magnetization from the film plane. Note that the increased surface roughness results in another nonzero component of the demagnetizing vector, $N_x, N_y > 0$. Since, the sum of the three demagnetization factors must remain constant $N_x + N_y + N_z = 4\pi$, this implies a reduction of the demagnetizing factor perpendicular to the film, $N_z = 4\pi$. Consequently, a weaker perpendicular demagnetizing field will not be sufficient to sustain uniform in-plane magnetization—an effect that becomes more intense the rougher the surface. In the present case, surface anisotropy due to the dipolar fields has a significant influence on the magnetization direction of surface layers but is not large enough to induce the whole film to switch to an easy direction

normal to the film plane. The results indicate that the surface magnetization direction gradually changes from the out-of film plane direction for as deposited samples to a uniform in-plane magnetization for films annealed at 573 K.

The surface roughness forces the surface magnetization to lie out of plane, allowing geometrical control of the surface magnetization direction of Fe-Ni alloy thin films. It can be deduced that the increased surface roughness of the film modifies the demagnetizing fields forcing the surface magnetization off plane.

Further evidence for the reorientation of surface magnetization can be obtained from the angular dependence of the resonance field. Figure 6.15 shows the angular variation of resonance fields for as deposited samples and samples annealed at 373 K, 473 K and 573 K. It is clear that the peak at $\theta_H = 0^\circ$ is considerably sharper at higher annealing temperature (573 K), because of the tendency of M to remain close to the film plane until θ_H is very close to 0° . Because of the reduced in plane demagnetizing field, uniform in-plane magnetization is observed in films annealed at 573 K.

The out-of-plane angular dependence of line width for different samples is determined and is plotted in figure 6.16. The peak-to-peak line width can have contributions from Gilbert damping as well as from two-magnon scattering [150-152]. Under a fixed FMR frequency and a varying external magnetic field, the contributions of Gibert damping to the line width can be expressed as [40,153]

$$\Delta H_G(\omega) \approx \frac{2}{\sqrt{3}} \frac{G}{\gamma^2 M} \frac{\omega}{\cos \beta_F} \quad 6.1$$

Where G is the Gibert damping parameter and β_F is the angle between M and H. The two-magnon scattering is a process where the $k = 0$ magnon excited by FMR scatters into degenerate states of magnons having wave vectors $k \neq 0$. Unlike the Gilbert damping shown in Eq.6.1 the frequency dependence of two-magnon scattering process

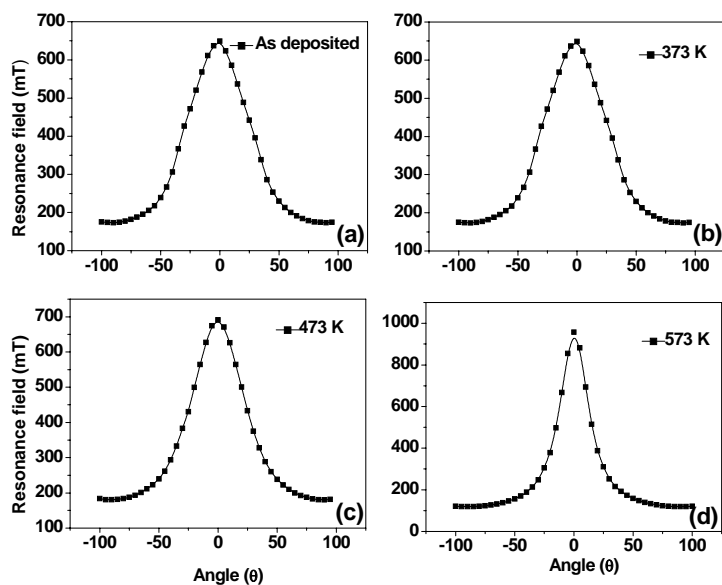


Fig. 6.15 Angular variation of resonance field for (a) as deposited film and films annealed at (b) 373 K (c) 473 K (d) 573 K

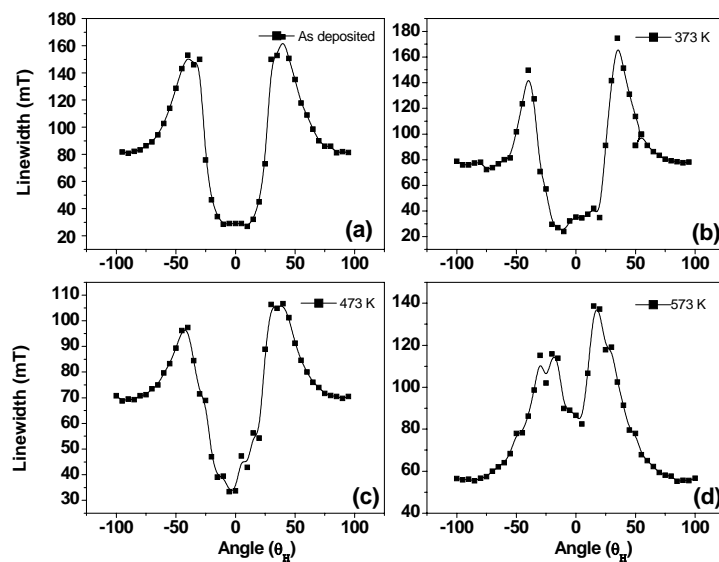


Fig. 6.16 Angular dependence of line width for (a) as deposited film and films annealed at (b) 373 K (c) 473 K (d) 573 K

is not linear with ω . It saturates at very high frequencies and starts with a steep slope at lower frequencies. The contributions of two-magnon scattering to the FMR line width can be expressed as [150-152]

$$\Delta H_{2M}(\omega) = \Gamma \sin^{-1} \frac{\sqrt{\omega^2 + \left(\frac{\omega_0}{2}\right)^2} - \omega_0/2}{\sqrt{\omega^2 + \left(\frac{\omega_0}{2}\right)^2} + \omega_0/2} \quad 6.2$$

with $\omega_0 = \gamma 4\pi M_{eff}$. The prefactor Γ in Eq.6.2 represents the strength of the two-magnon scattering. Apart from these two main contributions, inhomogenities in thin films can also contribute to the FMR line width. The out-of-plane angular dependence of line width in the present case shows a peak at intermediate angles and for a film which was annealed at 573 K the peak was closer to $\theta_H = 0^\circ$. It has been previously reported that both Gilbert damping and two-magnon scattering can contribute to the increase in the line width at intermediate angles [150-151]. The present study was carried out only at a single frequency and it is difficult to discuss the line width in detail. However, detailed investigations are necessary to investigate the influence of surface magnetization reorientation on the FMR linewidth. This is possible by carrying out FMR experiment at different frequencies.

6.4. Conclusions

A reorientation in surface magnetization direction from out-of-plane to in-plane was observed in Fe-Ni thin films on thermal annealing. Annealing induced surface smoothing is a possible reason for the observed changes in the surface magnetization direction. It was found that surface modification by thermal annealing significantly modifies the in-plane and out-of-plane demagnetizing fields in these films.

Fabrication and surface evolution of amorphous nano columns of Fe-Ni grown by oblique angle deposition

Contents

- 7.1 Introduction
- 7.2 Experiment
- 7.3 Results and discussions
- 7.4 Conclusion

7.1 Introduction

Nanostructured form of Fe-Ni amorphous alloys is of great interest due to their potential applications in soft magnetic devices. Magnetic nanostructures, in principle, can be patterned by e-beam lithography. But this technique requires expensive instrumentation and is not very versatile. For instance, the e-beam technique can induce phase transformations in materials upon exposure [154]. An alternative to this is thin film deposition at oblique angles [89]. This technique utilizes physical vapour deposition to deposit films on a substrate oriented at an oblique angle to the vapour source. The vapour atoms travel to a fixed substrate at large oblique angle respective to the surface normal of the substrate. The evaporant nucleates on the substrate and the region behind the nucleus does not receive any further vapour because of the shadowing by the nucleus. Therefore, vapour will only be deposited onto the nucleus. This preferential growth dynamics gives rise to the formation of columnar structures. The morphology of such films will be a resultant of the competition between smoothening due to surface diffusion of adatoms and

roughening due to the self shadowing process. The film surfaces grown under these two competing process usually generate fascinating self affine patterns [155-157].

The experimental set up for oblique angle deposition is very simple. The collimated evaporation beam (in ideal case) has a large incident angle θ with respect to the substrate surface normal [figure 7.1(a)]. Therefore we can treat the incoming vapour flux as a vector F as shown in figure 7.1(b). The flux has two components, a parallel component $F_{parallel}$ given by $F_{parallel} = F \cos \theta$ and a perpendicular component $F_{perpendicular}$ given by $F_{perpendicular} = F \sin \theta$

The substrate will receive the vapor flux from both the vertical and lateral directions. During the deposition of thin film on a smooth surface, initially impinging atoms will randomly form islands on the substrate as shown in figure 7.2 a. As deposition proceeds the initial nucleated islands will act as shadowing centres and all the tallest islands will receive more impinging atoms as compared to the shorter ones (figure 7.2 b). This is called the shadowing effect.

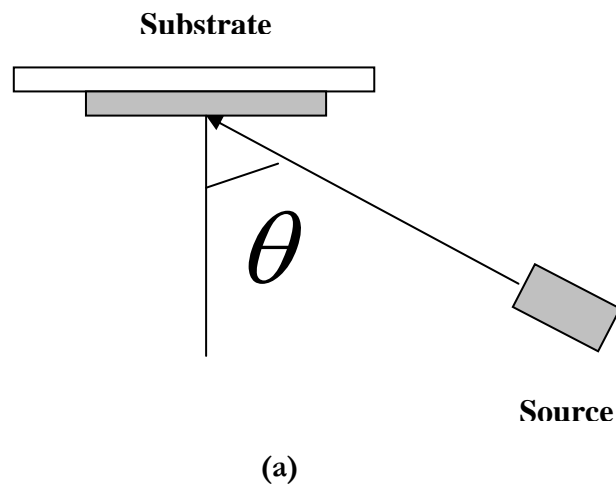
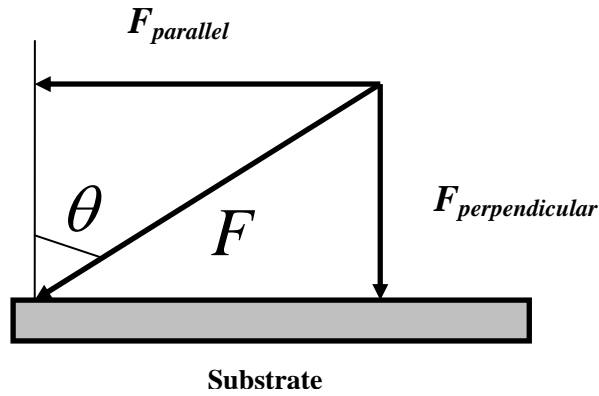


Fig.7.1 (a) Experimental setup for oblique angle deposition



(b)

Fig. 7.1 (b) The incident flux F can be decomposed into two different components $F_{perpendicular}$ is the flux perpendicular to substrate and $F_{parallel}$ is the flux parallel to the substrate.

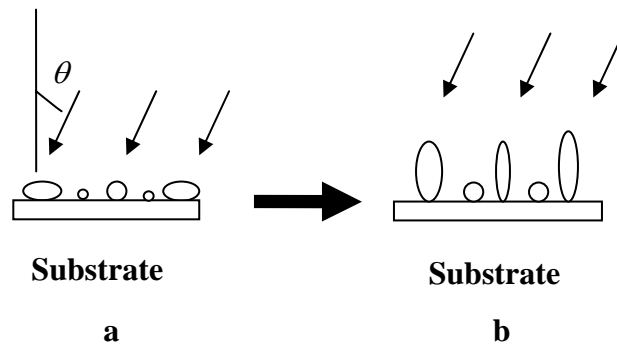


Fig.7.2 Illustration of the shadowing process

This competition process will leave only the tallest islands to grow into columns and a nanocolumnar film is formed. Clearly the horizontal component $F_{parallel}$ is the source for the shadowing effect. The shadow length can be approximated as $L_s = h_s \tan \theta$

where h_s is the height of the surface feature and θ is the angle of incidence. For the oblique angle deposition, since $F_{parallel}$ remains constant during deposition, a columnar film with tilt angle β will be formed.

Generally the tilt angle β will be less than the incident angle θ and follows the empirical tangent rule, $\tan \beta = \frac{1}{2} \tan \theta$ for small θ or the cosine rule

$$\beta = \theta - \arcsin\left(\frac{1 - \cos \theta}{2}\right).$$

Thus the films deposited by oblique angle deposition have the following characteristics. The films are in general porous, possessing nano-columnar structure. The nanocolumns are tilted away from the surface normal to the incident evaporation beam direction. The size and density of the nanocolumns change as a function of the incidence angle θ .

For the synthesis of columnar thin films with both a well-defined value of the surface roughness and well-defined surface morphologies, an understanding on the interplay between the mechanisms involved in the growth process of thin films is essential. From a fundamental point of view, this will enable a classification of the underlying physical phenomena controlling a given growth process. From an applied point of view, a detailed knowledge of the scaling behavior of the rough surface will aid in synthesizing surfaces with well defined roughness and geometry. While so much work has been devoted to understand the effect of deposition parameters on the morphology of elementary metal nano columns, [158-160] there has been less efforts to understand the growth mechanisms of nanostructures of amorphous alloys.

In this chapter, the preparation of Fe-Ni based amorphous nano columns by oblique angle deposition employing thermal evaporation technique is described. Atomic force microscopy is employed to quantitatively investigate the mechanisms involved in the growth process of obliquely deposited magnetic nanostructures.

7.2 Experiment

Commercially available Metglas 2826 MB ribbon of composition $\text{Fe}_{40}\text{Ni}_{38}\text{Mo}_4\text{B}_{18}$ was employed as a source material to deposit Fe-Ni thin films on silicon substrates. Silicon substrates were cleaned with acetone, ethanol and trichloroethylene and were immediately loaded into the vacuum chamber. The films were deposited by thermal evaporation using a current of 25 A at a base pressure of 1×10^{-5} mbar onto substrates oriented at an oblique angle of 40° to the flux. The base pressure of $\sim 1 \times 10^{-5}$ m bar was achieved by a diffusion pump backed with a rotary pump. The source to substrate distance was ~ 26 cm. A set of samples were deposited at an oblique angle of 40° with the same source to substrate distance (~ 26 cm) but with different deposition time (100, 200, 300, 400 and 500 s). The average deposition rate measured by a step profilometer was 6 nm/min.

Transmission electron microscopy experiments were carried out in a Joel JEM-2200 FS electron microscope operated at 200 kV. The compositions of the films were analyzed using an energy dispersive x-ray spectrometer which was attached to the TEM column. X-ray diffraction measurements were performed using an x-ray powder diffractometer technique employing a copper target ($\text{Cu K}\alpha = 1.5418 \text{ \AA}$, Rigaku Dmax C). The scanning speed was adjusted to 2°min^{-1} with a sampling interval of 0.05. X-ray photoelectron spectroscopy (XPS) measurements were carried out using an Omicron Nanotechnology Multiprobe Instrument. XPS spectra were obtained using a high resolution hemisphere analyzer EA 125 HR equipped with a detection system consisting of seven channeltrons. A monochromated Al $\text{K}\alpha$ source of energy $h\nu = 1486.6 \text{ eV}$ was used to probe the films which was attached to a molybdenum sample holder. Pressure in the XPS chamber during the measurements was 5×10^{-10} mbar. Room temperature magnetization measurements were carried out using a physical property measurement system (Quantum Design, USA) with an external field varying from -5 to $+5$ kOe. Images of the film surface were acquired using a Digital

Instruments Nanoscope Atomic Force Microscope (AFM) operated in the tapping mode using an etched single crystal silicon tip. (2 x 2) μm areas were scanned with a resolution of 256x256 pixels. The best known parameter characterizing the morphology of a surface is the rms roughness, which expresses the variation of the height function $h(r,t)$ over a two-dimensional substrate with linear size L .

$$\rho_{rms} = \sqrt{\frac{1}{L^2} \sum (h(r,t) - \bar{h}(t))^2} \quad 7.1$$

where r is the position vector and the mean height is given by $\bar{h}(t) = \frac{1}{L^2} \sum h(r,t)$.

However this description does not account for the lateral distribution of the surface features and a more detailed description of the sample surface topography is provided by the power spectral density (PSD) of the surface roughness which performs the decomposition of the surface profile into its spatial wavelengths. The PSD, which is the Fourier transform of surface heights is defined in its two dimensional form as

$$PSD(k) = \frac{1}{L} \left| \frac{1}{2\pi} \int h(r) e^{-ikr} dr \right|^2 \quad 7.2$$

Where $r=r(x, y)$ is the lateral position vector and $k=k(k_x, k_y)$ is the spatial frequency with wave length $k = \frac{2\pi}{\lambda}$. Also b is the surface height of surface point r and L represents the scan area.

AFM data was used to evaluate the rms roughness. In addition, the surface microstructure was studied using power spectral density (PSD) function calculations. The two dimensional PSD (2D PSD) calculations were performed using the software provided by Digital Instruments. The imaging of magnetic domains was performed with a commercial AFM (Veeco Instrument, Multimode) operated in tapping plus lift mode. This ensures separation between the topographic and magnetic data. A

commercial Si tip coated with a CoCr thin film (80 nm thick) that has magnetized vertically was used (Micro Masch NSC35/Co-Cr). The radius of curvature of the tip was less than 90 nm. The full tip cone angle was less than 30° . Images were collected at a tip to sample separation (lift height) of 40 nm.

7.3 Results and discussions

The X-ray diffraction (XRD) patterns of the samples were featureless except for the peaks from the substrate. Figure 7.3 shows the XRD of a representative film grown on the Si substrate. The diffraction pattern indicates that the prepared samples are amorphous in nature. Transmission electron microscopy (TEM) bright field image (plan view) of the sample is shown in figure 7.4 (a). The microstructure exhibits contrasts typical of an amorphous material. The electron diffraction pattern [Figure 7.4 (b)] consists of a diffraction ring which is characteristic of an amorphous material.

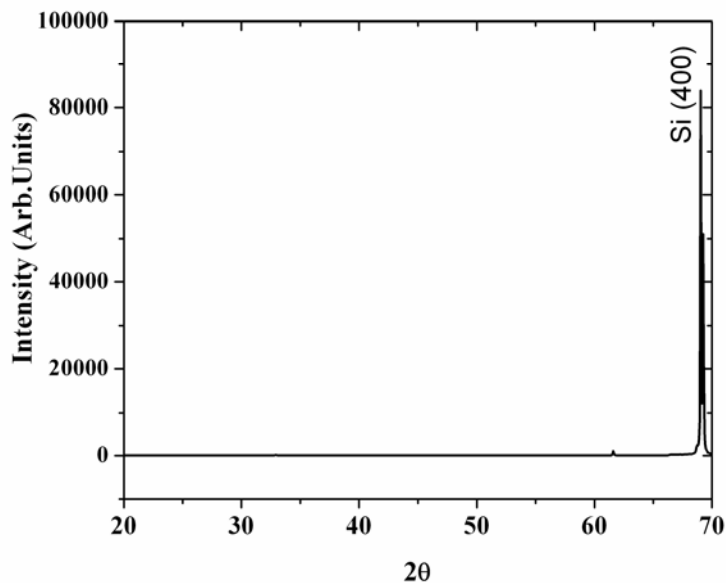


Fig.7.3 X-ray diffraction pattern for a film grown on silicon substrate

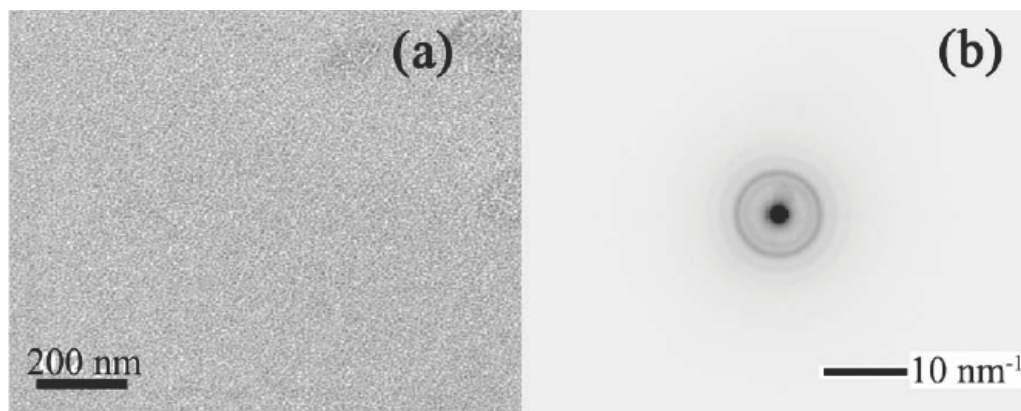


Fig.7.4 (a) Transmission electron microscopy bright field image of thin film (b) corresponding electron diffraction pattern

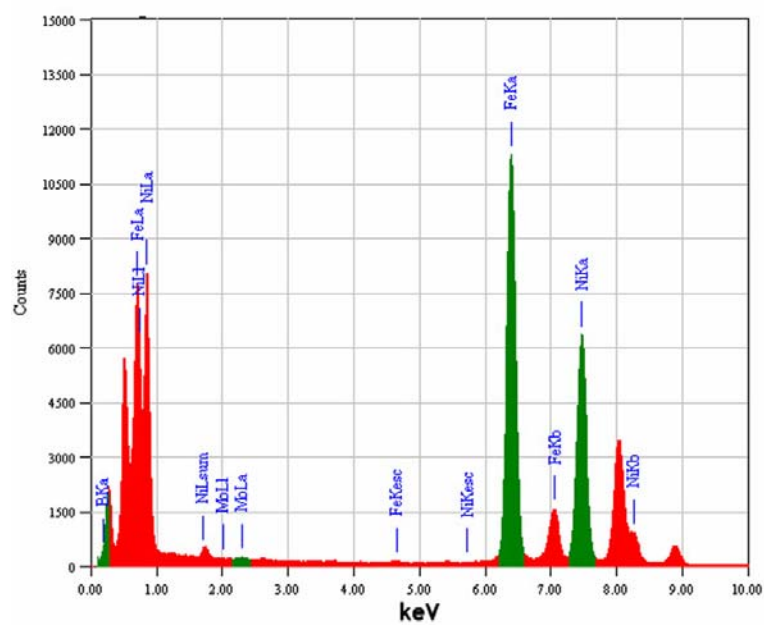


Fig.7.5 Energy dispersive x-ray spectrum for the film.

Figure 7.5 depicts the energy dispersive x-ray spectrum obtained during TEM measurements. The spectrum shows the presence of Fe and Ni. The composition of the films was estimated from the peak intensities of Fe $K\alpha$ and Ni $K\alpha$ lines in the spectrum. The atomic percentage of Fe and Ni were 55 and 45 respectively. X-ray photoelectron spectroscopy (XPS) survey scan was collected for films coated on Si substrates (figure 7.6). The spectrum exhibits characteristic photoelectron lines of Fe, Ni, O and C. The C 1s peak corresponds to the contaminant carbon on the top surface of the specimen. The O 1s spectrum consists of peaks originating from oxygen in metal-oxygen bond. The survey scan also exhibited lines corresponding to the emission of Auger electrons (Ni LMM, Fe LMM and O KLL).

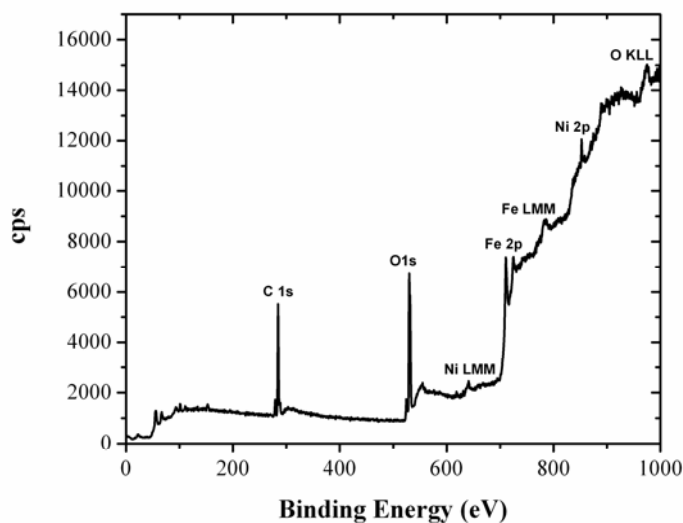


Fig.7.6 X-ray photoelectron spectroscopy survey scan of the nano columns on silicon substrate.

Figure 7.7 shows the AFM images of Fe-Ni film surfaces which were grown at different conditions as described above. The comparison between column height and total thickness of the film suggests that filling of voids in between the column is taking

place during the growth. In any columnar growth the trade off is between the ad atom surface diffusion and self shadowing. Such a growth on a randomly seeded substrate usually results in deposits in between the columns. Because of these deposits, the portion close to the substrate will become a continuous layer and the geometry of the whole system will be layer plus island type, in which islands are arranged on top of the layer. This is further supported by cross sectional TEM image shown in figure 7.8. From the AFM sectional analysis it can be seen that the lateral size as well as surface height (peak to valley) of the columns grows with increase in the deposition time (figure 7.10).

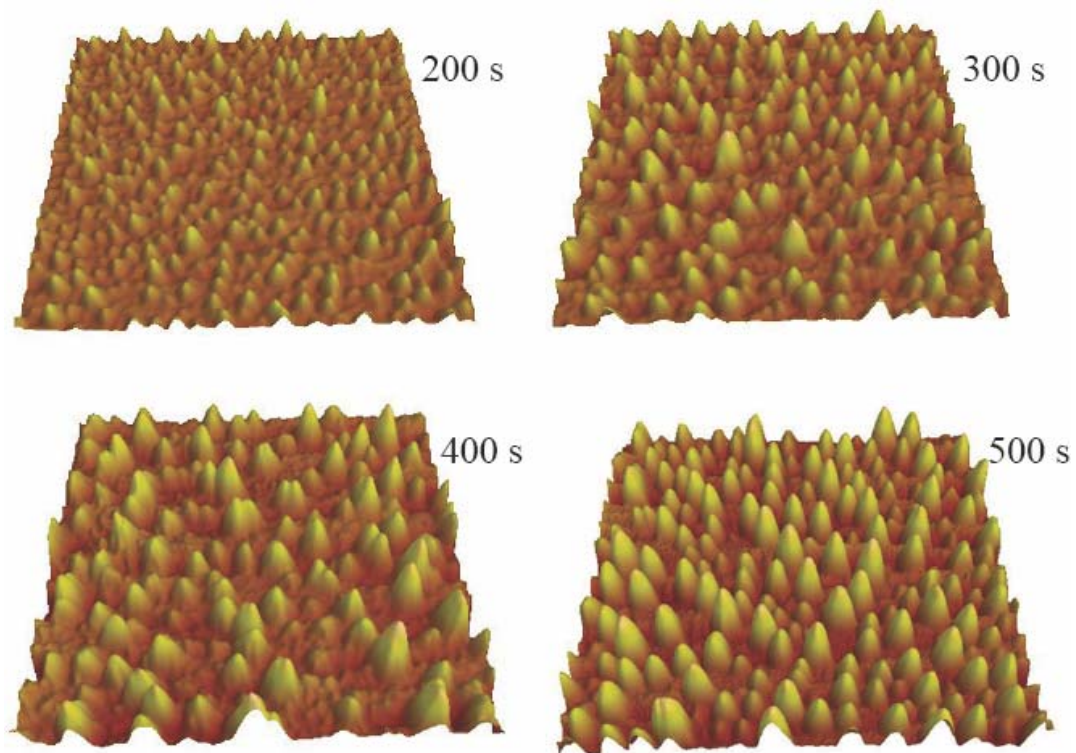


Fig.7.7 3-D AFM image for a film obtained after a deposition time of 200 s, 300 s, 400 s and 500 s. AFM images are $2 \times 2 \mu\text{m}^2$ with z scale 20 nm.

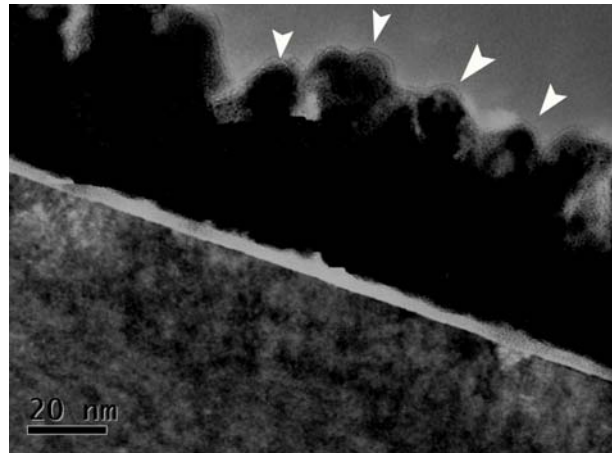


Fig.7.8. Cross sectional TEM of Fe-Ni films on silicon substrate obtained after a deposition time of 500 s (the arrows show the position of islands)

Figure 7.9 depicts plot of rms roughness versus deposition time. The change of roughness up to a deposition time of 300 s is sharp while for higher value of deposition time, it is gradual. During the initial stages of growth, the microstructure is strongly affected by shadowing. At this time the columns grow in an un-correlated fashion from the nuclei formed initially. Such an independent growth should agree with the sharp change in roughness for short deposition time. At higher deposition times the change in roughness is minimal implying that a smoothening mechanism by surface diffusion is also prominent. Also as the deposition time increases the lateral growth of columns occurs and this can be due to the surface diffusion of adatoms. The lateral growth of the columns at higher deposition time can be evidenced from the AFM line scans depicted in figure 7.10. Thus for higher deposition time surface diffusion also plays an important role in the growth process of films.

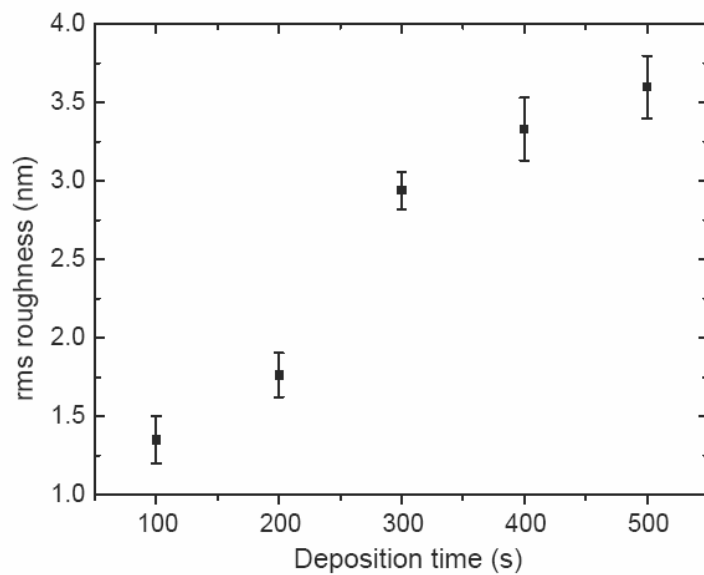


Fig.7.9 Plot of rms roughness versus deposition time

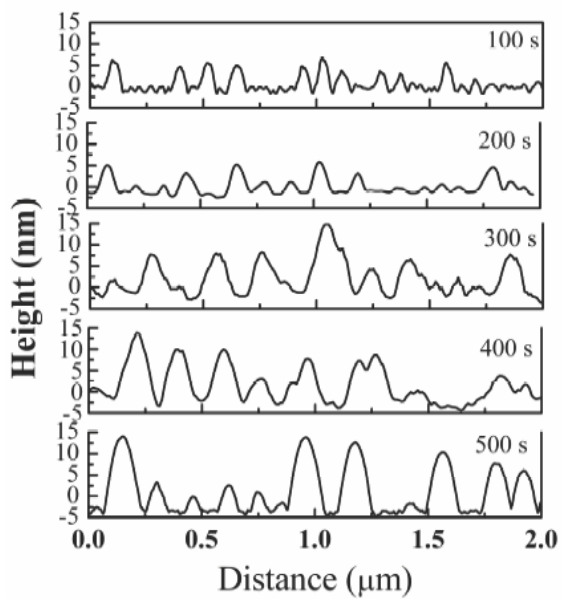


Fig. 7.10 AFM line profile on different samples

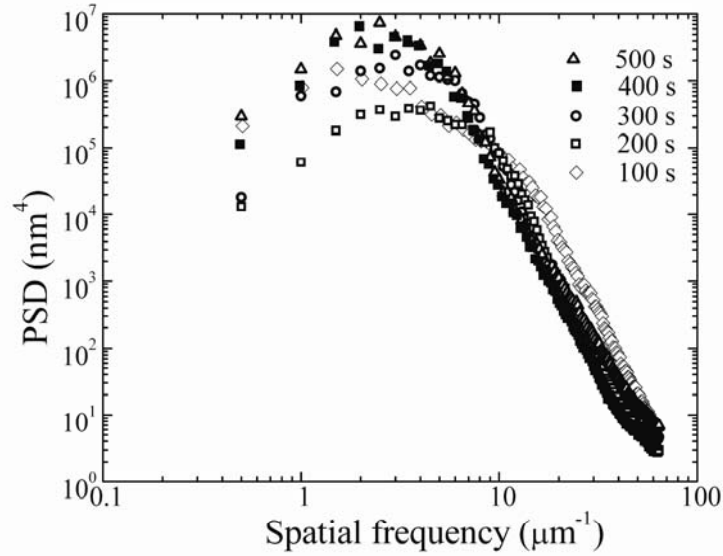


Fig. 7.11 PSD function curves calculated for thin films obtained with different deposition time.

2D PSD calculations were performed for the different films prepared. The 2D PSD spectrum provides the variation of PSD magnitude as a function of spatial frequencies. The power spectral density analysis allows quantification of the surface structure. Figure 7.11 shows log-log plots of power spectra PSD (k) calculated for thin films obtained at different deposition time.

The log-log plot of 2D PSD can be divided into two distinct regimes. The low frequency part which gives an indication of the periodicity of nanostructures and a high frequency part where the PSD distribution is decaying with frequency following a power law $\sim k^{-\gamma_p}$ where k is the frequency and γ_p is the power.

By fitting $\text{PSD}(k) \propto k^{-\gamma_p}$ to the correlated part we obtain $\gamma_p \sim 5.28, 5.4, 5.61, 6.33, 6.69$ for the films grown at deposition time 500, 400, 300, 200 and 100 s respectively. Since γ_p is related to the roughness exponent α_p by the equation [161]

$\alpha_p = (\gamma_p - d_p) / 2$ where the line scan dimension d_p is 2 in our case, the roughness exponent has a value $\alpha_p = 1.64, 1.7, 1.8, 2.15$ and 2.34 for the deposition time 500, 400, 300, 200 and 100 s respectively. It is to be noted that surface diffusion effects that lead to smoothening will lower the exponent; on the other hand, shadowing will increase the exponents [161]. The lowering of roughness exponent at higher deposition time indicates that at higher deposition time, a smoothening mechanism by surface diffusion is also prominent in the growth process of the film. This supports our inferences derived from the roughness versus deposition time plots (figure 7.9).

Moreover a non saturation behaviour of PSD function curves can be observed in the low frequency regime. The non saturation behaviour of PSD has been previously observed in mound structures grown by oblique angle deposition technique [162]. Figure 7.12 shows column separation versus deposition time. It is clear that the column separation increases with deposition time and shows saturation at higher deposition time. The column separation is exactly the shadowing distance. The shadowing length increases with the height of the column according to the equation, $L_s = h_s \tan \theta$ where L_s is the shadowing length, h_s is the height of the surface feature and θ is the oblique angle. Initially, due to the random effect during growth, some surface features become more prominent than nearby ones and they get additional flux resulting in an increase in the shadowing length. As the deposition time increases the columns become more uniform in length and after a critical deposition time shadowing length does not increase significantly.

The room temperature hysteresis curve for films deposited at 200, 300 and 400 s recorded both in the in plane and out of plane geometry are depicted in figure 7.13 a, b and c respectively. The saturation magnetization was found to be ~ 870 emu/cc. It is to be noted that a low field of ~ 2000 Oe was only necessary to saturate the

magnetization in the in plane while a field as high as 5000 Oe or above could not saturate the material in the out of plane geometry.

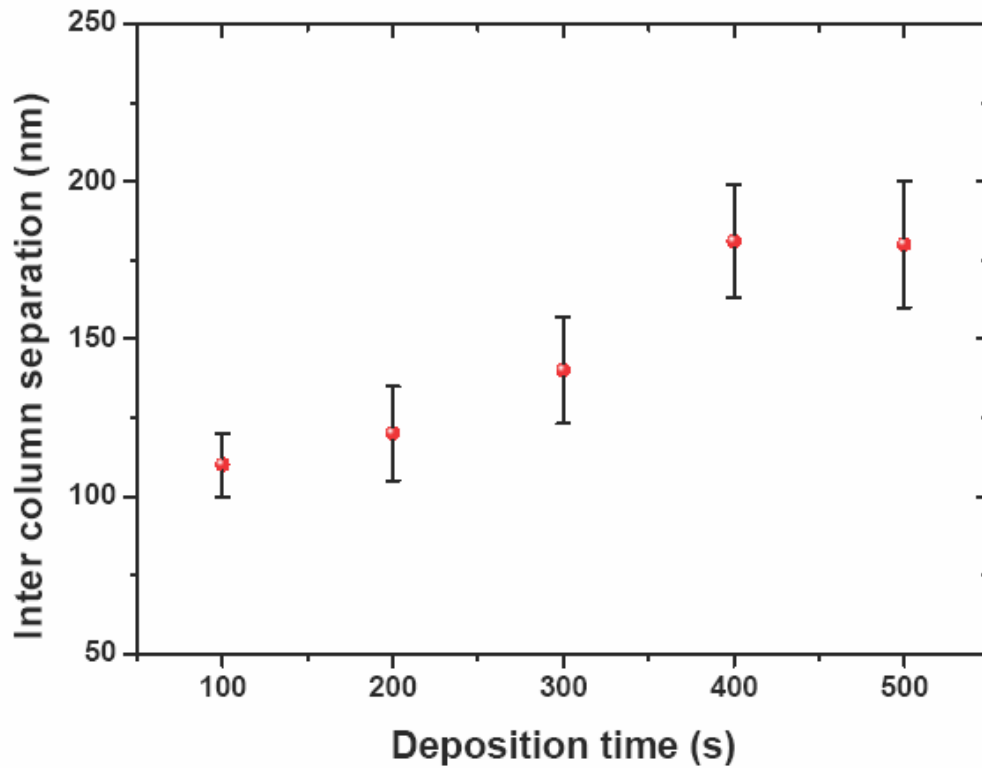


Fig. 7.12 Plot of distance between columns versus deposition time

The vibrating sample magnetometry (VSM) results show that the easy axis of magnetization is in the plane of the film. The magnetic force microscopy (MFM) image for a film deposited at 300 s is depicted in figure 7.13 d and this shows the existence of circular domains with an out of plane magnetic component.

A comparison of AFM and MFM images shows that there is a one to one correspondence between the domains observed and the columns formed. It is to be noted that imaging was done using a Si tip coated with a Co-Cr thin film (80 nm thick) that was magnetized vertically and at a tip to sample separation (lift height) of 40 nm.

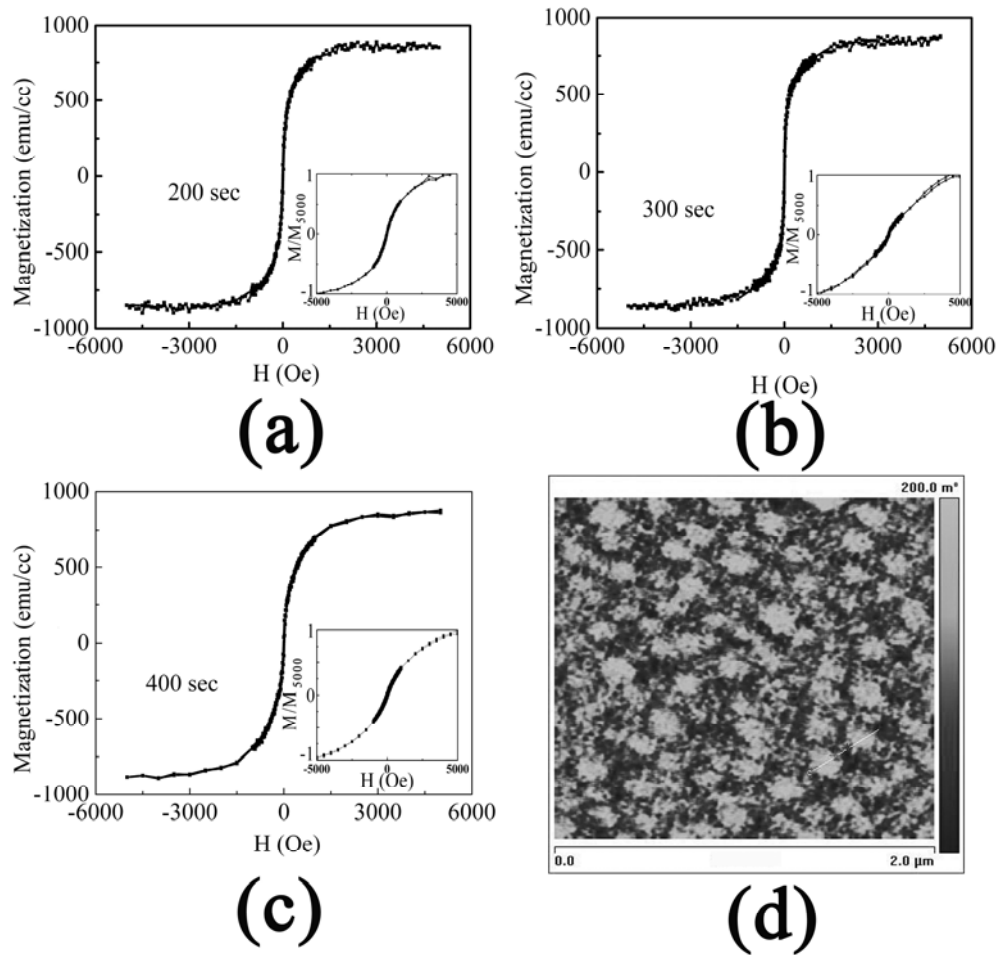


Fig. 7.13 Room temperature hysteresis loops for films obtained after a deposition time of 200 s **b**) 300 s and **c**) 400 s in parallel field. Inset shows the corresponding hysteresis loops for perpendicular field and **d**) MFM image for a film deposited at 300 s ($2 \times 2 \mu\text{m}^2$, z scale 200 m Deg).

The lift height of 40 nm is greater than the film roughness (~ 3 nm) and so the chances of topographical influence on the MFM signal can be negligible. In systems

where shape anisotropy is predominant, the easy axis of magnetization will be along the direction of long axis. If there are deposits in between the columns, the portion close to the substrate will become a continuous layer and the geometry of the whole system will be a layer plus island type in which islands are arranged on top of the layer. Due to the absence of magneto crystalline anisotropy the magnetization direction will be more influenced by the shape anisotropy. In the layer, where the long axis is along the plane of the substrate, the magnetic direction will be in plane. While in the islands, where the long axis is perpendicular to the plane of the substrate, the magnetic direction will be out of plane. The magnetization measurements using VSM is rather a bulk technique and one will only notice signatures of in plane anisotropy because of the domination of the contributions emanating from the layer. However MFM being sensitive to the local detects the out of plane component from the islands. The measurements show that the perpendicular anisotropy from the columns is small and this can be due to their small aspect ratio.

7.4 Conclusions

In conclusion Fe-Ni based amorphous nano columns were grown on Si substrates by oblique angle deposition. The films were grown at different deposition times at an oblique angle of 40° . AFM was employed to quantitatively investigate the surface roughening process in the oblique angle vapor deposited amorphous thin films.

Surface scaling analysis through roughness and PSD spectra showed that at low deposition time, the growth mechanism is dominated by self shadowing, while for higher deposition time surface diffusion is also contributing to the growth process. This situation resulted in the lateral growth of nanostructures at higher deposition times. From an applied point of view the method of obtaining magnetic nanostructures using this low-tech method is interesting and one should evolve preventive measures against surface diffusion while making attempts to get isolated

nano structures. This can be realized by performing the deposition on a patterned substrate or through substrate rotation.

Influence of substrate topography on the growth and magnetic properties of obliquely deposited amorphous nano columns of Fe-Ni

Contents

- 8.1 Introduction
- 8.2 Experiment
- 8.3 Results and Discussions
- 8.4 Conclusion

8.1. Introduction

Due to their potential applications in magnetic sensors and magnetic recording heads [163-166] soft magnetic nanostructures assumes significance from an applied point of view. Several strategies have been developed for the growth of nanostructured magnetic materials [167-171]. Nanolithography-based methods, solution-based approaches and template-based methods are some of them. Some of these methods, however, require high temperatures and special conditions while in other cases, they demand complex and tedious procedures. For instance, in template assisted growth of nanostructures, the selection of suitable catalysts and templates is not straightforward, and the removal of templates and the stabilization of unsupported nanostructures represent crucial issues that may compromise the structural and physical properties. The capability of obtaining ordered arrays of well-defined and periodic nanostructures in an accurate, fast, and inexpensive fashion would be of great interest not only from an applied perspective but also from a fundamental point of view.

Oblique angle vapour deposition offers advantages of fabrication of nanostructures over large areas, as required in many advanced technological and industrial applications [89,172-178]. Some other advantages of this technique are the non requirement of templates, relatively low temperatures and less harmful chemicals for the nanostructure fabrication [179].

Generally, the morphology of the nanostructures thus obtained is influenced by the substrate surface roughness and the growth conditions used for the film formation along with oblique angle, deposition rate, deposition time etc. The growth of nano structures will be the resultant of the competition between the smoothing due to adatom surface diffusion and roughening by self shadowing. For the synthesis of well defined nanostructures having appropriate separation and clear surface morphologies, an understanding on the interplay between the mechanisms involved in the growth process is essential. From an applied stand point, a detailed knowledge of the growth behaviour of the nanostructures on a solid surface will aid in synthesizing nanostructures with well defined roughness and geometry.

To date, ferromagnetic nano columns have been grown by vapour phase co-deposition and oblique angle vapour deposition [57-60]. Fe-Ni-Co nano columns were grown by the self organization of vapour phase co-deposited Fe-Ni-Co [58]. Nano columns with Co/Cu bilayers were obtained by two-source oblique angle vapour deposition [59]. The surface evolution of amorphous nano columns of Fe-Ni obtained by oblique angle vapour deposition on silicon substrate has been described in previous chapter and is published elsewhere[180]. It was found that the growth of nanostructures on a silicon substrate were more or less random and surface diffusion of adatoms led to the coarsening of the columns at higher deposition time.

There are many potentially attractive applications for these columnar films, if they can be prepared with the desired microstructure and inter column separation within the practical limits of time and expense. A critical issue concerning the

achievement of this goal is the control of nucleation. The nucleation events occur preferentially on defects and abnormalities on a substrate surface. While so much work has been devoted to understand the effect of deposition parameters on the morphology of elementary metal nano columns [120,158-160], there has been virtually no effort to understand the influence of substrate topography on the growth mechanisms and magnetic properties of nanostructures of amorphous alloys. A study relating the substrate surface roughness with column evolution and magnetic properties will be important not only from a fundamental perspective but also from an applied stand point.

The main objective of the work presented in this chapter is to investigate the influence of substrate surface roughness on the morphology and the separation between the nanostructures in oblique angle vapour deposition. Fe-Ni based amorphous nano columnar structures were obtained on silicon and glass substrates having different initial surface features. Growth of columns on different substrates is studied using atomic force microscopy (AFM). Further, the evolution of magnetic properties with column growth is studied using atomic force microscopy and magnetic force microscopy (MFM) techniques. The combined use of AFM and MFM will aid in understanding the intricate relationship between the magnetic properties and the nanoscale sized surface features. The MFM measurements are supplemented with vibrating sample magnetometry (VSM) to correlate the average magnetic properties with microstructure.

8.2. Experiment

8.2.1 Preparation

Commercially available Metglas 2826 MB ribbon of composition $\text{Fe}_{40}\text{Ni}_{38}\text{Mo}_4\text{B}_{18}$ was employed as a source material to deposit Fe-Ni thin films on silicon (coded as sample A) and glass substrates (coded as sample B). The substrates

were cleaned with acetone, ethanol and trichloroethylene and were immediately loaded into the vacuum chamber. The substrate was tilted in such a way that the angle between the surface normal to the substrate and the direction of incoming flux was at an oblique angle of 40° . No substrate rotation was provided. The films were deposited by thermal evaporation using a current of 25 A at a base pressure of 1×10^{-5} mbar onto substrates oriented at an oblique angle of 40° to the flux. The base pressure of $\sim 1 \times 10^{-5}$ mbar was achieved by a diffusion pump backed with a rotary pump. The source to substrate distance was 26 cm.

8.2.2 Characterization

The imaging of topography and magnetic domains was performed with a commercial AFM (Veeco Instrument, Multimode) operated in tapping plus lift mode. This ensures separation between the topographic and magnetic data. A commercial Si tip coated with a Co-Cr thin film (80 nm thick) that has magnetized vertically was used (Micro Masch NSC35/Co-Cr). The radius of curvature of the tip was less than 90 nm. The full tip cone angle was less than 30° . Images were collected at different tip to sample separation (lift height) ranging from 30- 120 nm. Room temperature magnetization measurements were carried out using a vibrating sample magnetometer (DMS 1660 VSM) with an external field varying from -5 to $+5$ kOe.

8.3. Results and discussions

8.3.1 Evolution of morphology with substrate roughness

Characterization of the substrate surface was performed using Atomic force microscope. Figure 8.1 a & b shows 3-D AFM images of silicon and glass substrates. The best known parameter characterizing the morphology of a surface is its root mean square (rms) roughness. The rms roughness obtained from the AFM images for silicon and glass substrates were 0.77 nm and 3.38 nm respectively.

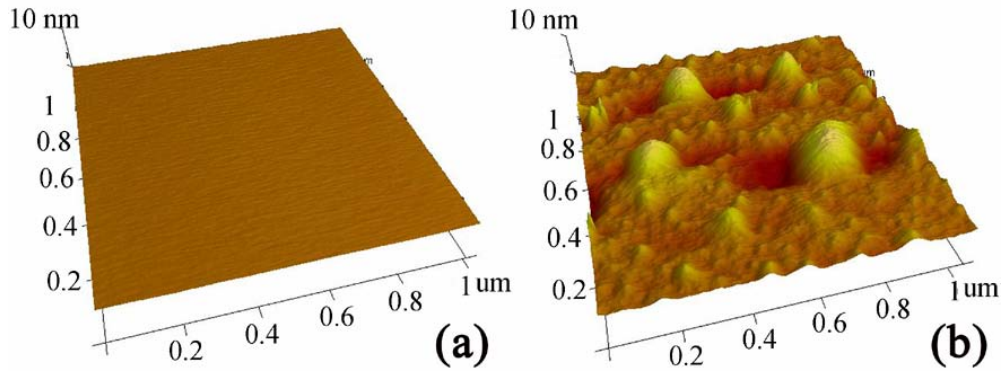


Fig.8.1 3-D AFM image of (a) Si surface (b) glass surface

Figure 8.2 (a) and (b) shows the topographic images of films coated on silicon (coded as sample A) and glass substrates (coded as sample B) respectively. A clear difference in morphology of the films obtained on the two different substrates was observed. Lateral size of the columns on silicon substrate is small (~ 250 nm) as well as they are closely packed (average separation between the columns ~ 240 nm). While well separated (average separation between the columns ~ 570 nm) and larger columns were obtained on a glass substrate (lateral size around 450 nm). The measured rms roughness was ~ 3.16 nm and 8.64 nm for sample sets A and B respectively. In both cases the rms roughness were smaller than the total film thickness (~ 50 nm) which suggests that there are film deposits in between the columns.

The line scans shown in figure 8.3 illustrates the size of the nano columns on both silicon and glass substrates. Tip convolution effects result in an exaggerated column width and in actual case the width of the column could be much less [181].

Columnar growth is a result of atomic shadowing mechanisms that occur at the substrate surface [89]. During the initial stages of vapour deposition, adatoms condense on to the substrate and form individual separated islands or nuclei. When the substrate is tilted such that the incident vapour arrives at oblique angles, the

topography of adatom nuclei results in geometrical shadowing over regions of the substrate, preventing the coalescence of nuclei into a continuous thin film layer. The nuclei capture the vapour flux that would have landed in the shadowed regions, resulting in the formation of columns.

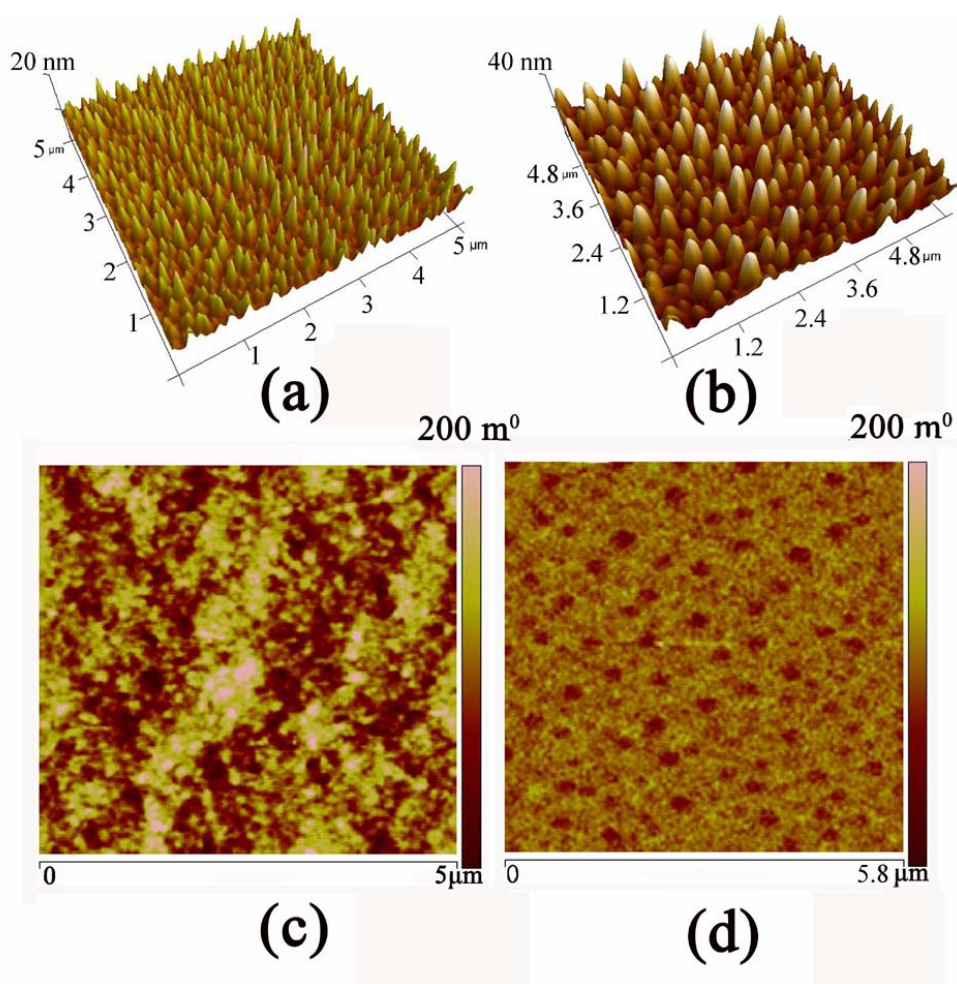


Fig. 8.2 a) 3-D AFM images for columns on (a) Si substrate (b) on glass substrate. MFM images for columns on (c) Si substrate (d) on glass substrate. Lift height in MFM scans is 60 nm.

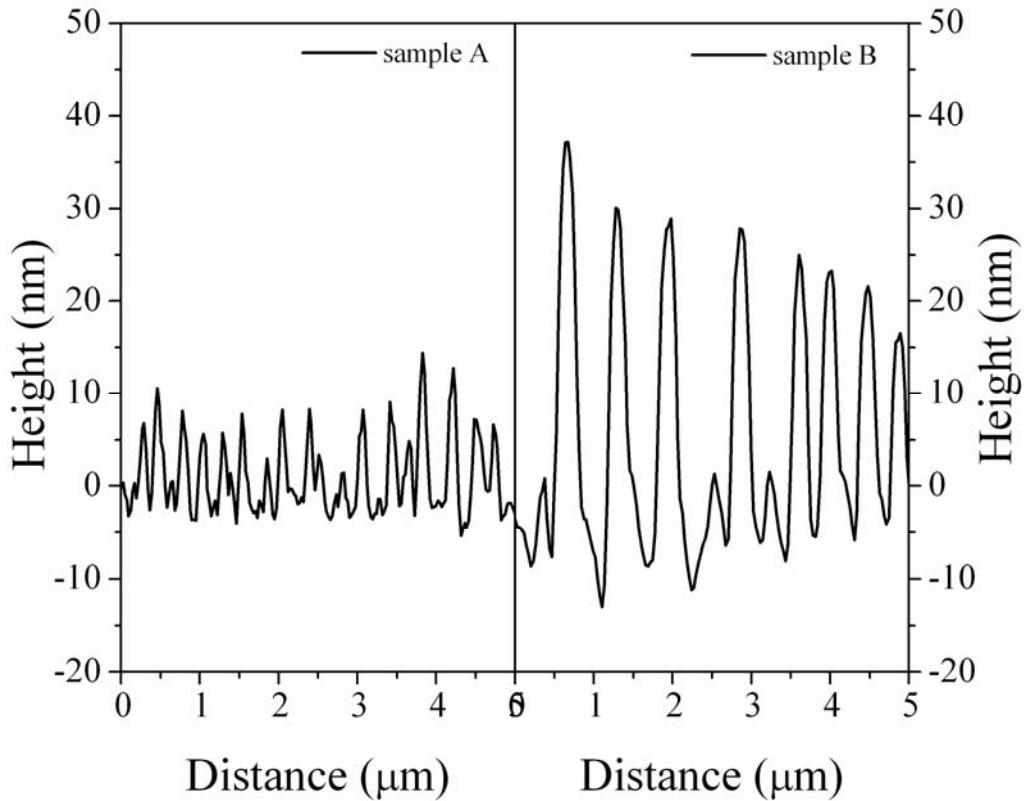


Fig.8.3 Line scans along the surface of sample A and B.

Deposition on smooth substrates generally results in a pseudo-random arrangement of nucleation sites during the initial stages of film growth, producing a similar distribution of columns over the substrate surface [175]. On the other hand, if there is a small perturbation to a flat surface, the irregularities act as nucleation sites for the columnar structure [120]. The topographical variations define the shadow regions on the substrate during the initial stages of film growth so that adatom nucleation is forced to occur on the surface protrusions. The small perturbations on the flat surface increase with time because surface protrusions receive more flux than valleys. If the protrusions are high enough, their shadows extends to its neighbour and

suppresses the inter-seed film growth. This can be a reason for the decreased inter columnar competition in sample prepared on glass substrate, where the initial irregularities were 2-3 nm in height. In glass substrates the column evolution is defined by the topographic protrusions on its surface, while in silicon it is defined by the Fe-Ni clusters formed initially. In films deposited on glass substrates, the separation between the columns was defined by the position of the irregularities on the substrate surface. Random nucleation on a smooth silicon surface resulted in a randomly arranged nano columns.

8.3.2 Magnetic properties

8.3.2.1 Magnetic force microscopy studies

MFM with a cantilever vibrating normal to the sample is sensitive to the gradient of the tip-sample interaction force in the normal direction of vibration, that is, to $\frac{\partial F_z}{\partial Z}$ [81,182]. The interaction force is $F = q \cdot \nabla H$, where q is the tip moment and H is the field at the tip. When the tip is ideally hard (e.g. coated with Co-Cr) and of constant moment q_z directed normal to the sample surface, the MFM signal is proportional to $q_z \frac{\partial^2 H_z}{\partial Z^2}$, that is, it is sensitive to the second derivative of the normal component of the sample field. The contrast in MFM image is thus proportional to the gradient of the magnetic force between the tip and the sample. Figure 8.2 (c) is an MFM image of sample A obtained at a lift height (tip-sample separation) of 60 nm. The contrast seen in the MFM images implies the presence of magnetic domains with out-of plane magnetic component. Sizes of the domains are larger than the width of individual columns which means that in this film there exists a magnetic interaction between the individual columns. In figure 8.2 (d) an MFM image of sample B indicates the existence of well separated circular domains. The microstructure of this

film is that of well separated larger columns and the MFM image from the corresponding scan area reveals that the out of plane magnetic component is only from individual columns. A one to one correspondence can be seen between the columns in the AFM image and circular domains in the MFM image of sample B (fig 8.2(b) & 8.2(d)). It is seen from the AFM images that the lateral size of columns for the two sample sets A and B are correspondingly 250 nm and 450 nm. While MFM images showed that the magnetic domain size are around 1.5 μm and 450 nm for the sample sets A and B respectively. This gives a clear indication that in sample A, magnetic correlation length is beyond the lateral size of individual columns. Thus in sample A the magnetic structure is not only determined by the individual columns but also by the magnetic interactions between them. The magnetic correlation length in sample B is within the column width itself which means that the columns in sample B are exchange isolated.

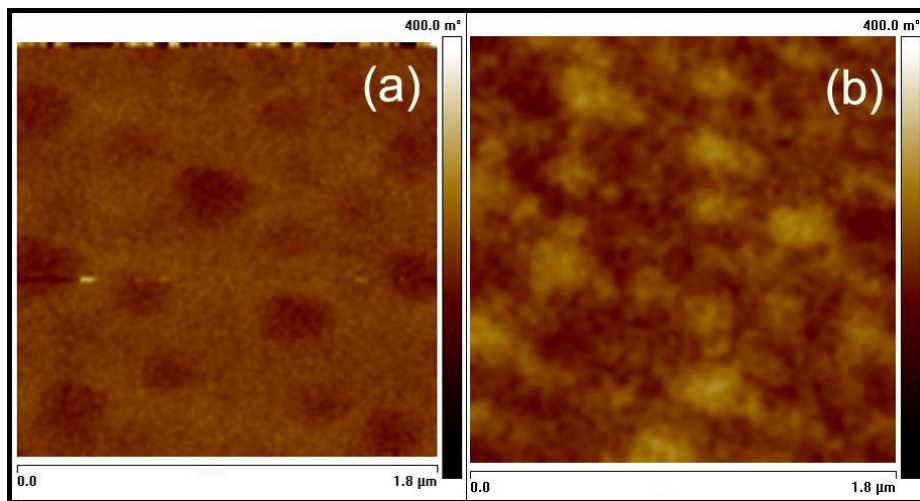


Fig.8.4 MFM images obtained at a lift height of 100 nm under two different tip magnetization orientations

In order to ensure that the contrast in the MFM image of sample B is caused by the film magnetization and not due to topographical artefacts, the tip magnetization was reversed by 180° and a MFM scan was obtained from the same area. Because it was not possible to relocate the scanning probe exactly the same scan line after removal of the tip for remagnetisation, exact mirror symmetry between the traces could not be expected. Figure 8.4 (b) shows MFM image of sample B for a lift height of 100 nm obtained after reversing the tip magnetization. The phase shift is now positive and the contrast is now inverted from dark to bright [when compared with MFM image in figure 8.4 (a)] which is an indication to the fact that the contributions to the MFM images are a result of magnetic forces of the sample.

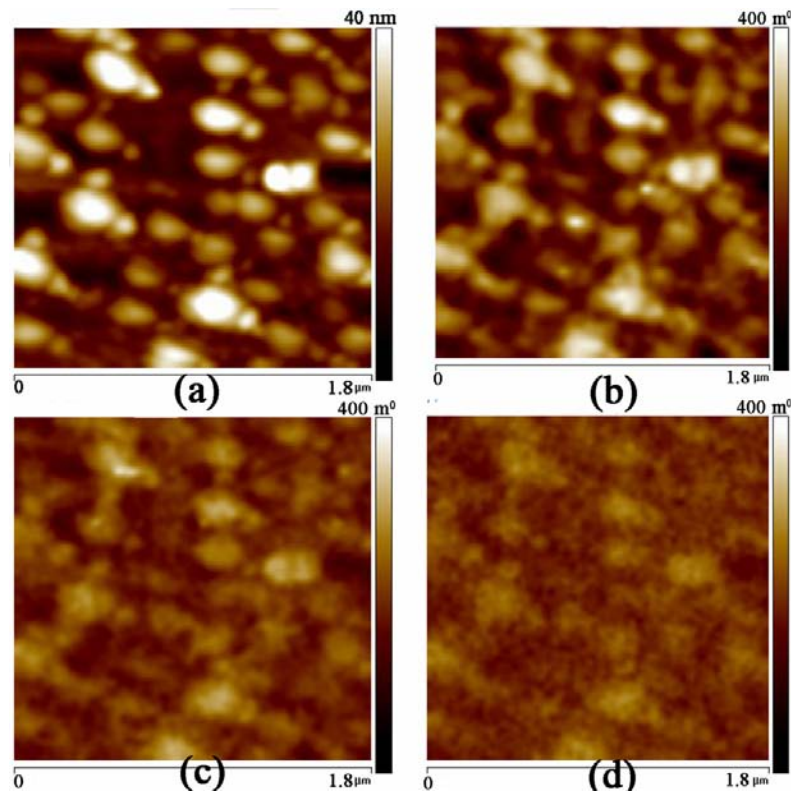


Fig.8.5 a) Topography b) Phase image at lift height of 30 nm c) 60 nm and d) 100 nm for sample B.

Figure 8.5 shows the topography and corresponding MFM images of samples B for a lift height of 30 nm, 60 nm and 100 nm. The plot of phase shift versus lift height (Figure 8.6) showed an exponential decay in agreement with our expectations. This decay in phase shift with lift height is due to the decay with distance of magnetic force from the sample.

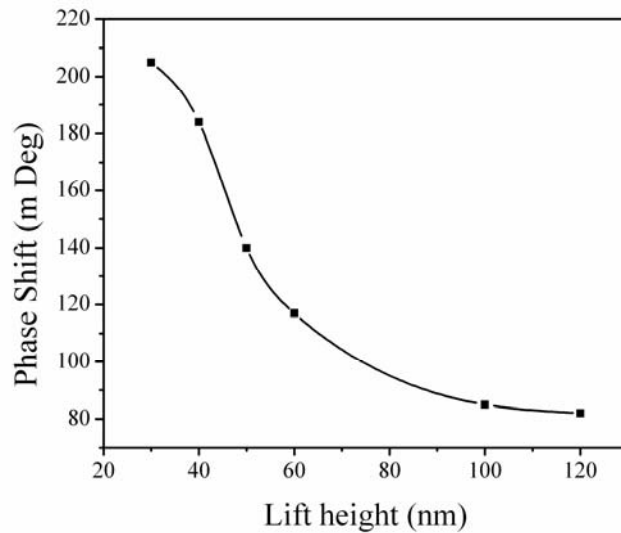


Fig.8.6 Scanning height dependence of phase shift in sample B

8.3.2.2 VSM studies

In order to gather more insight on the magnetic behaviour of the columns, room temperature magnetization measurements were performed on the two sample sets using a vibrating sample magnetometer. The measurements were carried out both in parallel (in-plane) and perpendicular fields (out-of plane). Figure 8.7 and 8.8 shows the magnetization curves for sample sets A and B respectively. The saturation magnetization was found to be ~ 870 emu/cc in both cases. It is to be noted that a low field was only necessary to saturate the magnetization in the in-plane direction while a field as high as 5000 Oe could not saturate the material in the out of plane

direction. AFM studies showed that the column height is smaller than the total film thickness implying that there is film deposits in-between the columns. Because of these deposits, the portion close to the substrate will become a continuous layer and the geometry of the whole system will be layer plus island type, in which islands are arranged on top of the layer. Due to the absence of significant magneto crystalline anisotropy, the magnetization direction will be largely influenced by the shape anisotropy. Within the layer, since the long axis is along the substrate plane, the magnetic direction will be in plane. On the other hand, in the islands, where the long axis is perpendicular to the substrate plane, the magnetic direction will be out of plane. The magnetization measurements using VSM will have contributions from the whole sample and one will only notice signatures of in plane magnetic direction because of the domination of the contributions emanating from the layer. However MFM being sensitive to the surface detects the out of plane component from the islands. The measurements show that the perpendicular magnetic component from the columns is small due to their small aspect ratio. The in-plane hysteresis loops show that the field necessary to saturate sample B (~2000 Oe) is double than that required for sample A (~1000 Oe). This can be correlated with the morphology of the columns prepared in two conditions.

In sample A the columns are packed close together (average inter-column distance around 240 nm) and MFM showed that there is a magnetic interaction between the columns. On the other hand, in sample B, the columns are well separated (average inter-column distance around 570 nm) and magnetic interaction between the columns is minimal. Since the columns of sample B are non-interacting, a larger magnetic field is required for achieving magnetic saturation. This field required for the sample A will be less due to the magnetic interaction existing in between the columns. Another feature to be noted from the in-plane hysteresis loop (Figures 8.7 & 8.8) is

that coercivity of sample B (~65 Oe) is larger than that of sample A (~40 Oe). This is due to the increased surface roughness of sample B.

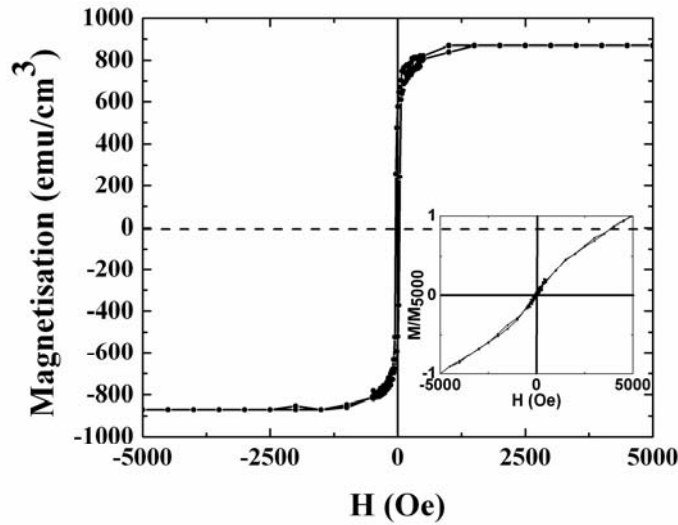


Fig.8.7 Room temperature hysteresis loop for nano columns on Si substrate in parallel field.

Inset shows the loop recorded in a perpendicular field.

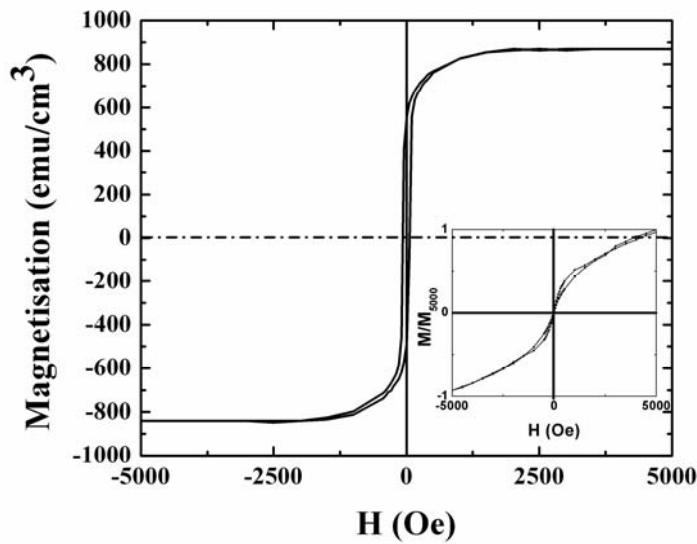


Fig.8.8 Room temperature hysteresis loop for nano columns on glass substrate in parallel field. Inset shows the loop recorded in a perpendicular field.

Small irregularities on the surface of a film inhibit the passage of a domain wall because the energy stored within a domain wall surrounding such a region is smaller than in an undisturbed domain wall and consequently the system energy must be increased to enable the domain wall motion. This is consistent with our previous observations in swift heavy ion irradiated Fe-Ni thin films [183].

8.4 Conclusions

Magnetic columnar thin films based on Fe-Ni were obtained by oblique angle deposition. Initial surface roughness of the substrate played a decisive role in the final morphology of the columnar structures. Thicker and taller columns were obtained on a glass substrate when compared to that on a smoother silicon substrate. Nucleation of Fe-Ni nano columns on a smooth silicon substrate were at random, while that on a rough glass substrate was defined by the irregularities on the substrate surface. The morphology of the resultant films determined their magnetic properties. Due to their small inter column separation, magnetic interaction was present for nano column arrays prepared on silicon substrates. On the other hand, well separated nano columns on glass substrate resulted in exchange isolated magnetic domains. These results also indicate that oblique angle deposition on a patterned substrate can result in well separated nano columns which can be promising for future high density recording applications.

Characterisation of Fe-Ni amorphous thin films for possible magnetostrictive sensor applications

9.1	Introduction
9.2	Experiment
9.3	Results and Discussions
9.4	Conclusion

9.1 Introduction

Magnetostrictive materials are currently of great interest due to their application potential in sensors and actuators [96,184,185]. Highly magnetostrictive materials are useful for ultrasound generators, magnetostrictive optical wavelength tuners and magnetostrictive delay lines [186]. Some of the requirements for practical applications of magnetostrictive materials include the capability to provide high saturation magnetostriction at low applied fields, ease of fabrication and low cost.

Fe-Ni based amorphous alloys are the best known candidates for magnetostrictive sensors because these amorphous alloys exhibit large saturation magnetostriction, high saturation magnetization, low anisotropy energies and low coercivity [187-189]. At present these alloys are available only in the form of ribbons of thickness ranging from 10 to 50 microns. A series of post treatment process such as high temperature annealing and epoxy treatment are further required for amorphous alloy ribbons to be used as sensors. Therefore there are many difficulties in fabricating systems based on amorphous ribbons for micro sensor applications. Magneto elastic materials in the form of thin films are an alternative to ribbons and they can be integrated easily to MEMS and NEMS [190]. This not only allows the miniaturization of sensor elements, but also enables the same micro-fabrication technologies to be

used in the production of both electronic and magnetic devices. The integration of magnetic components into MEMS (MagMEMS) offers the advantages of implementing wireless technology [191]. In comparison with other MEMS technologies, for example those incorporating piezoelectric materials, MagMEMS offer a high power density, low performance degradation, fast response times and ease of fabrication.

Thin films based on Fe-Ni can be prepared by techniques such as thermal evaporation, electrodeposition, molecular beam epitaxy, pulsed laser deposition and sputtering. Vapour deposition offers a simple alternative to sputter deposition in obtaining thin films of supersaturated solid solutions and other metastable states. The preparation of Fe-Ni amorphous thin films by thermal evaporation is described in the previous chapters and has been reported elsewhere [69,70,88,180,183,192]. The as prepared amorphous magnetic thin films usually present high coercivity due to the stresses in the films. The magnetic property of such films strongly depends on the magnitude of magnetoelastic anisotropies. So the measurement of magnetostriction is also important in the study of the amorphous ferromagnetic thin films.

Optical fibre long period grating (LPG) can be utilized to quantify the magnetostriction in thin films. It is a non destructive technique. Optical fibre long period grating based sensing methods offer other advantages of electromagnetic interference immunity, compactness, ease of fabrication and multiplexing [193].

LPG's are usually fabricated by exposing the core of a photosensitive optical fibre to a spatially varying ultra-violet beam [194]. Typically, the impinging UV beam is periodic in space and results in a regular pattern of refractive index modulation in the fibre core. For these gratings the energy typically couples from the fundamental guided mode to discrete, forward propagating cladding mode. Each LPG with a given periodicity Λ selectively filters light in a narrow band width centered on the peak wavelength of coupling λ_c [195]

$$\lambda_i = [n_{eff}(\lambda_i) - n_{cladd}^i(\lambda_i)]\Lambda \quad 9.1$$

Where n_{eff} is the effective index of refraction of the propagating core mode, n_{cladd}^i is the index of refraction of the i^{th} cladding mode, Λ is the period of grating and λ_i is the coupling wavelength. The value of n_{eff} depends on the core and cladding refractive index while the value of n_{cladd}^i depends on the core, cladding and air indices. When a tensile stress is applied to the optical fibre long period grating, the periodic spacing changes and thereby causes the coupling wavelength to shift. This provides a sensitive mechanism to measure the stress/strain and also the magnetostriction of a material attached to the fibre grating.

Few reports exist there in the literature describing the possible use of magnetostrictive transducers in fibre optic based sensors [196-198]. Miroslav Sedlar *et al.* [196] reported the magnetic field sensing properties of ferrite coated single mode optical fibers. Rengarajan and Walser [197] reported the fabrication of a high speed fibre optic sensor for magnetic field mapping. Their magnetostrictive transducer consisted of a multilayer film of $\text{Co}_{50}\text{Fe}_{50}/\text{Ni}_{80}\text{Fe}_{20}$. Chen *et al.* [198] reported the low field magnetostriction in an annealed Co-30% Fe alloy. Thick sheets of Co-Fe were bonded to a fibre Bragg grating sensor for magnetostriction measurements under different external magnetic fields. The majority of the studies concentrated on single mode fibers with an interferometer configuration for sensing the magnetic field. Long period grating based fibre sensors in combination with a magnetostrictive transducer is a better alternative for sensing the parameters such as magnetic field and strain. A survey of the literature reveals that not much work has been done on exploring the possibilities of amorphous magnetic thin film-LPG based magnetostrictive sensors. The combined use of Fe-Ni thin films and an external magnetic field can provide excellent tuning and chirping of long period fibre gratings [199]. The integration of a magnetostrictive material to an optical fibre long period grating can thus find potential

applications in magnetic field sensing, wavelength tunable optical filters and multiplexing devices. Therefore, the integration of Fe-Ni thin films on to an optical fibre long period grating not only enable us in measuring λ_s of amorphous thin films but also help us in realizing possible magnetostrictive sensor devices.

The work presented in this chapter focuses on the preparation of Fe-Ni based amorphous thin films and their integration into an optical fibre long period grating for potential magnetostrictive sensor applications. The attenuation band of the Fe-Ni coupled LPG had dependence on the strength of the magnetic field. Field dependent magnetostriction values were calculated from the shift in the central wavelength of the attenuation band. The results are presented here.

9.2 Experiment

Fe-Ni thin films of around 100 nm thickness were deposited simultaneously on to a silicon substrate and an optical fibre long period grating employing thermal evaporation technique. Commercially available Metglas 2826 MB ribbon of composition $\text{Fe}_{40}\text{Ni}_{38}\text{Mo}_4\text{B}_{18}$ was employed as a source material to deposit Fe-Ni thin films. The films were deposited by thermal evaporation using a current of 25 A at a base pressure of 1×10^{-5} mbar. The base pressure of $\sim 1 \times 10^{-5}$ mbar was achieved by a diffusion pump backed with a rotary pump. Room temperature magnetization measurements were carried out using a vibrating sample magnetometer (DMS 1660 VSM) with an external field varying from -2 to $+2$ kOe. Magnetostriction was measured by using an instrument with an optical fibre long period grating device, as shown in figure 9.1, in which the shift in the coupling wavelength due to the magnetostrictive strain was obtained using optical spectrum analyzer (YOKOGAWA, Model AQ6319) with a wavelength resolution of 10 pm. LPG was realized by exposing a photosensitive fibre, Newport F-SBG-15 to an excimer laser operated at

248 nm. Point to point technique was used for writing the grating and the grating period was $575 \mu\text{m}$. The grating was written over a length of 2 cm.

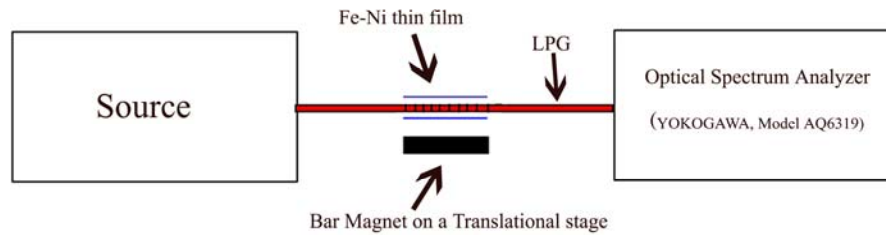


Fig 9.1 Schematic of the experimental set up for measuring magnetostriction

9.3 Results and discussions

Figure 9.2 shows room temperature hysteresis loop for thin film in parallel field. The saturation magnetization was found to be 865 emu/cc and the saturation was achieved at a field of 1000 Oe. The coercivity was ~ 60 Oe. Even in the absence of crystalline anisotropy, the origin of coercivity can be due to magnetoelastic anisotropies arising from stresses in the film.

In order to gain further insight into the magnetostrictive properties of the film, the magnetostriction was determined at various magnetic fields. The magnetostriction was measured by using an instrument with an optical fibre grating device, as shown in figure 9.1. The shift in the coupling wavelength due to the magnetostrictive strain was obtained with an optical spectrum analyzer.

For long period gratings, the energy typically couples from the fundamental guided mode to discrete, forward propagating cladding mode. The energy transferred to a cladding mode is then absorbed in the protective coating elsewhere in the fibre, which gives rise to an absorption band in the transmission spectrum of a fibre containing such a grating. The peak wavelength of absorption is defined by equation (9.1). When

a tensile stress is applied to the optical fibre long period grating the periodic spacing changes and thereby causes the coupling wavelength to shift. This provides a sensitive mechanism to measure the stress/strain and also the magnetostriction of a material attached to the fibre grating.

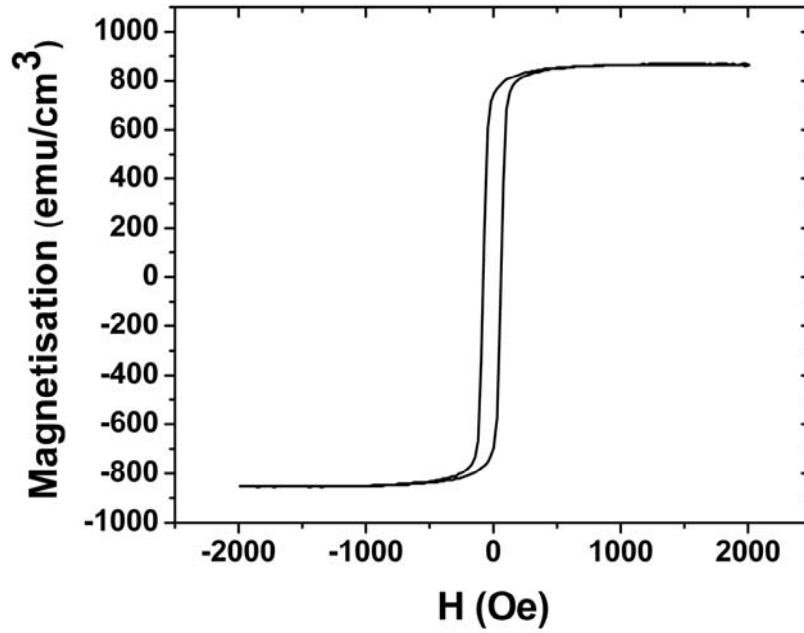


Fig. 9.2 Room temperature M-H curve for Fe-Ni film in a parallel field

The axial strain sensitivity of LPG's may be assessed by differentiating equation (9.1) [195]

$$\frac{d\lambda_i}{d\varepsilon} = \frac{d\lambda_i}{d(\delta n_{eff})} \left(\frac{dn_{eff}}{d\varepsilon} - \frac{dn_{cl}}{d\varepsilon} \right) + \Lambda \frac{d\lambda_i}{d\Lambda} \quad 9.2$$

The sensitivity comprises the material effects i.e. the change in fibre dimension and the strain-optic effect as well as waveguide effects arising from the slope of the

dispersion term $\frac{d\lambda_i}{d\Lambda}$.

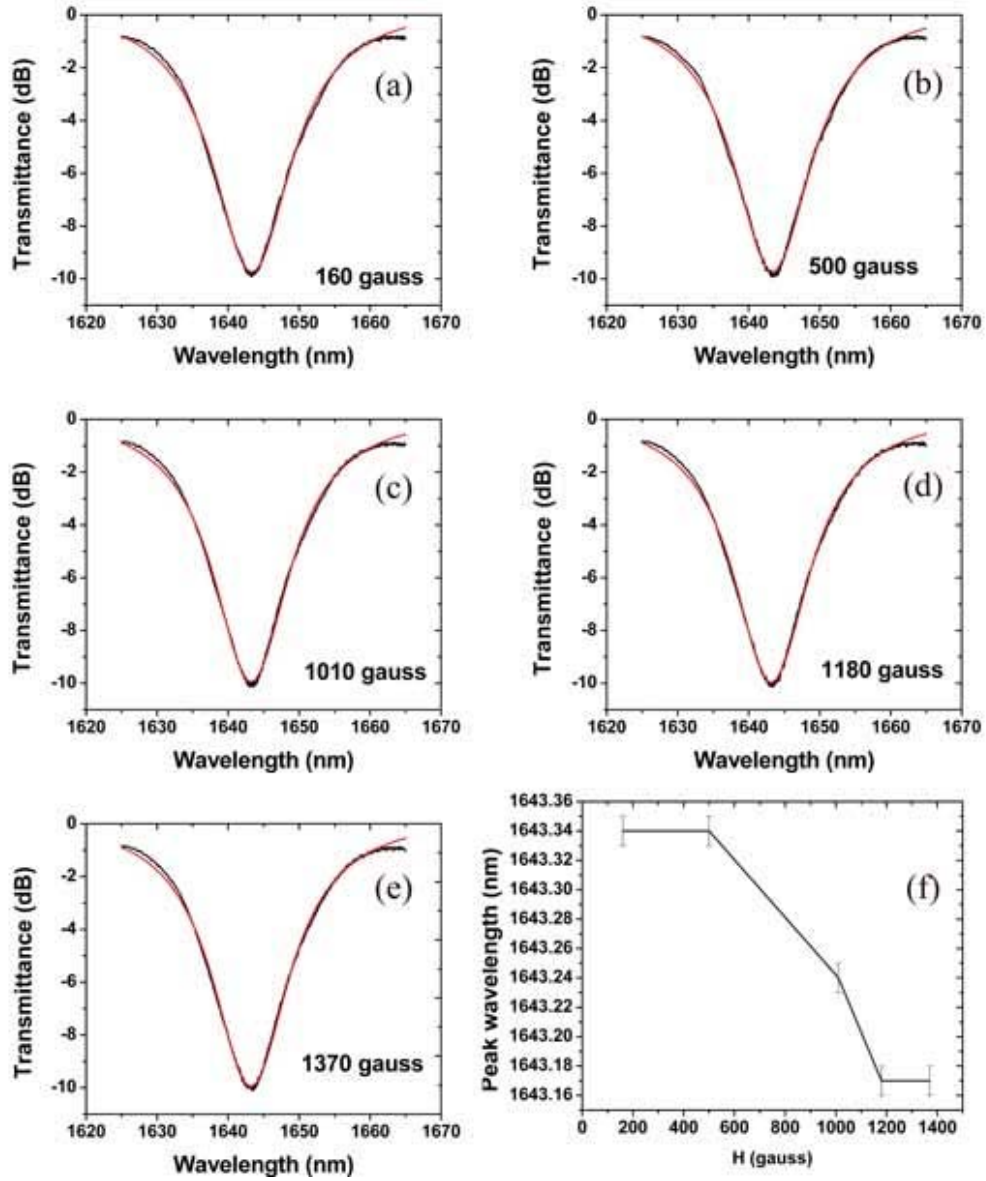


Fig 9.3 (a) Transmission spectrum at a magnetic field of 160 gauss (b) 500 gauss (c) 1010 gauss (d) 1180 gauss and (e) 1370 gauss. Variation of peak position with applied magnetic field is shown in (f)

When an axial strain is applied to the LPG, the resonant wavelength of the LPG will shift because the Λ of the LPG will increase and at the same time the effective refractive index of both core and cladding modes will decrease due to the photoelastic effect of the fibre.

The amount of wavelength shift is given by [194]

$$\frac{\delta\lambda_i}{\lambda_i} = \varepsilon_1 - \left(\frac{n^2}{2}\right)[p_{11}\varepsilon_1 + p_{12}(\varepsilon_1 + \varepsilon_t)] \quad 9.3$$

Where the principal strains are ε_1 along the fibre axis and ε_t transverse to the fibre axis. If the strain is homogeneous and isotropic, the above equation simplifies to its more common form

$$\frac{\delta\lambda_i}{\lambda_i} = [1 - p_e]\varepsilon \cong 0.78\varepsilon \quad 9.4$$

where the photoelastic contributions are subsumed into p_e which is defined by $p_e = \left(\frac{n^2}{2}\right)[p_{12} - \mu(p_{11} + p_{12})]$ in terms of the fibre Pockel's coefficients p_{ij} and μ the Poisson ratio. The photoelastic constant is about 0.22 for a silica fibre. This allows the magnetostriction of the sample (ε_s) to be directly determined by [198]

$$\varepsilon_s = \left(\frac{l_f}{l_s}\right)\varepsilon \quad 9.5$$

The factor $\left(\frac{l_f}{l_s}\right)$ is introduced to accommodate the difference in length between the fibre grating (l_f) and the sample (l_s). In the present experiment we have used $l_f = 2$ cm and $l_s = 2$ cm.

Figure 9.3 (a)-(e) shows the transmission spectra in the wavelength range 1625 nm-1665 nm of the Fe-Ni coated LPG for magnetic fields ranging from 160 gauss to

1370 gauss. The peak position was determined by fitting the experimental spectra using the Lorentian function (red line in the transmission spectra).

Figure 9.3(f) shows resonance wave length versus applied magnetic field. There is a decrease in the resonance wavelength position from 1643.34 nm to 1643.17 as the magnetic field increases from 500 gauss to 1180 gauss. For higher magnetic fields the change is minimal since the film has reached its magnetic saturation (figure 9.2).

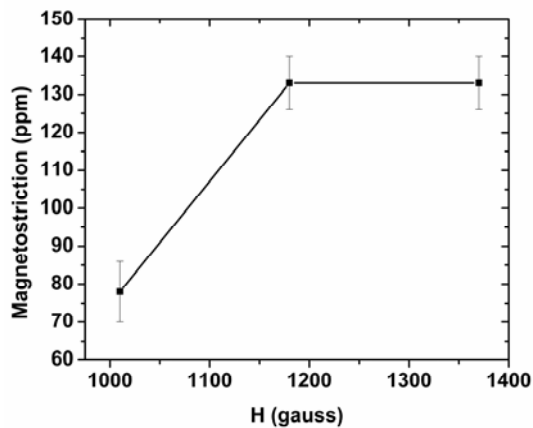


Fig. 9.4 Magnetostriction coefficient for Fe-Ni films at different magnetic fields

Magnetostriction values calculated at different fields using equation (9.5) are shown in figure 9.4. The saturation magnetostriction was found to be 130 ppm and the magnetostriction was saturated at fields of ~ 1200 gauss. Although, due to the experimental limitations only 3 data points was generated for demonstrating the magnetostriction exhibited by this material, the saturation magnetostriction achieved at a smaller magnetic field indicates the potential of Fe-Ni based amorphous thin films in magnetostrictive sensor devices. If the strain is amplified, for e.g. by using a multilayer stack of alternative magnetostrictive material (Fe-Ni) and a non-magnetic

thin film, a variety of applications such as wavelength tunable optical signal filter, wavelength channel add/drop multiplexer or a signal compensator is possible.

9.4 Conclusions

Fe-Ni based amorphous thin films were prepared by the thermal evaporation technique. The film was integrated to a long period fiber grating. The central wavelength of the attenuation band in the transmission spectrum of the long period grating decreased with an increase in the magnetic field. This dependence was due to the transfer of strain from film to fiber on application of a magnetic field. The change in the resonance wavelength was minimal once the film achieved its magnetic saturation. The magnetostriction properties exhibited by this film imply the potential application of this material in magnetostrictive sensor devices.

Conclusions and future outlook

Magnetic amorphous alloys represent a class of soft magnetic materials ideally suited for various applications. They shot to prominence with the discovery of Metglas/Finemet alloys back in 1988. However, with the advent of nanotechnology and the ever increasing need for their thin film, research work on these materials are also on the rise and efforts are made by scientists and engineer's world wide to improve upon the existing properties of these class of materials and also to evolve new materials based on magnetic amorphous alloys. It is known that the thin film forms of these alloys are in great demand for integration into MEMS and nanostructures based on these alloys are also sought after for storage applications. These alloy thin film can also be very useful candidates for sensor applications. From a fundamental perspective, many issues relating to the exchange correlation length, grain size and morphology also needs to be addressed. This investigation was an attempt encompassing some of these objectives and this chapter takes a close look at whether the intended objectives have been achieved or whether there exists any room for improvement and if so what is the future outlook.

Thin films of Fe-Ni were deposited from a composite target having a composition of $\text{Fe}_{40}\text{Ni}_{38}\text{Mo}_4\text{B}_{18}$. Electron microscopy observation revealed that the films were amorphous in nature. Energy dispersive x-ray spectroscopy and x-ray photoelectron spectroscopy showed that the films were replete in Fe with Ni and was depleted of B and Mo with a composition of $\text{Fe}_{55}\text{Ni}_{45}$. Vapour deposited thin films of Fe-Ni were vacuum annealed at different temperatures ranging from 373 K to 673 K to follow the microstructural evolution of the as deposited films. Electron microscopy

investigations showed that the microstructure of the annealed films consisted of Fe-Ni nanocrystals embedded in an amorphous matrix. The present study showed that the size of the nanocrystals can be tuned by annealing the films at different temperatures. It was found that coercivity had a strong dependence on grain size, D . The coercivity followed a $D^{3/2}$ dependence on the grain size in thin films contrary to the D^6 dependence observed in bulk nanocrystalline systems. The observed grain size dependence of coercivity was explained using a random anisotropy model extended to two dimensional systems.

Considering the prospects of fabricating thin films based on Fe-Ni from metallic glass ribbons by simple vacuum evaporation techniques and the fact that amorphous alloys are not resistant to irradiation induced damages, a detailed investigation for probing the surface modification of amorphous thin films of Fe-Ni by SHI irradiation was undertaken. It was found that bombardment of 108 MeV Ag^{8+} ions can result in roughening of Fe-Ni based amorphous thin film surfaces. The ion irradiation induced roughening can be due to the sputtering phenomena exhibited as a result of high electronic energy deposition. The coercivity of these films was found to increase with an increase in ion fluence. Magnetic squareness decreased with an increase in ion fluence and this was attributed to the increase in the in-plane demagnetization factor with an increase in surface roughness. Roughness induced local in-plane magnetic poles resulted in non uniform response of spins to an applied magnetic field and this in turn resulted in an increase in the saturating field for samples irradiated at higher fluences. Though SHI irradiation deteriorated the soft magnetic properties of the films, the increased coercivity and reasonable remanence (~ 0.5) suggests that a judicious choice of the ion fluence can alter the magnetic characteristics which suits novel applications of magnetic thin films. These results are promising and can be useful in tailoring the magnetic properties of a material in a controlled fashion.

In thin magnetic films the surface anisotropy has contributions from the dipolar magnetic fields generated by the irregularities on the surface profile. Hence a study relating the surface roughness and surface magnetisation orientation was demanded from a fundamental point of view as well as from an applied perspective. Magnetic force microscopy which is a surface sensitive technique is useful for such a study. Angular dependent FMR studies give a deep insight into the magnetic anisotropies present. A reorientation in surface magnetization direction from out-of-plane to in-plane was observed in Fe-Ni thin films on thermal annealing. It was found that surface modification by thermal annealing significantly modifies the in-plane and out-of-plane demagnetizing fields in these films. The in-plane demagnetising field decreased and out-of-plane demagnetising field increased on smoothing of Fe-Ni films surface. The surface roughness forced the surface magnetisation of as deposited Fe-Ni films to lie out-of-plane. The results indicates that by having a control on the surface roughness of magnetic thin films one can tailor the surface spin orientation which will find tremendous application in spintronics applications.

The growth of nanostructures by employing simple and cost effective methods remained elusive and hence an alternative method starting from ribbon precursors was thought to be a viable one. In the present work a simple and cost effective technique was employed for creating arrays of soft magnetic nanostructures. Fe-Ni based amorphous nano columns were grown on Si substrates by oblique angle deposition. The films were grown at different deposition times at an oblique angle of 40° . AFM was employed to quantitatively investigate the surface roughening process in the oblique angle vapour deposited amorphous thin films. Surface scaling analysis through roughness and PSD spectra showed that at low deposition time, the growth mechanism is dominated by self shadowing, while for higher deposition time, surface diffusion is also contributing to the growth process. This situation resulted in the lateral growth of nanostructures at higher deposition times. From an applied point of

view the method of obtaining magnetic nanostructures using this low-tech method is interesting and one should evolve preventive measures against surface diffusion while making attempts to get isolated nano structures. It was also found that initial surface roughness of the substrate played a decisive role in the final morphology of the columnar structures. Nucleation of Fe-Ni nano columns on a smooth silicon substrate were at random, while that on a rough glass substrate was defined by the irregularities on the substrate surface. The morphology of the resultant films determined their magnetic properties. Due to their small inter column separation, magnetic interaction was present for nano column arrays prepared on silicon substrates. On the other hand, well separated nano columns on glass substrate resulted in exchange isolated magnetic domains.

Finally, these Fe-Ni based amorphous thin films were integrated to a long period fiber grating. It was found that the central wavelength of the attenuation band in the transmission spectrum of the long period grating decreased with an increase in the magnetic field. This dependence was due to the transfer of strain from film to fiber on application of a magnetic field. The change in the resonance wavelength was minimal once the film achieved its magnetic saturation. The magnetostriction properties exhibited by this film imply that they can be used as magnetostrictive sensor devices.

If the strain is amplified, for example by using a multilayer stack of alternative magnetostrictive material (Fe-Ni) and a non-magnetic thin film, a variety of applications such as wavelength tunable optical signal filter, wavelength channel add/drop multiplexer or a signal compensator is possible. Further, scope exists for improving the transmission characteristics of an LPG for exhibiting an attenuation line with a narrow band width. Use of such a grating in combination with a Fe-Ni based magnetostrictive transducer will result in sensing strain as well as magnetic fields even without the aid of a high resolution spectrum analyser. The crystallisation process in

Fe-Ni thin films is not addressed in detail in the present work, and therefore scope exists in studying the nano crystallisation kinetics in these films by employing temperature dependent electrical resistivity measurements. Only such a study can deliver ideas on the type of crystallisation process taking place on thermal annealing, exact value of activation energies required for the crystalline phase formation and stability of the amorphous phase at high temperatures.

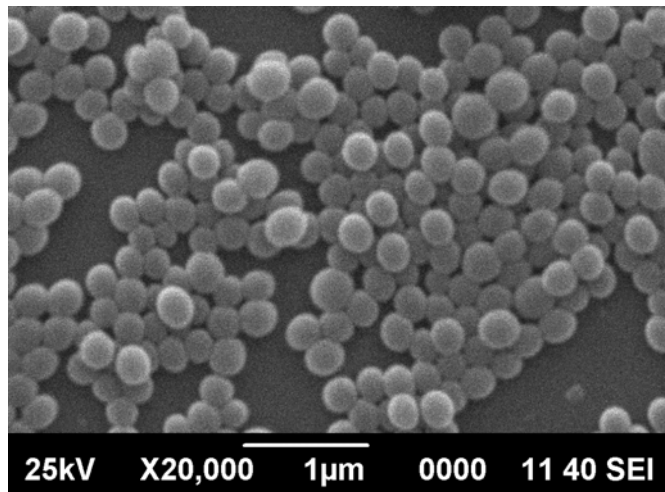


Fig 10.1 Silica spheres prepared by Stober process

The results on columnar thin film preparation by OAD indicates that oblique angle deposition on a patterned substrate can result in well separated nano columns which can be promising for future high density recording applications. Initial studies have already been carried out in this respect which can be extended to the future. The technique of OAD was successfully utilized for growing nano columns on different substrates; however, there was no control over the inter-columnar separation or the height of the columnar structures. Patterned substrates with appropriately designed width are an alternative and such substrates can be good templates for growing the

column. At the same time if a template like silica nano spheres assembled on the surface of porous alumina is utilized as substrates, Fe-Ni can be deposited on the surface.

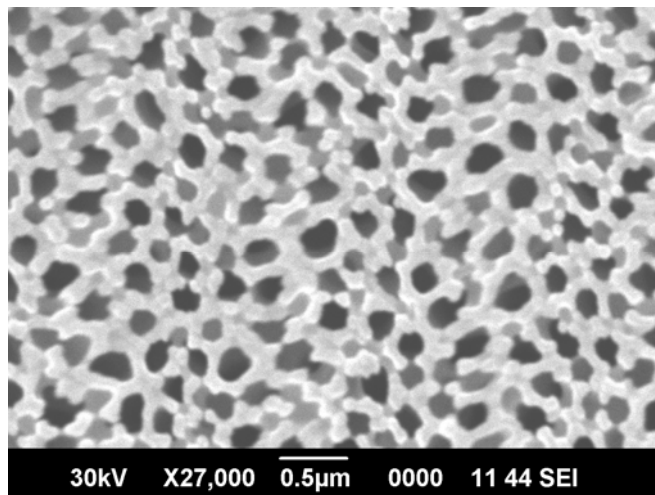


Fig 10.2 SEM Image of porous alumina template

Silica nano spheres can be prepared by the Stober process. A typical scanning electron microscopy image of silica nano spheres thus prepared is shown in figure 10.1. The diameter of the spheres in this particular case was found to be 300 nm. A colloidal solution consisting of silica nano spheres diluted with distilled water can be dropped onto the porous alumina substrate (a SEM image of the alumina template is shown in figure 10.2) which is kept tilted by 15°. The nano spheres are trapped in the template holes as the solution flows slowly downwards. As the colloidal solution dries, the nano spheres are fixed inside the holes, and a dense long-range order is formed. Once these spheres are trapped on the surface of a porous alumina template, they can serve as a patterned substrate with the inter silica separation depending on the size of the silica as well as the separation of alumina pores. Oblique angle deposition of Fe-Ni

on this patterned substrate will be an ideal for fabricating isolated soft magnetic nanostructures. Such a structure is expected to be an excellent platform for studying magnetism.

Though this thesis took a look at the structure, morphology and magnetism related issues which are of fundamental in nature, not much could be gathered on the nature of interactions taking place on the surface. For example, the kind of studies that can be focussed on these amorphous alloys in the future may be in finding out the role of short range forces enabling surface spins to align and their contribution to the overall magnetism of the film. It would be interesting to delve into the mechanism of flipping of surface spins and a detailed investigation using MOKE could shed light on this phenomenon. From an application point of view Fe-Ni based magneto elastic sensors are promising and could be easily fabricated using evaporation of Metglas ribbons. Magneto impedance measurements on the thin films will help throw light on the usefulness of these materials as sensors.

Appendix A

Symbols used in the thesis

B_s - Saturation magnetic induction

T_C - Curie temperatures

μ - Permeability

B - Flux density

H - Applied field

W_h - Energy consumed in one hysteretic cycle

ρ - Resistivity

M - Saturation magnetization _s

λ_s - Magnetostriction constant

T_x - Crystallization temperature

D - Grain size

K_2 - second order anisotropy constant

K_4 - fourth order anisotropy constant

M - Magnetisation

μ_m - magnetic dipole moments

μ_B - Bohr magneton

K_1 - first-order magnetic anisotropy constant

H_{INT} - Internal Field

λ_W - Weiss molecular field constant

k_B - Boltzmann constant

Appendix A

J_{ex} - Exchange Integral

H_{D} - Demagnetising field

N_{D} - Demagnetising factor

δ - Domain wall thickness

A - Exchange stiffness constant

L_{ex} - ferromagnetic exchange length

γ_{d} - Domain wall energy density

ϵ - Strain

λ - Magnetically induced strain

$\Delta l/l$ - Fractional change in length

k - Stiffness of the cantilever

$h\nu$ - Energy of a photon

E_{b} - Electron binding energy

E_{k} - Electron kinetic energy

Φ_{sp} - Spectrometer work function

λ_{m} - Inelastic mean free path of an electron

M_{r} - Retentivity

H_{c} - Coercivity

m - Effective mass of tip and cantilever

c_{eff} - Effective cantilever constant

f_0 - Free resonance frequency of the cantilever

G - Gilbert damping constant

γ - gyromagnetic ratio

ΔH - FMR linewidth

d - Inter-planar distance

x_{m} - Average distance between atoms

$(dE/dx)_e$ - Electronic energy loss

$(dE/dx)_n$ - Nuclear energy loss

R_p - Range of ions

ρ_{rms} - rms roughness

\mathbf{r} - Position vector

M_r/M_s - Squareness ratio

R_c - Ion track radii

S_e - Electronic energy loss

S_{th} - Threshold energy for ion track formation

$F_{parallel}$ - Parallel component of vapour flux

$F_{perpendicular}$ - Perpendicular component of vapour flux

β - Column tilt angle

$h(\mathbf{r},t)$ - Height function

L - AFM scan size

k - Spatial frequency

L_s - Shadowing length

h_s - Height of the columns

γ_p - Power

α_p - Roughness exponent

d_p - AFM line scan dimension

$H_r(0)$ - Resonance field for the applied dc field perpendicular to the sample plane

$H_r(90)$ - Resonance field for the applied dc field parallel to the sample plane

N_x - Demagnetising factor along x-direction

N_y - Demagnetising factor along y-direction

N_z - Demagnetising factor along z-direction

ω - Microwave frequency

Appendix A

n_{eff} - Effective index of refraction of the propagating core mode

n_{cladd}^i - Index of refraction of the i^{th} cladding mode

Λ - Grating period

λ_i - Coupling wavelength

Appendix B

Abbreviations used in the thesis

bcc - Body centered cubic

MEMS - Micro electro mechanical system

NEMS - Nano electro mechanical system

FMR - Ferromagnetic resonance

TMR - Tunneling magneto resistance

MOKE - Magneto optic Kerr effect

MagMEMS - Magnetic MEMS

OAD - Oblique angle deposition

TEM - Transmission electron microscopy

SHI - Swift heavy ions

AFM - Atomic force microscopy

LPG - Long period grating

MFM - Magnetic Force Microscopy

VSM - Vibrating Sample Magnetometer

fcc – Face centered cubic

IUAC - Inter University Accelerator Centre

SNICS - Source of negative ions by Cesium sputtering

GAXRD - Glancing angle x-ray diffraction

SEM - Scanning electron microscope

CRT - Cathode ray tube

Appendix B

EDS - Energy Dispersive X-ray spectroscopy

EELS - Electron Energy Loss Spectrum

EFTEM - Energy Filtered Transmission Electron Microscopy

STM - Scanning tunneling microscope

DFM - Dynamic Force Mode

Si(Li) - Lithium-drifted silicon

HPGe - High purity germanium

UPS - Ultraviolet photoelectron spectroscopy

XPS - X-ray photoelectron spectroscopy

PE spectroscopy - Photoelectron spectroscopy

CHA - Concentric hemispherical analyzer

XRD - X-ray diffraction

SAED - Selected area electron diffraction

PSD - Power spectral density

2D PSD - Two dimensional PSD

Bibliography

1. McHenry, M. E.; Willard, M. A.; David, E. 1999 Prog. Mater. Sci. **44** 291.
2. Yoshizawa Y, Oguma S, Yamauchi K. 1988 J Appl Phys. **64** 6044.
3. Yoshizawa Y, Yamauchi K, Yamane T, Sugihara H. 1988 J Appl Phys. **64** 6047.
4. Chen H S, Leamy H J and Miller C E 1980 Ann. Rev. Mater. Sci. **10** 363
5. Strange E A and Pim 1908 US Patent 905758
6. Chen H S and Miller C E 1970 Rev. Sci. Instrum. **41** 1237
7. Babic E, Girt E, Krsnik R, and Leontic B 1970 J. Phys. E: Sci. Instrum. **3** 1014
8. Masumoto T and Maddin R 1971 Acta Metall. **19** 725
9. Pond R and Maddin R 1969 Trans. Met Soc AIME **245** 2475
10. Liebermann H H and Graham C D Jr 1976 IEEE Trans. Magn. Mag **12** 921
11. Walter J L, Berkowitz A E and Koch E F 1983 Mater. Sci. Engg **60** 31
12. Yamaguchi T and Narita K 1977 IEEE Trans. Magn. Mag **13** 1621
13. Egami T 1984 Rep. Prog. Phys. **47** 1601
14. Liu B X, Clemens B M, Gaboriaud R, Johnson W L and Nicolet 1983 Appl. Phys. Lett. **42** 624
15. Simpson A W and Brambley D R 1971 Phys. Stat. Solidi **43** 291
16. Cochrane R W and Cargill G S IV 1974 Phys. Rev. Lett. **32** 476
17. Schwartz R B and Johnson W L 1983 Phys. Rev. Lett. **51** 415
18. Egami T and Waseda Y 1984 J. Non-Cryst. Solids **64** 113
19. Takao M and Senno H 1983 J. Magn. Magn. Mater. **31-34** 949
20. Chien C L and Unruh K M 1981 Phys. Rev. B **24** 1556
21. G. Herzer, Amorphous and nanocrystalline soft magnets (Kluwer Academic Publishers, Dordrecht/Boston/London, 1997) p.711-730
22. M Neagu 2006 J Opt Adv Mater **18** 1755

23. G V Kurlyandskaya, J M Barandiarán, P Mínguez and L Elbaile 2003
Nanotechnology **14** 1246
24. H. Okumura, D. J. Twisselmann, R. D. McMichael, M. Q. Huang, Y. N. Hsu, D.
E. Laughlin and M. E. McHenry 2003 J Appl Phys **93** 6528
25. Aleksandras ILJINAS, Sigitas JONELIŪNAS, Darius MILČIUS, Julius
DUDONIS 2007 Materials Science **13** 117
26. Y. Luo, M. Esseling, A. Käufler, K. Samwer, T. Dimopoulos, G. Gieres, M.
Vieth, M. Rührig, J. Wecker, C. Rudolf, T. Niermann and M. Seibt 2005 Phy Rev
B **72** 014426
27. L. H. Chen, H. K. Chen, C. T. Hsieh, Y. H. Shih, I. G. Chen, S. Y. Chen, and H.
P. Liu 2002 J Appl Phys **91** 8450
28. M. C. Contreras, J. F. Calleja, R. Matarranz, B. Presa, J. A. Corrales and G. Pan
2006 J Appl Phys **99** 08F110
29. M. Vopsaroiu, M. Georgieva, P. J. Grundy, G. Vallejo Fernandez, S. Manzoor
and M. J. Thwaites 2005 J Appl Phys **97** 10N303
30. N. X. Sun, Q. F. Xiao, and B. York 2005 J Appl Phys **97** 10F906
31. Nguyen Duy Ha, Manh-Huong Phan and Chong-Oh Kim 2006 J Appl Phys **99**
08F105
32. Tokihiko Yokoshima, Kenta Imai, Toshiki Hiraiwa, and Tetsuya Osaka 2004
IEEE Trans. Magn. **40** 2332
33. Xiaomin Liu, Giovanni Zangari and Liyong Shen 2000 J Appl Phys **87** 5410
34. D. Berling, A.P. Caricato, E. Denys, M. Fernández, G. Leggieri, S. Luby, A.
Luches, M. Martino, P. Mengucci 2007 Appl. Surf. Sci **253** 6522
35. Maria Neagu, M. Dobromir, G. Popa, H. Chiriac, Gh. Singurel, Cornelia Hison
2006 Sensors and Actuators A **129** 172
36. Z.G. Sun, H. Kuramochi, H. Akinaga 2005 Appl. Surf. Sci **244** 489
37. Z. Pászti, I. Szabó, É. Kisdi-Kosztó, G. Pető, Z. E. Horváth, E. Zsoldos, L. Guzzi
1998 Thin solid films **317** 294

38. Nguyen Duy Ha, Cheol Gi Kim, Chong Oh Kim and Manh-Huong Phan 2007 Solid State Comm. **141** 502
39. Wang S X, Sun N X, Yamaguchi M and Yabukami S 2000 Nature **407** 150.
40. M Farle, 1998 Rep.Prog.Phys **61**, 755
41. Dittschar A., M. Zharnikov, W. Kuch, M.-T. Lin, C. M. Schneider, and J. Kirschner, 1998 Phys. Rev. B **57**, R3209
42. R. Sellmann, H. Fritzsche, H. Maletta, V. Leiner and R. Siebrecht, 2001 Phys. Rev. B **64**, 054418
43. P. Pouloupoulos and K. Baberschke, 1999 J. Phys.: Condens. Matter **11**, 9495
44. Parmanand Sharma, Hisamichi Kimura, Akihisa Inoue, Elke Arenholz and J.-H. Guo, 2006 Phys. Rev. B **73**, 052401
45. C. H. Chang and M. H. Kryder 1994 J. Appl. Phys. **75** 6864
46. P. Bruno, G. Bayureuther, P. Beauvillain, C. Chappert, G. Lugert, D. Renard, J. P. Renard, and J. Seiden 1990 J. Appl. Phys. **68** 5759
47. J. Barnas and Y. Bruynseraede 1995 Europhys. Lett. **32** 167.
48. Q.Jiang, H.N. Yang, and G.C. Wang 1997 Surf. Sci. **373**, 181
49. Q. Jiang and G.-C. Wang 1996 J. Vac. Sci. Technol. B **14**, 3180
50. S. Vilain, J. Ebothe, and M. Troyon 1996 J. Magn. Magn. Mater. **157**, 274
51. V. I. Malyutin, V. E. Osukhovskii, Yu. D. Vorobiev, A. G. Shishkov, and V. V. Yudin 1981 Phys. Status Solidi A **65**, 45
52. J. W. Freeland, K. Bussmann, P. Lubitz, Y. U. Idzerda, and C.C. Kao 1998 Appl. Phys. Lett. **73** 2206
53. M. Li, G.C. Wang, and H.G. Min 1998 J. Appl. Phys. **83** 5313
54. J.H. Kim and S.C. Shin 1996 Jpn. J. Appl. Phys. Part 1 **35**, 342
55. E. Schlömann 1970 J. Appl. Phys. **41** 1617
56. A. Moschel, R. A. Hyman, A. Zangwill, and M. D. Stiles 1996 Phys. Rev. Lett. **77** 3653
57. Lisfi, A. ; Lodder, J. C.; Wormeester, H.; Poelsema, B. Phys. Rev. B **66**, 174420 (2002).

58. Henry Greve; Abhijit Biswas; Ulrich Schürmann; Vladimir Zaporojtchenko; Franz Faupel. 2006 *Appl. Phys. Lett.* **88** 123103.
59. Kar, A. K.; Morrow, P.; Tang, X-T.; Parker, T. C.; Li, H.; Dai, J-Y.; Shima, M.; Wang, G. C.; 2007 *Nanotechnology* **18** 295702.
60. Carl, A; Kirsch, S; Lohau, J; Weinforth, H; Wassermann, E.F. 1999 *IEEE Trans. Magn.* **35** 3106.
61. Giovanni Mastrogiacomo, Jürg Kradolfer, and Jörg F. Löffler 2006 *J. Appl. Phys* **99** 023908
62. Chikazumi S 1997 *Physics of Ferromagnetism*. (New York: Oxford Science Publications) p 163
63. Nicola Spaldin 2003 *Magnetic materials: fundamentals and device applications*. (Cambridge: Cambridge University Press) pp 66,79,123,127
64. Cullity B. D 1972 *Introduction to magnetic materials*. (MA: Addison-Wesley, Reading) pp 144,209,251,287
65. David Jiles 1998 *Introduction to magnetism and magnetic materials*. (Florida: Taylor & Francis) pp 205,228
66. Alben R, Becker J J, Chi MC 1978 *J. Appl. Phys* **49** 1653
67. Herzer G 1990 *IEEE Trans. Magn* **26** 1397
68. Herzer G 1991 *Mater. Sci. Eng. A* **133** 1
69. Senoy Thomas, S H Al-Harhi, D Sakthikumar, I A Al-Omari, R V Ramanujan, Yasuhiko Yoshida and M R Anantharaman 2008 *J. Phys. D: Appl. Phys.* **41** 155009.
70. T Hysen, S Deepa, S Saravanan, R V Ramanujan, D K Avasthi, P A Joy, S D Kulkarni M R Anantharaman, 2006 *J. Phys. D: Appl. Phys.***39** 1993
71. Gibbs M. R. J, 1990 *J. Magn. Magn. Mater.* **83** 329
72. C Richard Brundle, Charles A. Evans, Jr. and Shaun Wilson 1992 *Encyclopedia of Materials Characterization- Surfaces, Interfaces, Thin Films* (Massachusetts: Butterworth-Heinemann) pp 71,99,203

73. Ian M Watt 1997 *The Principles and Practice of Electron Microscopy* (Cambridge: Cambridge University Press) pp 89, p.413.
74. G. Binnig, C. F. Quate and Ch. Gerber 1986 *Phys. Rev. Lett.* **56** 930
75. http://www.pacificnanotech.com/afm-tutorial_atomic-force-microscope.html
76. Yip-wah Chung, 2001 *Practical guide to surface science and spectroscopy* (San Diego: Academic press) p.101.
77. Bharat Bhushan and Othmar Marti 2004 *Springer handbook of nanotechnology* (Heidelberg: Springer) p. 591.
78. David Briggs and M. P. Seah, *Practical Surface Analysis by Auger and X-Ray Photoelectron Spectroscopy* (John Wiley and Sons Ltd, Chichester, 1990)
79. D.J. O'Connor, Brett A. Sexton, Roger S.C. Smart 1992 *Surface Analysis Methods in Materials Science.* (Berlin: Springer-Verlag) p 165
80. B. D. Cullity, C. D. Graham 2008 *Introduction to Magnetic Materials.* (Wiley-IEEE) p.67.
81. U. Hartmann 1999 *Annu. Rev. Mater. Sci.* **29** 53
82. Klaus Baberschke, *Handbook of Magnetism and Advanced Magnetic Materials* (2007 John Wiley & Sons Ltd) p.1618
83. Yong Lu and Arokia Nathan 1997 *Appl. Phys. Lett.* **70** 526
84. Hasegawa R 2004 *Mater. Sci. Eng. A* **375** 90
85. Hernando A, Marín P, López M, Kulik T, Varga L K, and Hadjipanayis G 2004 *Phys. Rev. B* **69** 052501
86. Hono K and Ohnuma M 2002 *Magnetic Nanostructures.* H S Nalwa (California: American Scientific Publishers) p 327
87. Idzikowski B, Szajek A, Greneche J M and Kovac J 2004 *Appl. Phys. Lett.* **85** 1392
88. Jyothi M and Suryanarayana C 1985 *Z. Metallkd.* **76** 802
89. Hawkeye M M and Brett M J 2007 *J.Vac.Sci.Technol. A* **25** 1317
90. Du S W and Ramanujan R V 2004 *Mater. Sci. Eng. A* **375** 1040

91. Dunlop A, Jaskierowicz G, Rizza G and Kopcewicz M. 2003 Phys. Rev. Lett. **90** 015503
92. John F. Moulder, William F. Stickle, Peter E. Sobol and Kenneth D. Bomben 1992 Hand book of X-ray photoelectron spectroscopy. Jill Chastain (Minnesota: Perkin-Elmer Corporation) p 222
93. Teruo Bitoh, Akihiro Makino and Akihisa Inoue 2004 J.Mag.Mag.Mater **272** 1445.
94. Chikazumi S 1997 Physics of Ferromagnetism. (New York: Oxford Science Publications) p 287
95. Eiji Kita, Naoki Tsukuhara, Hidenori Sato, Keishin Ota, Hideto Yangaiharu, Hisanori Tanimoto and Naoshi Ikeda 2006 Appl. Phys. Lett. **88** 152501
96. E. Komova, M. Varga, R. Varga, P. Vojtanik, J. Bednarcik, J. Kovac, M. Provencio and M. Vazquez 2008 Appl. Phys. Lett. **93** 062502.
97. Jinn P. Chu, Chang-Ting Lo, Yi-Kun Fang and Bao-Shan Han 2006 Appl. Phys. Lett. **88** 012510.
98. T R Anantharaman, Metallic alloys production properties and applications (Trans Tech, Aedermannsdof, 1984) p.2.
99. S. Ladak, L. E. Fernández-Outón, and K. O'Grady 2008 J. Appl. Phys. **103** 07B514.
100. Y.-P. Zhao, R. M. Gamache, G.-C. Wang, T.-M. Lu, G. Palasantzas and J. Th. M. De Hosson 2001 J. Appl. Phys. **89** 1325.
101. Y.-P. Zhao, G. Palasantzas, G.-C. Wang and J. Th. M. De Hosson 1999 Phys. Rev. B **60** 1216.
102. Dipak Paramanik, Asima Pradhan and Shikha Varma 2006 J. Appl. Phys. **99** 014304.
103. S. Mechler, C. Abromeit, N. Wanderka, M.-P. Macht, T. Zumkley, G. Schumacher, S. Klaumünzer 2006 Nucl. Instrum. Methods Phys Res. B **245** 133.

- 104.S. Nagata, S. Higashi, B. Tsuchiya, K. Toh, T. Shikama, K. Takahiro, K. Ozaki, K. Kawatusra, S. Yamamoto, A. Inouye 2007 Nucl. Instrum.Methods Phys Res.B **257** 420.
- 105.G. Rizza, A. Dunlop, M. Kopcewicz 2006 Nucl. Instrum.Methods Phys Res.B **245** 130.
- 106.P. Ziemann, W. Miehle, A. Plewnia 1993 Nucl. Instrum.Methods Phys Res.B **80** 370.
- 107.E. M. Bringa and R. E. Johnson 2002 Phys. Rev. Lett. **88** 165501.
- 108.R. L. Fleischer, P. B. Price, R. M. Walker and E. L. Hubbard 1967 Phys. Rev. **156** 353.
- 109.R. L. Fleischer, P. B. Price, and R. M. Walker 1965 J. Appl. Phys. **36** 3645.
- 110.S. Klaumünzer and G. Schumacher 1983 Phys. Rev. Lett. **51** 1987.
- 111.G. Schumacher, S. Klaumünzer, S. Rentzsch, G. Vogl 1984 J. Non- Cryst. Solids. **61** 565.
- 112.A.Audouard, R. Mamy, M. Toulemonde, G. Szenes and L. Thomé 1997 Eur.Phys.Lett **40** 527.
- 113.A.Audouard, R. Mamy, M. Toulemonde, G. Szenes, L. Thomé 1998 Nucl. Instrum.Methods Phys Res.B **146** 217.
- 114.S.W. Du, R.V. Ramanujan 2005 J. Non-Cryst. Solids **351** 3105.
- 115.www.metglas.com.
- 116.S. G. Mayr and R. S. Averback 2001 Phys. Rev. Lett. **87** 196106.
- 117.H. D. Mieskes, W. Assmann, F. Grüner H. Kucal, Z. G. Wang, and M. Toulemonde 2003 Phys. Rev. B **67** 155414.
- 118.G. Rizza, A. Dunlop, G. Jaskierowicz, M. Kopcewicz 2004 Nucl. Instrum.Methods Phys Res.B **226** 609
- 119.G. Szenes 1995 Phys. Rev. B **51** 8026
- 120.P. Bai, J. F. McDonald, and T.-M. Lu and M. J. Costa 1991 J. Vac. Sci. Technol. A **9** 2113.

- 121.K. Zhang, M. Uhrmacher, H. Hofsäss, and J. Krauser 2008 J. Appl. Phys. **103** 083507
- 122.K Zhang, F Rotter, M Uhrmacher, C Ronning, J Krauser and H Hofsäss 2007 New J. Phys. **9** 29
- 123.D. S. Rodbell and C. P. Bean 1956 Phys. Rev. **103** 886.
- 124.M. Li, Y.P. Zhao, G. C. Wang and H.G. Min 1998 J. Appl. Phys. **83** 6287 .
- 125.Doherty S.A., Zhu J. G., Dugas, M., Anderson, S and Tersteeg, J. 1998 IEEE Trans. Magn. **34** 840.
- 126.J. Swerts, K. Temst, N. Vandamme, C. Van Haesendonck, Y. Bruynseraede 2002 J.Mag.Mag.Mater **240** 380.
- 127.M. Li, G.-C. Wang and H.-G. Min 1998 J. Appl. Phys. **83** 5313
- 128.Deeder Aurongzeb, K. Bhargava Ram and Latika Menon 2005 Appl. Phys. Lett. **87** 172509
- 129.T Kaneyoshi, 1991 J. Phys.: Condens. Matter **3**, 4497
- 130.Xavier Batlle and Amílcar Labarta, 2002 J. Phys. D **35**, R 15
- 131.Popov A. P. and D. P. Pappas, 1997 Phys. Rev. B **56**, 3222
- 132.Rajesh V. Chopdekar, Elke Arenholz and Y. Suzuki, 2009 Phys. Rev. B **79**, 104417
- 133.Reichl I., A. Vernes, P. Weinberger, L. Szunyogh and C. Sommers, 2005 Phys. Rev. B **71**, 214416
- 134.S. Gallego, L. Szunyogh, P. Weinberger and M. C. Muñoz, 2004 Phys. Rev. B **69**, 224408
- 135.R. Hammerling, J. Zabloudil, P. Weinberger, J. Lindner, E. Kosubek, R. Nünthel and K. Baberschke, 2003 Phys. Rev. B **68**, 092406
- 136.Jisang Hong, R. Q. Wu, J. Lindner, E. Kosubek, and K. Baberschke, 2004 Phys. Rev. Lett **92**, 147202
- 137.R. Denk, M. Hohage and P. Zeppenfeld, 2009 Phys. Rev. B **79**, 073407
- 138.Rodrigo Arias and D. L. Mills, 1999 Phys. Rev. B **59**, 11871

- 139.D. M. Schaller, D. E. Bürgler, C. M. Schmidt, F. Meisinger and H.-J. Güntherodt, 1999 Phys. Rev. B **59**, 14516
- 140.P. Weinberger, J. Zabloudil, R. H. Hammerling, L. Szunyogh, T. L. Monchesky and B. Heinrich, 2003 Phys. Rev. B **67**, 054404
- 141.J.-S. Lee, K.-B. Lee, Y. J. Park, T. G. Kim, J. H. Song, K. H. Chae, J. Lee, C. N. Whang, K. Jeong, D.-H. Kim and S.-C. Shin, 2004 Phys. Rev. B **69**, 172405
- 142.P. Pouloupoulos, J. Linder, M. Farle and K. Baberschke, 1999 Surf. Sci. **437**, 277
- 143.Y.-P. Zhao, G. Palasantzas, G.-C. Wang and J. Th. M. De Hosson, 1999 Phys. Rev. B **60**, 1216
- 144.Gabriel Bochi, C. A. Ballentine, H. E. Inglefield, C. V. Thompson, and R. C. O'Handley, 1996 Phys. Rev. B **53**, R1729
- 145.Kenta Amemiya, Enju Sakai, Daiju Matsumura, Hitoshi Abe, Toshiaki Ohta and Toshihiko Yokoyama, 2005 Phys. Rev. B **71**, 214420
- 146.Daiju Matsumura, Toshihiko Yokoyama, Kenta Amemiya, Soichiro Kitagawa, and Toshiaki Ohta, 2002 Phys. Rev. B **66**, 024402
- 147.Fabio Favot, Andrea Dal Corso, and Alfonso Baldereschi, 2001 Phys. Rev. B **63**, 115416
- 148.D. Peterka, A. Enders, G. Haas and K. Kern, 2002 Phys. Rev. B **66**, 104411
- 149.H. Sang, N. Xu, J.H. Du, G. Ni, S.Y. Zhang and Y.W. Du, 1999 Phys. Rev. B **53**, 15023
- 150.K. Lenz, H. Wende, W. Kuch, K. Baberschke, K. Nagy and A. Jánossy, 2006 Phys. Rev. B **73**, 144424
- 151.Kh. Zakeri, J. Lindner, I. Barsukov, R. Meckenstock, M. Farle, U. von Hörsten, H. Wende, W. Keune, J. Rucker, S. S. Kalarickal, K. Lenz, W. Kuch, K. Baberschke and Z. Frait, 2007 Phys. Rev. B **76**, 104416
- 152.K. Baberschke, in Investigation of Ultrathin Ferromagnetic Films by Magnetic Resonance, edited by H. Kronmüller and S. S. Parkin, Hand-book of Magnetism and Advanced Magnetic Materials, Volume 3 (Wiley, New York, 2007), p. 1617.

- 153.W. Platow, A. N. Anisimov, G. L. Dunifer, M. Farle and K. Baberschke, 1998
Phys. Rev. B **58**, 5611
- 154.M. Sorescu, E. T. Knobbe and D. Barb 1995 Phys. Rev. B **51**, 840
- 155.Yanguas-Gil, J. Cotrino, A. Walkiewicz-Pietrzykowska, and A. R. González-Elipe
2007 Phys. Rev. B **76**, 075314
- 156.Borrás, A. Yanguas-Gil, A. Barranco, J. Cotrino, and A. R. González-Elipe 2007
Phys. Rev. B **76**, 235303.
- 157.M. A. Auger, L. Vázquez, O. Sánchez, M. Jergel and R. Cuerno 2005 J. Appl.
Phys. **97**, 123528.
- 158.K. Rechendorff, M. B. Hovgaard, J. Chevallier, M. Foss, and F. Besenbacher 2005
Appl. Phys. Lett. **87**, 073105
- 159.Dolatshahi-Pirouz, M. B. Hovgaard, K. Rechendorff, J. Chevallier, M. Foss and
F. Besenbacher 2008 Phys. Rev. B **77**, 115427
- 160.H. Alouach and G. J. Mankey 2005 Appl. Phys. Lett. **86**, 123114
- 161.Junhua Xu, Lihua Yu, and Isao Kojima 2003 J. Appl. Phys. **94**, 6827
- 162.T. Karabacak, G.-C. Wang and T.-M. Lu 2003 J. Appl. Phys. **94**, 7723
- 163.Hernando, A.; Vazquez, M.; Barandiaran, J. M. 1988 J. Phys. E **21** 1129.
- 164.Osaka, T; Takai, M; Hayashi, K; Ohashi, K; Saito, M; Yamada, K. 1998 Nature
392 796.
- 165.Hayakawa, Y; Makino, A; Fujimori, H; Inoue, A. 1997 J. Appl. Phys. **81** 3747.
- 166.Vazquez, M; Hernando, A; 1996 J. Phys. D: Appl. Phys **29** 939.
- 167.Liu, X.; Fu, L.; Hong, S.; Dravid, V.P.; Mirkin, C.A. 2002 Adv. Mater.**14** 231.
- 168.Shouheng Sun, Hao Zeng, David B. Robinson, Simone Raoux, Philip M. Rice,
Shan X. Wang, and Guanxiong Li. 2004 J. Am. Chem. Soc. **126** 273.
- 169.Shouheng Sun; Murray, C. B.; Dieter Weller; Liesl Folks; Andreas Moser. 2000
Science **287** 1989.
- 170.Taeghwan Hyeon.; 2003 Chem. Commun. **8** 927.
- 171.Azzaroni, O.; Schilardi, P. L.; Salvarezza, R. C. 2002 Appl. Phys. Lett. **80** 1061.
- 172.Robbie, K; Brett, M.J. 1997 J. Vac. Sci. Technol. A **15** 1460.

173. Dick, B.; Brett, M. J.; Smy, T. J.; Freeman, M. R.; Malac, M.; Egerton, R. F. 2000 *J Vac Sci Technol A* **18** 1838.
174. Messier, R.; Lakhatiah, A. 1999 *Mat Res Innovate* **2** 217.
175. John J. Steele; Michael J. Brett. 2007 *J Mater Sci: Mater Electron*. **18** 367.
176. Martin O. Jensen and Michael J. Brett. 2005 *IEEE Trans. Nanotech.* **4** 269.
177. Y.-P. Zhao, D.-X. Ye, G.-C. Wang and T.-M. Lu *Proceedings of SPIE Vol. 5219 Nanotubes and Nanowires*, edited by Akhlesh Lakhtakia, Sergey Maksimenko, (SPIE, Bellingham, WA, 2003) page 59.
178. Demirel, M.C.; Boduroglu, S.; Cetinkaya, M.; Lakhtakia, A. 2007 *Langmuir* **23** 5861.
179. Tang, X-J; Zhang, G.; Zhao, Y-P. 2006 *Nanotechnology* **17** 4439.
180. Senoy Thomas; Al-Harhi, S. H.; Ramanujan, R. V.; Zhao Bangchuan; Liu Yan; Wang Lan; Anantharaman, M. R. 2009 *Appl. Phys. Lett.* **94** 063110.
181. Rasa, M; Kuipers, B. W. M; Philipse, A. P. 2002 *J. Colloid Interface Sci.* **250** 303
182. Steffen Porthun; Leon Abelmann; Cock Lodder. 1998 *J. Magn. Magn. Mater.* **182** 238.
183. Senoy Thomas; Hysen Thomas; Avasthi, D. K.; Tripathi, A.; Ramanujan, R. V.; Anantharaman, M. R. 2009 *J. Appl. Phys.* **105** 033910.
184. Kolano-Burian A, R Kolano, M Kowalczyk, J Szyrowski, M Steczkowska-Kempka and T Kulik 2009 *J. Phys.: Conf. Ser.* **144** 012062
185. Lou J., R. E. Insignares, Z. Cai, K. S. Ziemer, M. Liu and N. X. Sun 2007 *Appl. Phys. Lett.* **91** 182504
186. Hristoforou E 2003 *Meas. Sci. Technol.* **14** R15
187. Akihiro Makino, He Men, Takeshi Kubota, Kunio Yubuta and Akihisa Inoue 2009 *J. Appl. Phys.* **105** 07A308
188. Akihiro Makino, He Men, Kunio Yubuta and Takeshi Kubota 2009 *J. Appl. Phys.* **105** 013922
189. Akihisa Inoue and Wei Zhang 1999 *J. Appl. Phys.* **85** 4491
190. Gibbs M R J, E W Hill and P J Wright 2004 *J. Phys. D: Appl. Phys.* **37** R237.

191. Gibbs M R J 2007 IEEE Trans. Magn. **43** 2666
192. Senoy Thomas, S. H. Al-Harhi, I. A. Al-Omari, R. V. Ramanujan, V. Swaminathan and M. R. Anantharaman 2009 J. Phys. D: Appl. Phys. **42** 215005
193. Alan D. Kersey, Michael A. Davis, Heather J. Patrick, Michel LeBlanc, K. P. Koo, C. G. Askins, M. A. Putnam, and E. Joseph Friebele 1997 J. Lightwave Technol. **15** 1442
194. Kenneth O. Hill and Gerald Meltz 1997 J. Lightwave Technol. **15** 1263
195. Stephen W James and Ralph P Tatam 2003 Meas. Sci. Technol **14** R49
196. Miroslav Sedlar, Ivan Paulicka, and Michael Sayer 1996 Appl. Optics. **35** 5340
197. Rengarajan S. and R. M. Walser 1997 J. Appl. Phys. **81** 4278
198. Chen L. H., T. J. Klemmer, H. Mavoori, and S. Jin 1999 Appl. Phys. Lett **74** 2047
199. Cruz J.L., A. Díez, M.V. Andrés, A. Segura, B. Ortega, and L. Dong 1997 Electron. Lett. **33** 235